Table of Content

2 CHAPTER 2 – CRACKING IN ASPHALT MATERIALS

Edited By: E. Dave (1), R. Botella (2), P. Marsac (3), D. Bodin (4)

(1) University of New Hampshire, USA
(2) University of Catalonia, Spain
(3) IFSTTAR, France
(4) ARRB Group, Australia

Abstract

This chapter provides a comprehensive review of both laboratory characterization and modelling of bulk material fracture in asphalt mixtures. For the purpose of organization, this chapter is divided into a section on laboratory tests and a section on models. The laboratory characterization section is further subdivided on the basis of predominent loading conditions (monotonic versus cyclic). The section on constitutive models is subdivided into two sections, the first one containing fracture mechanics based models for crack initiation and propagation that do not include material degradation due to cyclic loading conditions. The second section discusses phenomenological models that have been developed for crack growth through the use of dissipated energy and damage accumulation concepts. These latter models have the capability to simulate degradation of material capacity upon exceeding a threshold number of loading cycles.

2.1 INTRODUCTION

As described in the first chapter of this report, asphalt mixtures are heterogeneous composites with temperature, rate and hereditary dependencies amongst other complexities such as oxidative aging and non-uniformities due to construction practices. Characterization of fracture in this highly complex, viscoelastic particulate composite is a challenging task. Cracking realted failures in asphalt pavements are often associated with fractures occurring within the asphalt materials or debonding occurring between asphalt layers or between asphalt and other pavement layers. Thermal and fatigue cracking in asphalt pavements as well as certain aspects of reflective cracking are examples of fracturing within 'bulk' asphalt concrete materials. In order to understand the mechanisms of cracking in asphalt pavements it is critical to be able to adequately characterize and understand the physical nature of fracture in the bulk material, particularly within near-surface layers, where damage and cracking tend to appear most often. Such characterization includes the ability to conduct and interpret bulk fracture tests and the availability of analytical and computational models that can capture key physical processes associated with failure of asphalt paving mixtures.

Signficant progress has been made in both laboratory characterization and modelling of bulk fracture in asphalt materials in recent years. For example, the use of notched asphalt specimens for localizing crack initiation and propogation has become very popular over the last ten years. Similarly, a large number of computational and analytical models have emerged that are capable of capturing the fracture processes within the asphalt macro and micro-structure. Models that are capable of accurately simulating asphalt materials over wider ranges of temperatures, loading rates, aging conditions and other effects have also emerged. When applied in practice, these advances will lead to significant improvements over empirical

test procedures and purely phenomenological modelling approaches that mainly consist of regression equations developed through data-fitting approaches using very specimen-centric or site-specific cracking observations, which are inherently biased by prevailing boundary conditions.

The titles and authors of the orginal contributions that were submitted for the characterization of fracture mechanisms in asphalt materials is as follows:

Laboratory Tests

Static Cracking and Damage

1. Fracture Energy Measurements Using Disk-Shaped Compact Tension Test (Buttlar et al.)

2. Fracture Energy Measurements Using Fenix Test (Perez-Jimenez et al.)

3. Validity of Time-Temperature Superposition Principle for Cracking in Bitumenous Mixtures (Di Benedetto et al.)

4. Dissipated Creep Strain Energy Density Measurements (Hernanado et al.)

Cyclic Cracking and Damage

1. 2 Point Bending Test (Maggiore, Marsac)

2. Complex Modulus and Fatigue Tests on Cantilever Trapezoidal Beam (Chabot, Hammoum)

3. Complex Modulus Testing Using Uniaxial Cylindrical Test (Di Benedetto et al.)

4. Uniaxial Test for determining Viscoelastic Continuum Damage model parameters (Kim et al.)

Constitutive Models

Crack Initiation and Propagation Models

1. Crack Growth Initiation Model (Dubois et al.)

2. Cohesive Zone Fracture Model (Behnia et al.)

3. Hot Mix Asphalt Fracture Mechanics Model (Hernando et al.)

Cyclic Degradation Models

1. Dissipated Energy Concept (Maggiore et al.)

2. Non-local Modeling of Fatigue Microcracking with Application to Specimen Size Effects (Marsac and Bodin)

3. Viscoelastic Continuum Damage Model (Kim)

2.2 LAB TESTS: STATIC CRACKING AND DAMAGE

This section describes three of the most recent static lab tests developed to evaluate cracking resistance in bituminous mixtures. Each subsection contains details regarding the theoretical background, specimen geometry and data interpretation methods.

2.2.1 Fracture Energy Measurements using Disk-Shaped Compact Tension Test and Compact Tension Test

The University of Illinois at Urbana-Champaign (UIUC) has developed a variety of tools to characterize the fracture properties of asphalt mixtures. This research has predominantly focused on the mechanisms related to reflective and thermal cracking. The experimental tests created at UIUC measure the fracture energy of mixtures to describe the work required to propagate an existing crack through the asphalt mastic and aggregate. The disk-shaped compact tension test (DC(T)), shown in Fig. 2.1(a), was developed by Wagoner et al. [1] to characterize the Mode I fracture behavior of conventional intermediate and surface layer asphalt mixtures. In addition, Ahmed et al. [2] adapted the compact tension (C(T)) test from the DC(T) geometry to evaluate the fracture properties of thin-bonded overlay (TBO) systems. Thin-bonded overlays are thin lifts of gap or dense graded asphalt concrete (less than 25 mm thick) placed immediately after the application of a heavy tack coat to promote greater adhesion between the overlay and underlying layers. The C(T) test determines the Mode I fracture properties of TBO systems by driving a crack vertically through the overlay as shown in Fig. 2.1(b).

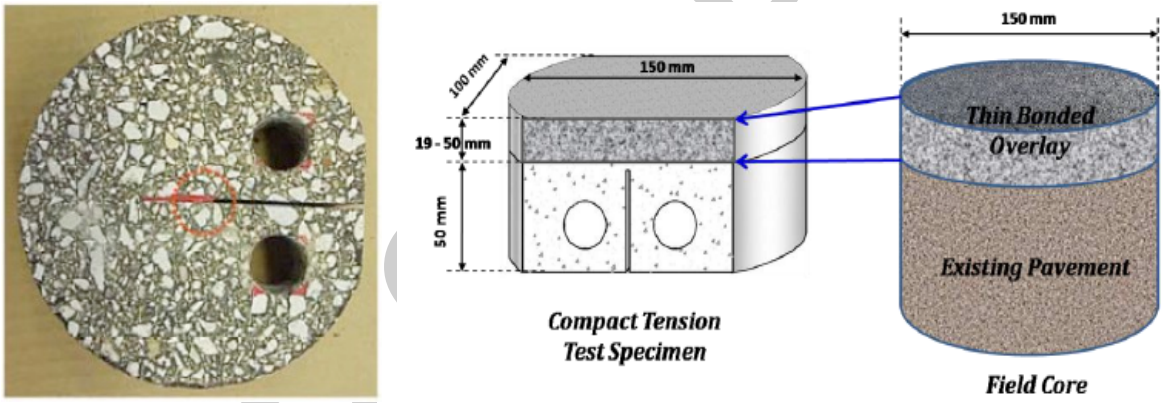

Fig. 2.1 **(a)** DC(T) Specimen **(b)** C(T) Specimen (Ahmed et al. [3])

2.2.1.1 Test Setup, Procedures, and Analysis

Wagoner et al. [1] proposed an adapted DC(T) geometry to characterize conventional asphalt mixtures, using the ASTM E399 standard as a starting point. This geometry, shown in Fig. 2.2, can be fabricated from 150 mm diameter field core or laboratory produced gyratory specimens and is specified in ASTM D7313-14. The C(T) geometry, provided in Fig. 2.1(a), can also be generated from 150 mm dia. field cores or gyratory specimens. However, the ligament length of the specimen varies from 19 to 50 mm depending on the thickness of the TBO system. Additionally, the C(T) specimen notch spans the thickness of the entire underlying layer such that the fracture energy of the specimen relates to the TBO system only.

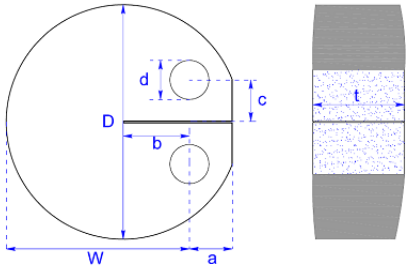

DC(T), Dimensions (mm)	
D	150
W	110
a	35
b	27.5
c	25
d	25
t	50

Fig. 2.2 Asphalt concrete DC(T) geometry [4]

The DC(T) and C(T) tests are controlled using a crack mouth opening displacement (CMOD) gauge. A constant CMOD rate of 1.0 mm/min is used to initiate and propagate a crack through the asphalt material, generally at temperatures less than 0 ºC. According to ASTM D7313-14, the testing temperature is recommended to be 10 ºC higher than the low temperature performance grade (PG) of the asphalt binder. The primary outputs of the DC(T) and C(T) tests are load-CMOD plots, CMOD fracture energy, and peak load. A plot of four Load-CMOD curves is provided in Fig. 2.3. The dissipated energy during cracking, i.e. global fracture energy (G_f), is calculated as:

$$G_f = \frac{W_D}{h \cdot l} \tag{2.1}$$

where G_f = dissipated energy during test application, (typically in units of J/m^2); W_D = dissipated work during test application; h = specimen thickness, l = initial ligament length. The dissipated work is calculated by measuring the area under the average Load-CMOD curve.

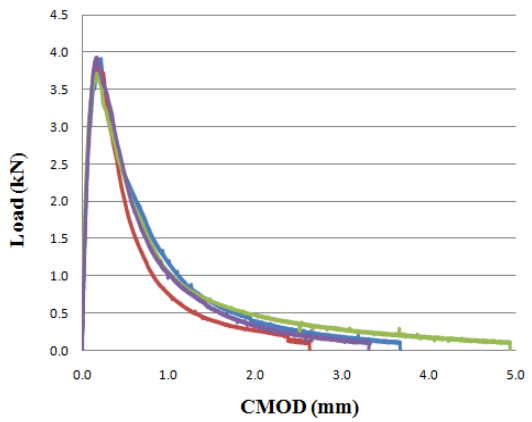

Fig. 2.3 Example load versus CMOD plots for asphalt mixtures

2.2.1.2 Examples of Test Results

Initial DC(T) studies evaluated the effects of testing rate, temperature, aging, and specimen size. Wagoner et al. [1] examined the effect of four rates, 10, 1, 0.5, and 0.1 mm/min, and three temperatures, 0, -10, and -20 ºC on CMOD fracture energy. Fracture energy was found to increase with temperature from 233 J/m^2 at -20 ºC to 470 J/m^2 at 0 ºC. In addition, fracture energy decreased with CMOD opening rate from 352 at 0.1 mm/min to 276 J/m^2 at 10 mm/min.

The increase in fracture energy due to the temperature increase likely occurred as a result of a combination of factors, including the decreasing brittleness (increasing ductility) of the

binder with temperature, the corresponding increase in the fracture process zone (and decreased structural brittleness), and increased proportion of viscous dissipation entering into the energy measurement. In addition, the inverse relationship between the fracture energy and loading rate was likely related to a reduced ability to relax stress during the shorter testing period. Wagoner et al. [5] assessed the effect of specimen size on fracture resistance. Varying specimen diameters and thicknesses were used. CMOD fracture energies increased from 400 to 600 J/m^2 and 250 to 550 J/m^2 with respective increases in diameter from 100 to 450 mm and thickness from 25 to 150 mm, despite normalizing for the size of the fractured area in the energy calculation (equation 2.1).

Braham et al. [6] considered the effect of laboratory oven aging of asphalt mixtures on DC(T) fracture energy. Researchers placed loose asphalt mixtures at temperatures of 135 ºC for 8 different oven aging periods ranging from 2 to 48 hours. Then, specimens were compacted and tested. Braham and his colleagues found CMOD-based total fracture energy to increase for oven aging times up to about 8 hours. This result was counter-intuitve at first, but closer examination showed a rise in peak load, and slight increase in the slope of the post-peak softening curve (decreasing Load-CMOD curve in the post-peak region). Creep compliance values obtained from testing in AASHTO T-322 indicated a decrease in creep compliance with aging level. Up to the 8 hour aging level, the energy increase associated with the peak load increase seems to outweigh the loss in energy due to the increased severity (slope) of the post-peak softening curve. After 8 hours of aging at 135 ºC, the post-peak softening behavior became quite severe (steep slope), more than offsetting the increased peak load, and leading to overall reduced fracture energy.

The DC(T) test has also been applied to sustainable materials such as reclaimed asphalt pavement (RAP) and warm mix asphalt (WMA) mixtures. Behnia et al. [4] found increased levels of RAP generally yielded decreased fracture energy. This result agreed with Braham et al. [6] as greater levels of aging or amounts of aged inclusions reduced the ability of the asphalt concrete to resist crack propagation above a certain load threshold. Furthermore, Hill et al. [7] found that the DC(T) test was able to distinguish among foaming, organic, and chemical WMA additives. In particular, this study found fracture energy to be more sensitive to additive type as compared to the reduced production temperatures of WMA.

Finally, Buttlar et al. [8] considered the relationship between transverse cracking and CMOD fracture energy. Researchers extracted field core samples at locations in which crack count surveys were conducted. The results are shown in Fig. 2.4 and produced a definitive correlation between fracture energy and transverse cracking. CMOD fracture energies in excess of of 400 J/m^2 were determined to represent a threshold associated with negligible levels of transverse cracking. Fracture energies below this value related to sections containing significant transverse cracking.

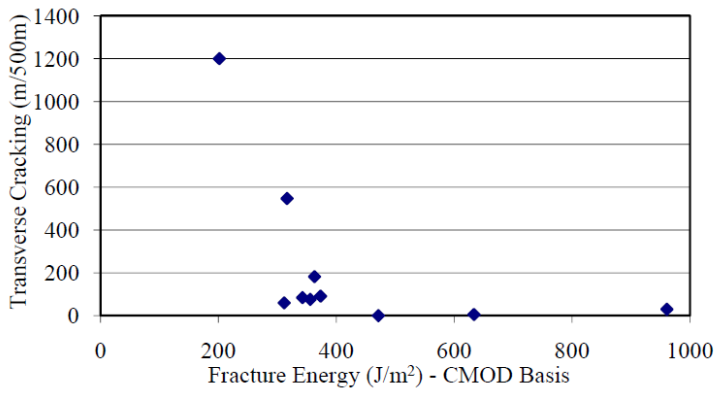

Fig. 2.4 Transverse cracking and DC(T) fracture energy relationship (Buttlar et al. [8])

The C(T) test has been successfully used to characterize gap and dense graded TBOs. Ahmed et al. [2] determined that C(T) tests conducted on gap graded TBO's showed significantly greater fracture energies when compared to dense graded overlays. This result likely occurred due to the upward migration of the tack coat into the gap graded mixture during compaction. Ahmed et al. [2] also evaluated dense grade TBO's constructed with conventional and spray paver construction techniques using the C(T) test. Results showed that sections constructed using the spray paver construction technique yielded fracture energies 39% greater than those constructed using traditional paving techniques. Testing also showed that samples obtained from sections constructed using a polymer modified asphalt binder as a tack coat had 40% higher fracture energies as compared to those constructed using unmodified asphalt emulsion. Finally, Ahmed [9] compared laboratory produced and field core based C(T) test specimens in terms of fracture energy. Results showed that samples obtained from field cores exhibited higher fracture energies than those manufactured in the laboratory.

2.2.2 Fracture Energy Measurements using Fenix Test

The Fenix test is a tensile test to evaluate cracking resistance of asphalt concrete mixtures by calculation of the dissipated energy during the cracking process. The test is named after the research project that funded the investigation: FENIX Project (www.proyectofenix.es).

The Fenix test represents a mode I type of fracture. It can be performed on laboratory samples or field cores. The typical test temperature applied is 20ºC, however it has been applied at lower temperatures such as, 5ºC, -5ºC, -10ºC, -15ºC and -25ºC. The displacement velocity its usually 1 mm/min but tests have been carried out at 10 mm/min, 0.1 mm/min and 0.03 mm/min.

By this definition, at below 0ºC temperatures the dissipated energy is equal or very close to the fracture energy, however when the test is performed at higher temperatures an important part of this energy is employed in deformation of the material and therefore it is not all used in the fracture of the specimen. The dissipated energy is calculated in the same way as for the DC(T) and C(T) tests (refer to Eq. 2.1).

Other mechanical parameters like peak load, F_{max}, displacement at peak load, Δ_{Fmax}, and displacement at 50% of post-peak load, Δ_{mdp}, are determined from the load-displacement curve (refer to Fig. 2.5). In order to obtain a stiffness related parameter from the test, the tensile stiffness index, IRT, is defined by Eq. 2.2:

$$IRT = \frac{\frac{1}{2} \cdot F_{\max}}{\Delta_m} \tag{2.2}$$

where IRT = tensile stiffness index (kN/mm); Δ_m = displacement before peak load at ½ F_{max}, (mm).

2.2.2.1 Test Setup, Procedures, and Analysis

The test procedure consists of subjecting one half of a 63.5 mm thick cylindrical specimen of a 101.6 mm diameter prepared by Marshall or gyratory compaction to a tensile stress at a constant displacement velocity and specific temperature. A 6 mm deep notch is made in the middle of its flat side where two steel plates are fixed. The specimen is glued to the steel plates with an adhesive mortar containing epoxy resins. Each plate is attached to a loading platen so that they can rotate about fixing points. Load and displacement data are recorded throughout the test to calculate the parameters involved in the cracking process. Fig. 2.6 shows finite element simulation of Fénix specimen.

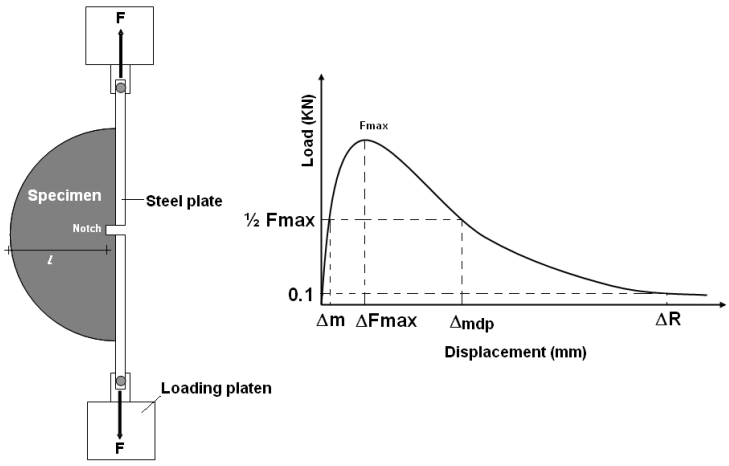

Fig. 2.5 Fénix test set up and load-displacement output curve

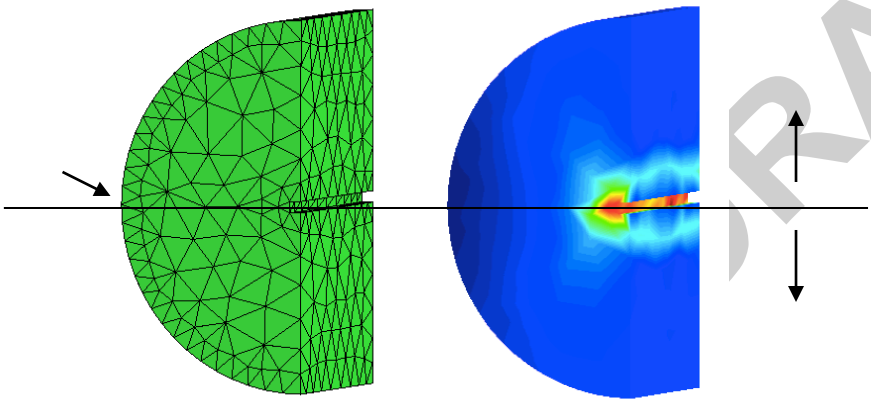

Fig. 2.6 Finite element simulation of Fénix specimen (using GID ® software)

2.2.2.2 Examples of Test Results

Figs. 2.7, 2.8, and 2.9 summarize the results of the effect of binder type and test temperature for a S20 mixture (AC22S). At a low temperature (-10ºC), this asphalt mixture exhibited a brittle behaviour with high peak load and low displacement values, Fig. 2.7. At 20ºC, a more ductile behaviour with higher displacement values, Δ_{mdp}, and low peak load, F_{max}, and stiffness, I_{RT}, values, can be observed (Fig. 2.9). At intermediate temperatures, 5ºC, the behaviour was also intermediate as seen in Fig. 2.8.

The results of dissipated energy during cracking, G_f, which is related to binder type and test temperature, reveal that BM3c mixture had the highest dissipated energy value at all temperatures, and therefore it is expected to have superior cracking behaviour. Mixtures obtained the largest dissipated energy value at 5ºC irrespective of the binder used, except for B13/22 mixture that had the highest dissipated energy value at 20ºC due to the higher stiffness of the binder. At lower temperatures a more brittle behaviour can be observed.

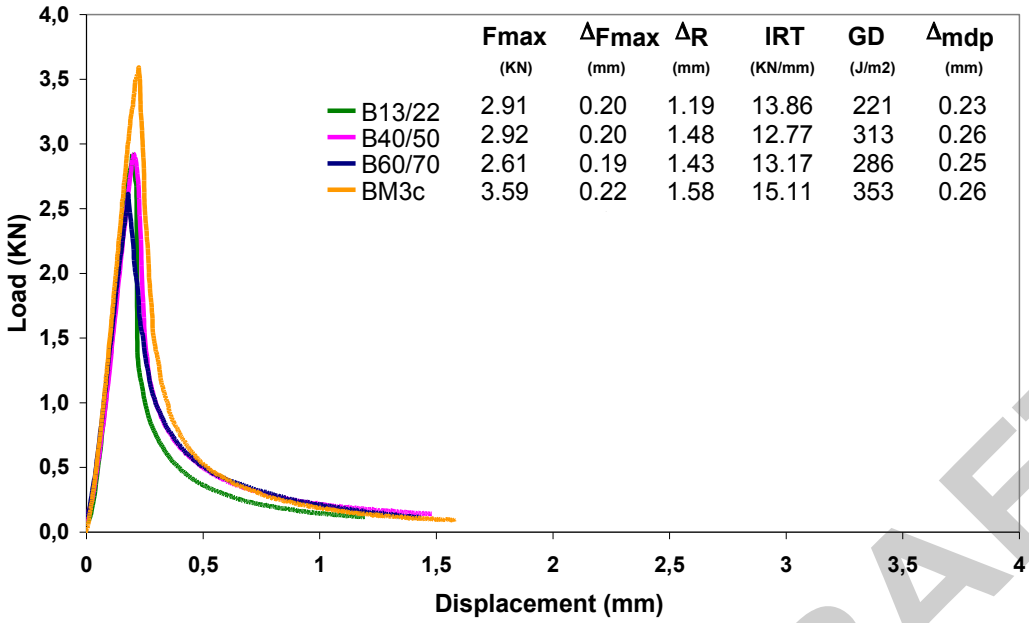

Fig. 2.7 Fénix test with different bitumen types, S-20 mixture at -10ºC

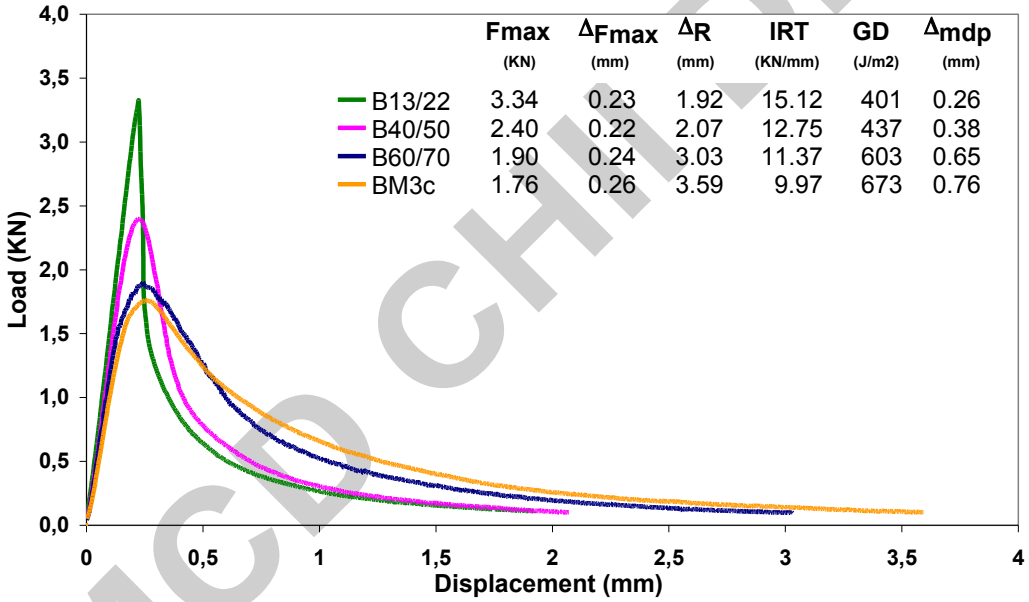

Fig. 2.8 Fénix test with different bitumen types, S-20 mixture at 5ºC

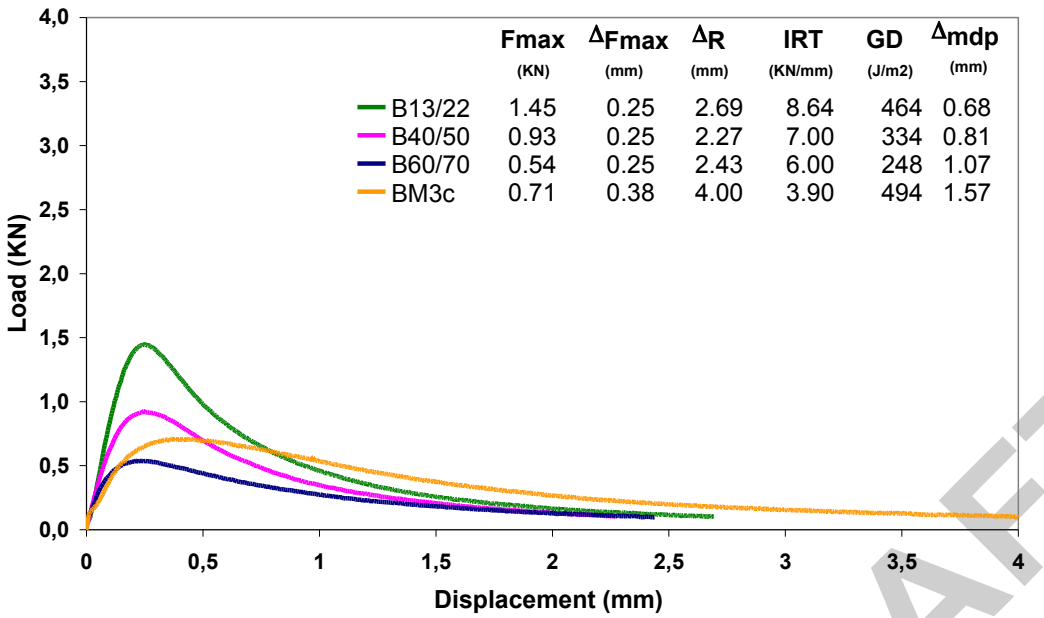

Fig. 2.9 Fénix test with different bitumen types, S-20 mixture at 20ºC

2.2.2.3 Repeteability and Sensitivity

Repeatability of the Fénix test was assessed by computing the coefficient of variation (COV) for each series of specimens tested. For dissipated energy, G_f, and maximum tensile load, F_{max}, COV mean values of 15 and 8.5% were obtained, respectively. Based on COV values for dissipated energy, the Fénix test seems to have good repeatability that is comparable to other fracture tests for asphalt mixtures. On basis of typical published results, the COVB ranges for other tests are 3-18% for SE(B), 4-25% for DC(T) and 15-34% for SCB tests (13).

Sensitivity of the Fénix test was evaluated by a variance analysis (ANOVA) of the results for dissipated energy obtained in the experimental tests. With ANOVA it is possible to find out whether the values of a set of numerical data are significantly different from those of other sets. Thus, test sensitivity for a specific parameter can be determined.

In the first stage, test sensitivity of S-20 mixture to binder type and test temperature was analyzed from the results obtained for dissipated energy during cracking in the Fénix test. A variance analysis of two factors, i.e. binder type and test temperature, was performed with several samples per group. Binder type levels were B60/70, B40/50, B13/22 and BM3c, with 9 data for each level; test temperature levels were -10, 5 and 20ºC, with 12 data for each level. As can be seen in Table 2.1, the F ratio for binder type and test temperature factors, like for the interaction between both factors, is greater than its critical value determined for a significance level of 0.05. This means that for each evaluated factor, as well as in the interaction between them, significantly different values are obtained for dissipated energy, G_f. Thus, test sensitivity to factors analyzed at this stage is determined.

Table 2.1 ANOVA Comparison of Dissipated Energy, G_F, with Bitumen Type and Test Temperature. S-20 mixture (AC22 S)

Source of Variation	SS	DF	MS	F-Value	P-Value	Critical F-Value
Bitumen Type	132414.178	3	44138.059	20.42	8.59 •10-07	3.0088
Test Temperature	337020.377	2	168510.188	77.95	3.18 •10-11	3.4028

Interaction	167925.278	6	27987.546	12.95	1.66 •10-06	2.5082

Analogously, in the second stage test sensitivity of G-20 mixture to binder content and test temperature was tested. As in the previous case, a variance analysis of two factors, i.e. binder content and test temperature, was conducted with several samples per group for each binder type (B60/70, B40/50 and B13/22). Binder content levels were 3.5, 4.5 and 5.5%, with 9 data for each level; test temperature levels were -10, 5 and 20ºC, with 9 data for each level.

From Table 2.2, it can be concluded that, for binder content and test temperature, significantly different values of dissipated energy during cracking, G_f, are obtained in the Fénix test. Thus, test sensitivity to factors analyzed at this stage is determined.

Table 2.2 ANOVA Comparison of Dissipated Energy, G_F, with Bitumen Content and Test Temperature. G-20 mixture (AC22 G)

Bitumen Type	Source of Variation	SS	DF	MS	F-Value	P-Value	Critical F-Value
B60/70	Bitumen Content	112047.73	2	56023.865	5.2324	1.62 • 10-02	3.5546
	Test Temperature	1465290.22	2	732645.111	68.4263	3.87 • 10-09	3.5546
	Interaction	103244.73	4	25811.183	2.4107	8.71 • 10-02	2.9277
B40/50	Bitumen Content	181021.95	2	90510.974	6.9033	5.95 • 10-03	3.5546
	Test Temperature	581451.24	2	290725.619	22.1736	1.39 • 10-05	3.5546
	Interaction	154442.81	4	38610.701	2.9448	4.91 • 10-02	2.9277
B13/22	Bitumen Content	588307.52	2	294153.761	45.0689	9.81 • 10-08	3.5546
	Test Temperature	1104949.06	2	552474.530	84.6477	6.99 • 10-10	3.5546
	Interaction	173596.07	4	43399.019	6.6494	1.81 • 10-03	2.9277

2.2.3 Four Point Bending Notch Fracture

Crack propagation in bituminous mixtures using four point bending notch has been designed at University of Lyon/ENTPE. One of the main features of this test is that the middle one third of the beam is subjected to pure bending (constant momentum) without any shear deformation.

2.2.3.1 Test Setup, Procedures, and Analysis

The test set up together with the tested pre-notched prismatic beams dimensions are shown in Fig. 2.10.

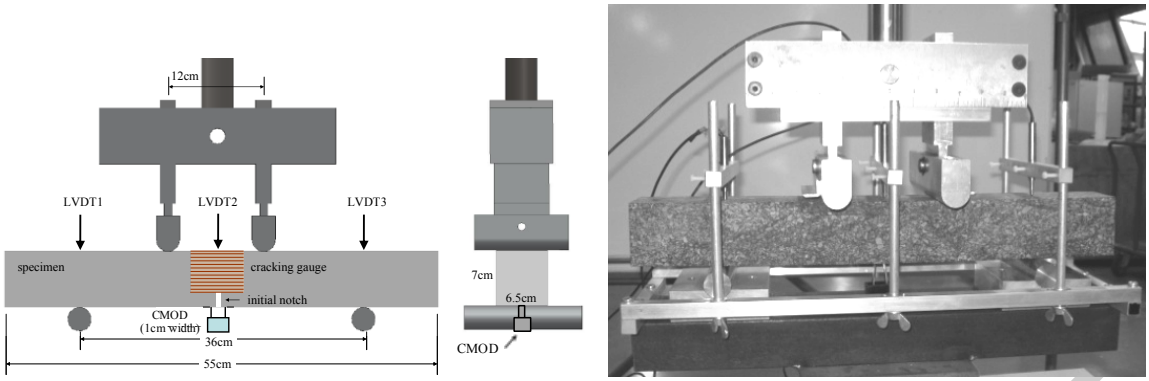

Fig. 2.10 Four point bending test performed at University of Lyon/ENTPE

An initial notch of height "a_0" is made in the middle of the beam. This height assures stable crack propagation. The same ligament size (W-a_0) of about 5 cm (value used in previous study by Nguyen et al. [10]) is obtained for all specimens. As the energy needed for crack initiation is dependent of the initial notch edge shape, great care is taken to create it. It is performed in two steps. First, a circular saw is used to obtain a $a_0 - 0.5\ cm$ deep and 5 mm thick notch. Then the last 0.5 cm is made with a hacksaw to obtain a thinner crack tip of 1 mm thickness. Table 2.3 provides initial notch values (a_0) as well as ligament (W-a_0) of each considered specimen.

Table 2.3 Size of pre-notch and ligament for the tested specimens

Specimen	Initial notch a_0 (cm)	Ligament W-a_0 (cm)
ENTPE2	3.10	4.7
ENTPE4	1.90	5.3
ENTPE7	2.27	5.0
ENTPE8	2.63	4.9

A servo-hydraulic machine is used to perform the tests. The displacement of the piston (u) (measured by an integrated transducer) is used as the feedback signal for the considered tests. However, any other sensors may be used to monitor the test (crack opening or other). Monotonic tests as well as loading-unloading cyclic tests can be applied. A 10kN load cell measures the applied load (P).

A thermal chamber is used to control the temperature. The temperature inside the chamber may be regulated from -50°C to 80°C. A thermal gauge is fixed on the specimen to measure its surface temperature.

Three linear variable differential transducers (LVDT) are used to measure displacements on top of the beam: deflection in the centre of the beam, *LVDT2*, and vertical displacements at the two lower supports, *LVDT1* and *LVDT3* (see Fig. 2.10). The range of the used LVDTs is 5 cm. Measurements by *LVDT1* and *LVDT3* give displacements due to punching effect of the two lower supports on the beam. As the same load is applied by each upper and lower support displacement due to punching effect can be taken into account and corrected. The "true" deflection of the beam, called f, is then obtained by:

$$f = \mathrm{LVDT2} - \frac{\mathrm{LVDT1} + \mathrm{LVDT3}}{2} \tag{2.3}$$

An extensometer is used to measure the crack mouth opening displacement (CMOD) at the top of notch. It is placed under the beam (see Fig. 2.10).

An important measurement is the crack length evolution during the test. In order to follow the crack propagation the cracking gauges are used. These gauges are constituted of 21 parallel wires separated each other by 2.5 mm (Fig. 2.11 left). The wires are designed to break sequentially as the crack propagates in the specimen, which indicates the crack tip position (Fig. 2.11 right). The gauges used are 8 cm long and 5 cm high. One gauge is glued on each lateral side of the specimen.

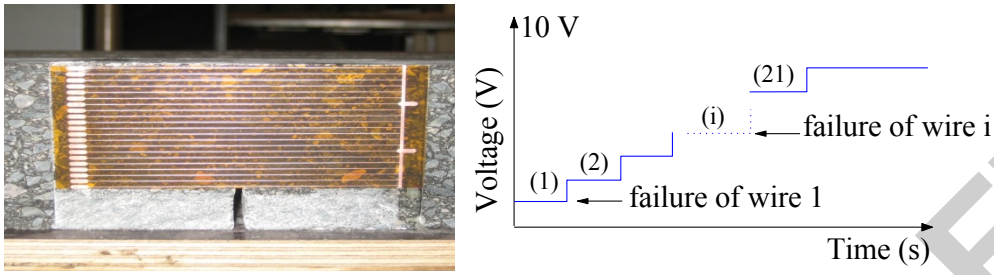

Fig. 2.11 (Left): Cracking Gauge Glued On The Specimen; And (Right): Typical Measured Voltage–Time Curve When Crack Propagates

The four point bending test is conducted with constant imposed displacement rate of the piston. The displacement rate fixed for each test is chosen depending on the test conditions as described further. The realization of the test takes place in two stages.

First, two cycles of loading/unloading are carried out to allow setting of specimen inside the loading frame. The maximum loading value during these two cycles is P_{1max} = 0.8 kN, which is relatively small (less than a third of the failure value). The minimal value is P_{2min} = 0.2 kN. Then, after these loading/unloading cycles, monotonic loading is applied at constant displacement rate of the piston, until the final failure of the beam. Fig. 2.12 shows the typical obtained response of load versus time. Fig. 2.13 presents result in the axes load vs. displacement of piston, for the same test as Fig. 2.12 (test ENTPE7).

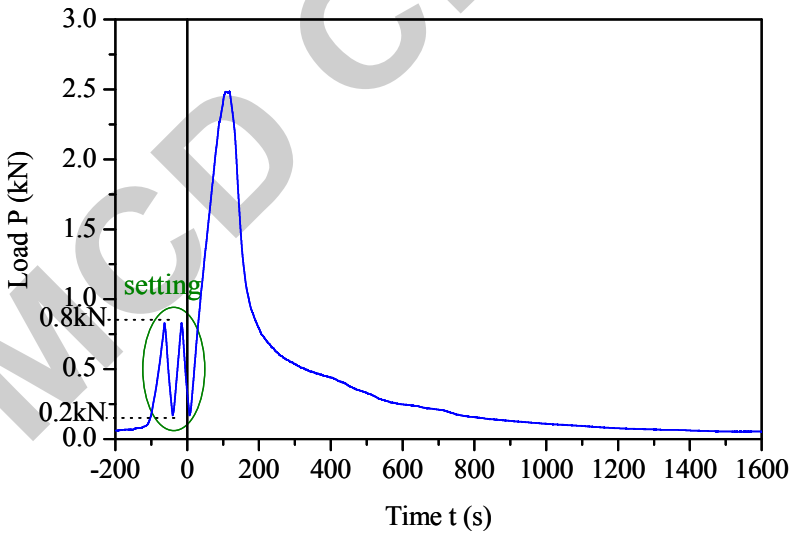

Fig. 2.12 Loading path during the crack propagation test (ENTPE7: v = 5.9mm/min; T = -1.5°C)

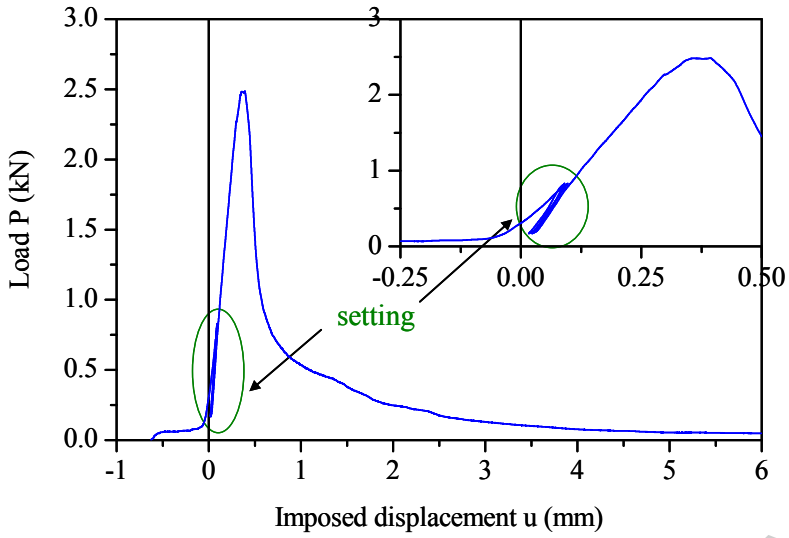

Fig. 2.13 Load – displacement curve obtained for test ENTPE7: v = 5.9mm/min; T = -1.5°C (same test as Fig. 2.12)

The determination of the crack length follows a type of measurement that has been applied in many previous studies (Lemaistre [11]; Jiang et al. [12]; Wendling et al. [13]; Nguyen et al. [10]).

As one gauge is used on each side of the specimen, two different values of crack length are obtained, noted a_{gauge1} and a_{gauge2}. Results given by the two cracking gauges are plotted in Fig. 2.16, for test ENTPE7 already chosen in Fig. 2.12 and 2.13. As shown in Fig. 2.16, some differences appear between the two values a_{gauge1} and a_{gauge2}. The measured crack length is slightly different on each side. The crack may also have a different evolution inside the beam.

A drawback of this method is that detection of crack is delayed due to the relatively higher ductility of the gauge wires as compared to asphalt concrete. Only macro-cracks above a certain minimal width can be detected. Fig. 2.16 shows clearly that, the detected macro-crack using cracking gauges, appears after the peak of the load. This result probably does not reflect the reality. To address this shortcoming, a novel method was developed by the authors. The DRCL (Displacement Ratio method for predicting Crack Length) method is a new approach which makes it possible to calculate the crack length during the four point bending crack propagation test [10]. This method is based on the relation between two measured displacements: the crack mouth opening displacement "*CMOD*" and the deflection of the beam "*f*". The ratio between *CMOD* and *f* is called r_d:

$$r_d = \frac{CMOD}{f} \tag{2.4}$$

The DRCL method was developed at DGCB laboratory of University of Lyon/ENTPE and was introduced for the first time for cyclic tests then extended to monotonic loading cases. During analysis of cyclic tests, it was observed that linear extrapolation of the linear part of the reloading branch passes through the origin in the axes CMOD-f. Linear viscoelastic behaviour, without crack propagation can be reasonably assumed for the material, during this reloading period.

The second part of this method relies on FEM calculation considering the hypothesis of isotropic linear elastic behaviour. The calculation is made in order to determine the displacements field in the beam during the test. When considering the boundary conditions imposed on the beam (Fig. 2.11 left), it can be shown that the displacement and the strain fields are the same for elastic or viscoelastic materials [14] if the crack does not propagate.

The fields are independent of the modulus value of the material. They only depend of the fixed crack length.

The Finite Element Method (FEM) software COMSOL is used for the calculation, which is described in detail in Nguyen [15] and Tapsoba [16]. The calculation is repeated for different values of crack length *a*, in order to obtain the displacement ratio r_d (Eq. 2.4) as a function of the crack length *a* (Fig. 2.14b).

The last part of the method consists in linking the measured experimental ratio r_d with the crack length *a* considering relation of Fig. 2.14b.

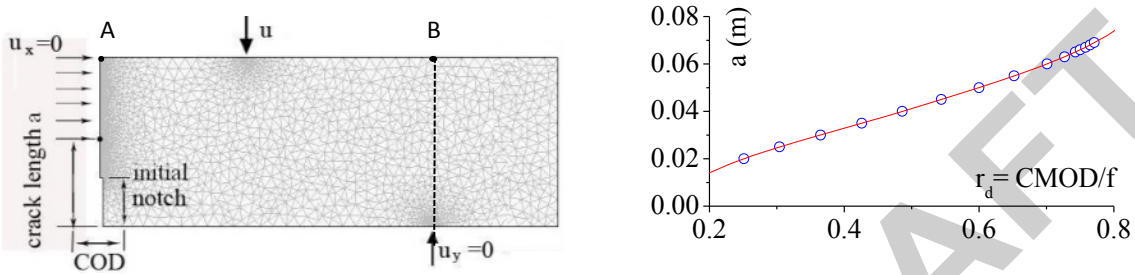

Fig. 2.14 **(a)**: boundary conditions and mesh used in FEM calculation: vertical displacement at A and B points and CMOD displacement computed; **(b)**: displacement ratio r_d values calculated by FEM as a function of crack length *a*

The DRCL method can also be applied to monotonic (non-cyclic) test data, as considered in this study. In that case, a crack length can be obtained from any point of the monotonic curve of CMOD versus f, as explained in Fig. 2.15. Then the crack length evolution is obtained during the entire monotonic loading test.

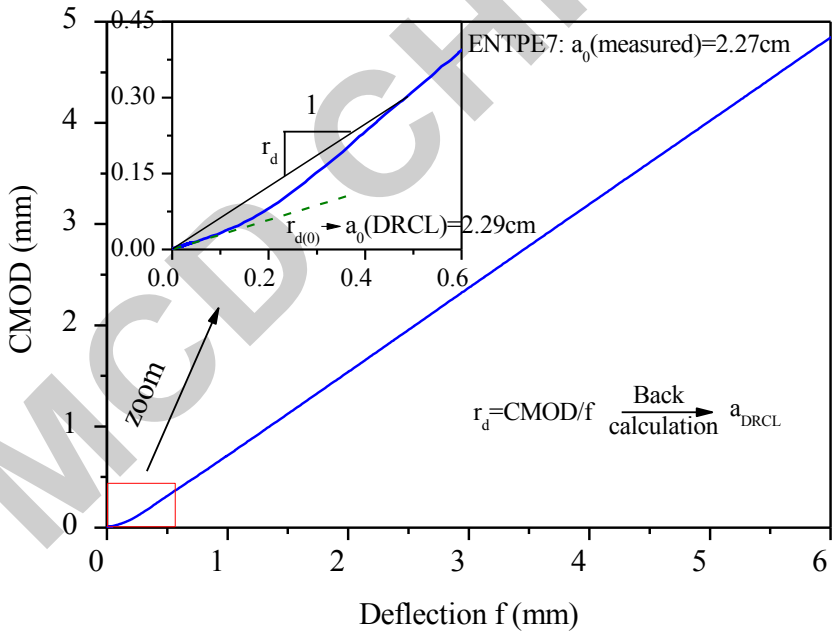

Fig. 2.15 Calculation of the crack lengths "a_{DRCL}" thanks to the displacement ratios r_d determined from the CMOD-f curve during monotonic loading test (test ENTPE7)

2.2.3.2 Results

Fig. 2.16 presents a comparison of the crack length obtained from cracking gages (a_{gauge}) and by DRCL method (a_{DRCL}) for ENTPE7 test (same test as presented in Fig. 2.12, 2.13 and 2.15). The evolution of crack length calculated by the DRCL method (a_{DRCL}), also plotted in

Fig. 2.16, is slightly different from the evolution of crack length obtained by the cracking gauges (a_{gauge1} and a_{gauge2}). A significant difference can be noted at the beginning of the test.

At the beginning of the curve: the deflection f increases, but the calculated crack a_{DRCL} remains constant. The accuracy of the method is confirmed by the value of this calculated initial pre-notch, whose value is quite close to the measured initial notch (for example : 2.29 cm to be compared to 2.27 cm for test ENTPE7 in Fig. 2.15). The calculated crack clearly starts to propagate (point A in Fig. 2.16) before the load reaches its peak value (point B in Fig. 2.16). Whereas, cracking gauges detect initiation of the crack (points C_1 and C_2 in Fig. 2.16) after the peak of the load. It is well admitted that, before macro-crack propagation, an initiation phase exists where damage occurs [17]. Only micro-cracks develop. Some studies showed that large damage occurs before the peak of the load – deflection curve, which can be considered as the start of macro-crack propagation [18][19][13]. The crack length calculated by the DRCL method could be considered as the sum of the macro-crack and a fictitious crack representing the damage zone at the crack tip. More details of the crack propagation mechanism evaluated by the DRCL method are presented in Nguyen et al. [10] and Nguyen [20].

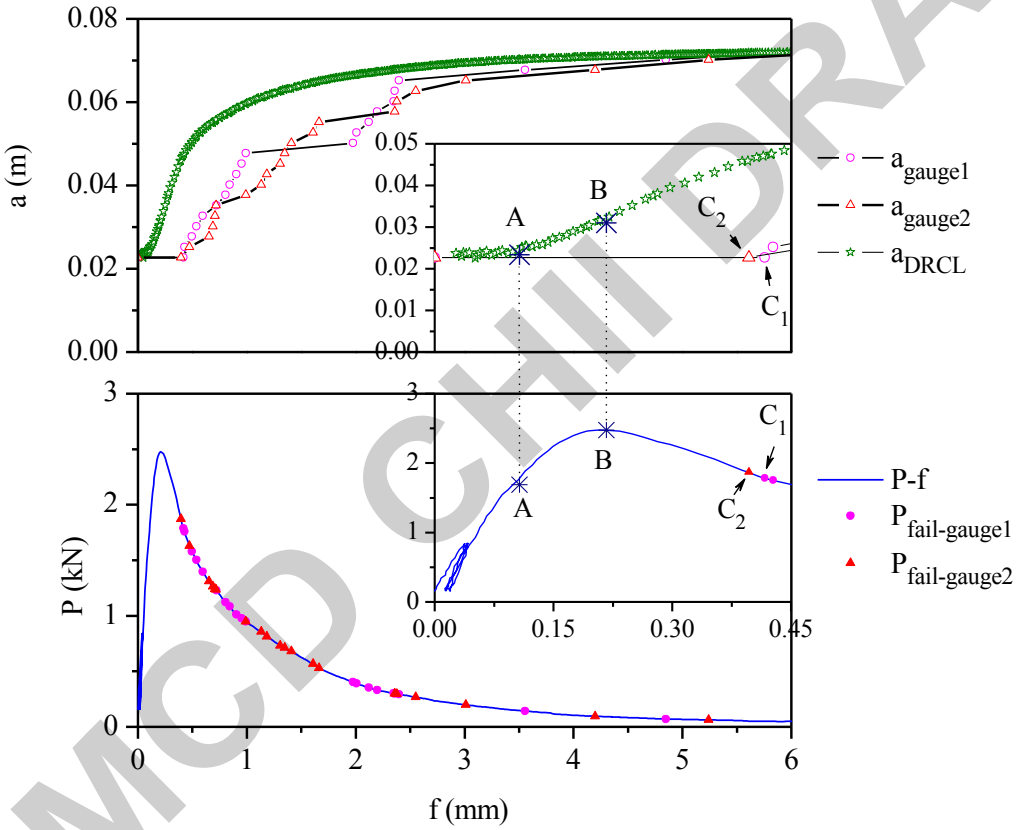

Fig. 2.16 ENTPE7 test: v = 5,9mm/min ; T = -1,5°C. (above): crack length in function of deflection of the beam. a_{gauge1}, a_{gauge2}: crack length measured by cracking gauges 1 and 2 respectively; a_{DRCL}: crack length obtained by the DRCL method; (below): load – deflection curve P -f. $P_{fail\text{-}gauge1}$, $P_{fail\text{-}gauge2}$: points located on the P - f curve where a wire fails for gauge1 and gauge2 respectively

2.2.3.3 Summary

The DC(T) and C(T) tests are viable monotonic fracture tests available to characterize thermal and reflective cracking. Each test produces repeatable fracture energy results with coefficients of variation generally less than 15%. The DC(T) test has shown the ability to

classify a variety of mixtures from RAP to WMA and to relate to transverse cracking in the field. Similarly, the C(T) test displayed the potential to differentiate among various TBO's and tack coat types. Few limitations are present with these tests. The most prominent limitations are the lack of mode mixity available with the tests and the lack of knowledge regarding deformation and stress states across the entire specimen during loading. Future extensions with these tests include the employment of digital image correlation to evaluate full field fracture behavior.

The Fenix test is an easy procedure that allows to compare the cracking resistance of different mixtures at different temperatures in terms of their dissipated energy or fracture energy and their tensile stiffness index (IRT). The procedure presents a good repeatability and it is sensitive to changes in temperature, binder type and binder content of the mixture. Furthermore, the mechanization of the specimen and their geometry makes possible to test not only lab specimens but also field cores. The four-point bending notch fracture test is another promising method to characterize Mode I fracturing of asphalt concrete. The novel DCRL method is a convenient and accurate method to characterize crack growth in this test and related fracture tests, including cyclic and monotonic types.

2.3 LAB TESTS: CYCLIC CRACKING AND DAMAGE

2.3.1 Complex Modulus Testing using Uniaxial Cylindrical Test Test Setup, Procedures and Analysis

Complex modulus can be measured in different loading modes. Here the measurement of complex modulus using the test configuration designed by the DGCB laboratory of University of Lyon/ENTPE [21-24] is presented. The test consists in applying on cylindrical specimen, sinusoidal axial strain at different temperatures and frequencies. Axial stress (σ) is measured from a load cell. Axial strain (ε_{ax}) and radial strain (ε_{rad}) are obtained from non-contact displacement transducers (Fig. 2.17).

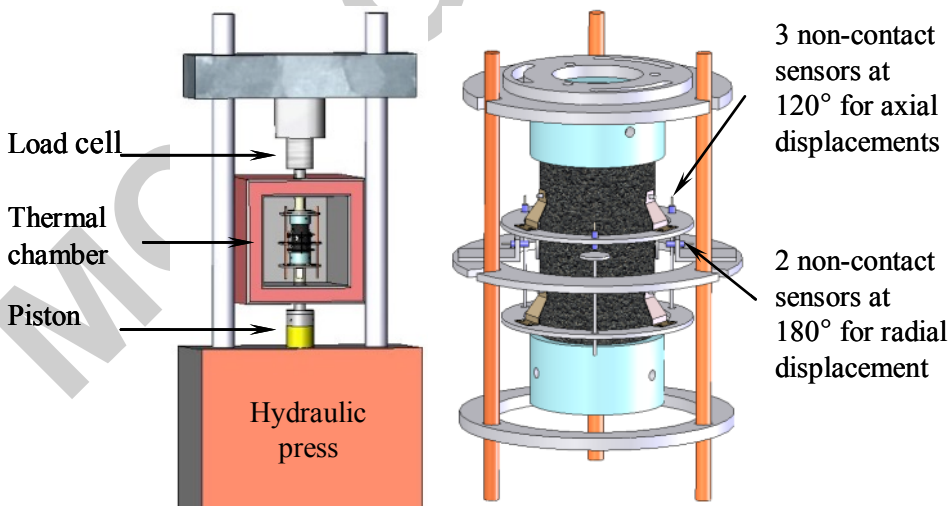

Fig. 2.17 Experimental device used for complex modulus test: general view (left) and specimen view (right)

Small axial strain amplitudes (less than 10^{-4} m/m) were applied ensuring the behaviour remained inside the linear domain. The following Eq. (2.5) gives the sinusoidal evolution of the stress and strain measured with time (t).

$$\begin{cases} \sigma(t) = \sigma_0 \sin(\omega t + \phi_E) \\ \varepsilon_{ax}(t) = \varepsilon_{0ax} \sin(\omega t) \\ \varepsilon_{rad}(t) = \varepsilon_{0rad} \sin(\omega t + \pi + \phi_\nu) = -\varepsilon_{0rad} \sin(\omega t + \phi_\nu) \end{cases} \tag{2.5}$$

where ϕ_E is the classical phase angle between the axial strain and the axial stress, ϕ_ν is the phase angle between the axial strain and the opposite of radial strain, ω is the pulsation ($\omega=2\pi*frequency$).

Considering the complex notations where j is the complex number ($j^2 = -1$), the measured values are written in Eq. (2.6).

$$\begin{cases} \sigma^*(t) = \sigma_0 e^{j(\omega t+\phi_E)} \\ \varepsilon^*_{ax}(t) = \varepsilon_{0ax} e^{j(\omega t)} \\ \varepsilon^*_{rad}(t) = -\varepsilon_{0rad} e^{j(\omega t+\phi_\nu)} \end{cases} \tag{2.6}$$

The complex modulus E^* and the complex Poisson's ratio ν^* are obtained from Eq. (2.7).

$$\begin{cases} E^*(\omega) = \dfrac{\sigma^*(t)}{\varepsilon^*_{ax}(t)} = \left|E^*(\omega)\right| e^{j\varphi_E} = \dfrac{\sigma_0}{\varepsilon_{0ax}} e^{j\varphi_E} \\ \nu^*(\omega) = -\dfrac{\varepsilon^*_{rad}(t)}{\varepsilon^*_{ax}(t)} = \left|\nu^*(\omega)\right| e^{j\varphi_\nu} = \dfrac{\varepsilon_{0rad}}{\varepsilon_{0ax}} e^{j\varphi_\nu} \end{cases} \tag{2.7}$$

The specimen is loaded at 6 different frequencies (from 0.03 to 10 Hz) and 8 different temperatures (from -20 °C to 35 °C).

2.3.1.1 Test Results

The norm of complex modulus $|E^*|$ and its phase angle ϕ_E (and norm of complex Poisson's ratio $|\nu^*|$ and its phase angle ϕ_ν, respectively) are presented in Fig. 2.18 (Fig. 2.19, respectively) for the tested material. It can be seen (Fig. 2.19) that the norm of the complex Poisson's ratio $|\nu^*|$ is not a constant as generally admitted for pavement design. For the considered mixture, $|\nu^*|$ varies from about 0.17, for high frequencies and/or low temperatures, to 0.35, for low frequencies and/or high temperatures. It decreases when temperature decreases and when frequency increases.

Fig. 2.19 also confirms results already pointed out by Nguyen et al. [10] and Pouget et al. [25], the phase angle of the complex Poisson's ratio ϕ_ν is very small and negative but not nil as it is generally supposed in the literature. Negative values of ϕ_ν mean that the radial strain is slightly delayed compared with the axial strain, which appears as physically acceptable.

As mentioned in the introduction, many researchers considering only unidirectional experiments have shown for this monodimensional limited case that bituminous mixtures respect the time – temperature superposition principle (TTSP) in the small strain domain, where the behaviour can be considered as linear viscoelastic (LVE). Application of this principle enables to plot a master curve at a given reference temperature (T_R). This complex modulus master curve is constructed by shifting along the frequency axis the complex modulus values obtained at different temperatures. The master curve of E^* at the reference temperature -10.3°C obtained for tests on specimen MCE1 is plotted in Fig. 2.18, which also shows the master curve of the phase angle ϕ_E at the same reference temperature

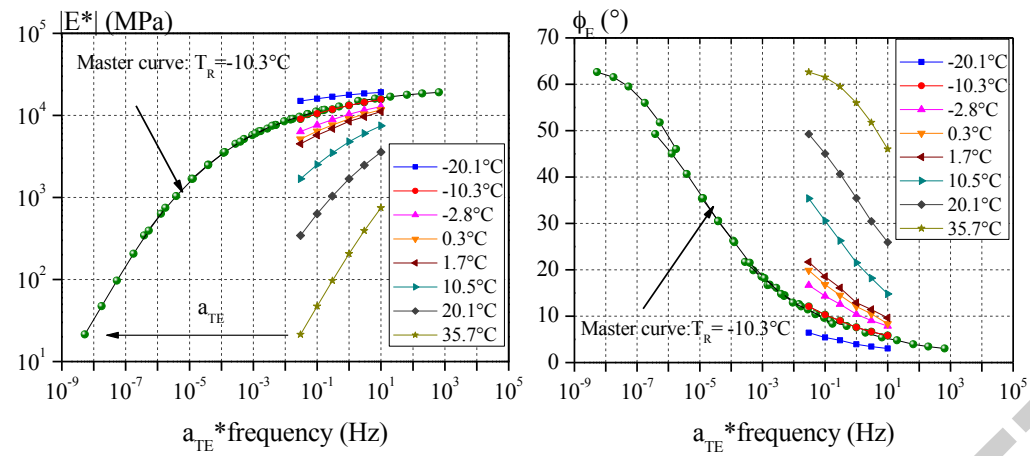

Fig. 2.18 Experimental values (test MCE1) of complex modulus E^* and master curves, plotted at reference temperature of -10.3°C. (Left): Norm of complex modulus $|E^*|$; (right): phase angle ϕ_E

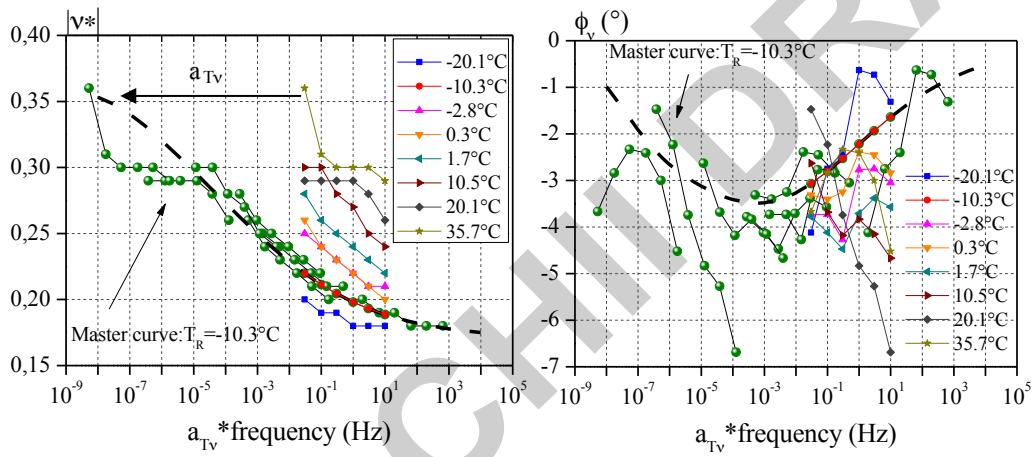

Fig. 2.19 Experimental values (test MCE1) of complex Poisson's ratio ν^* and master curves, plotted at a reference temperature of -10.3°C with $a_{T\nu}$ values equal to a_{TE} values previously determined (Fig.4). (Left): norm of complex Poisson's ratio $|\nu^*|$; (right): phase angle ϕ_ν

An interesting output of this test is that the unidirectional result can be extended to the three dimensional case. Fig. 2.19 shows that a master curve can also be obtained for the complex Poisson's ratio ν^* and its phase angle ϕ_ν. Some scatter appears in this Fig. 2.19. It can be explained by the practical difficulty for measuring Poisson's ratio, as involved strain levels remain very low. Furthermore, the shift factors used for complex Poisson's ratio ($a_{T\nu}$) are identical to the shift factors obtained for complex modulus (a_{TE}). This experimental result confirms the same tendency observed in recent studies [22][26][27]. An important output is that a unique shift factor can be considered in Eq. (2.8).

$$a_T = a_{TE} = a_{T\nu} \tag{2.8}$$

The classical WLF law (Williams, Landel and Ferry) [28] is used to fit the shift factors a_T in Eq. (2.9). The results are plotted in Fig. 2.20.

$$\log(a_T) = \frac{-C_1(T - T_R)}{(T - T_R) + C_2} \tag{2.9}$$

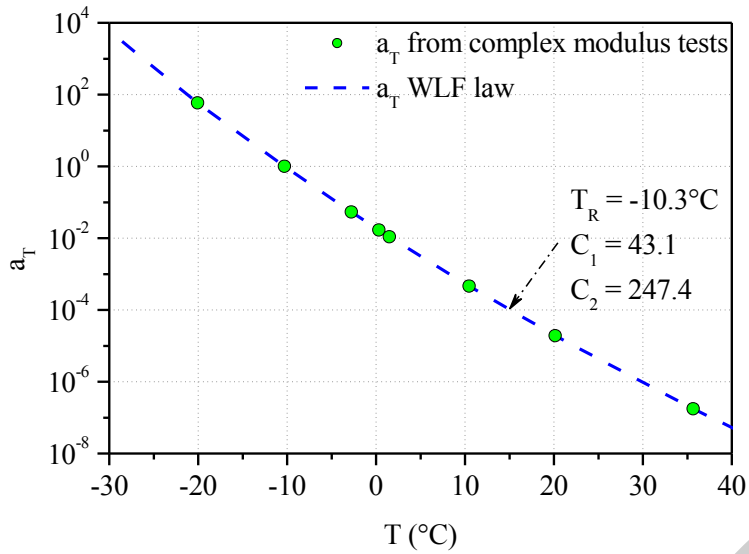

Fig. 2.20 Shift factors a_T of complex modulus and complex Poisson's ratio. Comparison with WLF law prediction for the test MCE1

2.3.2 Complex Modulus and Fatigue Testing using Cantilever Trapazoidal Beam Test

2.3.2.1 **Complex Modulus** *Testing: Specimen Geometry and Equipment*

During the round robin testing of asphalt mixtures for the RILEM TC CAP due to smaller thickness of each layer, the sawing procedure (NF P 98-250-3:1992) had been adapted for Illinois materials to extract the specimen horizontally in each layer. For each slab, 8 specimen are sawn, 4 for each layer (refer to Fig. 2.21).

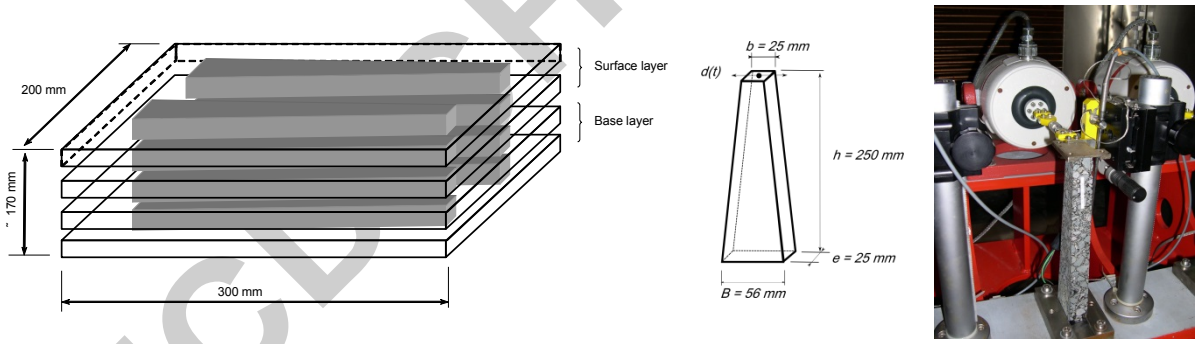

Fig. 2.21 Specimen Geometry and equipment (http://www.lcpc.fr/english/products/catalogue-of-mlpc-r-equipment/fiche-268/article/3mc-1112)

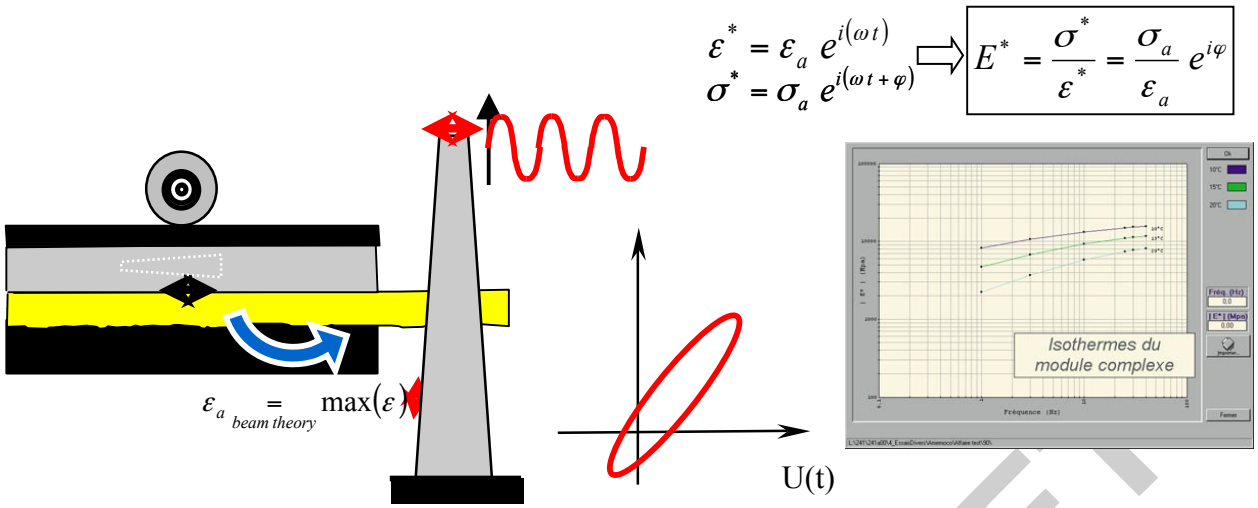

Fig. 2.22 Experimental setup [29]

2.3.2.2 Complex Modulus: Brief Test Description

Evaluation of the complex modulus of the materials has been performed according the current European standard EN 12697-26 on cantilever trapezoidal specimens (Fig. 2.23). Materials extracted from the two layers are lightly different. The top layer material's is "stiffer" than the top layer ones. This difference is logically correlated to the difference of void content of the two layers evaluated on the two sets of specimen (around 2%).

This test is a French standard test for the behaviour characterization of bituminous material and is systematically carried out to provide the information required for product standards (modulus at 15°C, 10 Hz) for the French Design method [30]. It allows for the determination of linear viscoelastic performance of bituminous materials depending on their frequency and operating temperature ranges. Four specimens can be tested simultaneously on the 3MC device within the following maximum temperature and frequency ranges: from -10°C to 60°C and from 1 to 40 Hz so as master curve can be drawn. The results are used to set some rheological models before bituminous material modelling.

Rheology of bituminous materials is strongly dependent of loading time and temperature. Interrelationship between frequency and temperature for these materials makes possible to get the same mechanical behaviour in different experimental conditions. Hence, mechanical properties, determined at high loading time (or low frequency) and at low temperature, can be found at low loading time (or high frequency) and at high temperature. In some cases (thermo rheologically simple bituminous materials) the equivalency between time and temperature allows to build master curve from linear viscoelastic data by shifting measurement at different temperature in order to obtain a continuous curve at a reference temperature [31]. The mechanical behaviour of asphalt materials is assumed to be linear thermo-viscoelastic and represented by the five viscoelastic coefficients $E_0^i, E_\infty^i, k_i, h_i, \delta_i$ and the three thermal coefficients A_0^i, A_1^i, A_2^i of the complex modulus of the Huet- Sayegh model [32-33] for the layer i. The Huet-Sayegh model consists in two parallel branches. The first branch is made up of a spring and two parabolic dampers that give the instantaneous and the retarded elasticity of asphalt, respectively. The second one is made up of a spring and it represents the static or the long-term elasticity of asphalt. Parameter E_∞ is the instantaneous elastic modulus, E_0 is the static elastic modulus, k and h are the exponents of the parabolic dampers $(1 > h > k > 0)$, and δ is a positive adimensional coefficient balancing the contribution of the first damper in the global behaviour. By means of parabolic creep laws associated to the two dampers, this

rheological model predicts very accurately the complex modulus test obtained for asphalt mixes at different temperatures and frequencies.

The coefficients of the Huet-Sayegh model can be determined from experimental tests and by using the free software Viscoanalyse [31] (see http://www.lcpc.fr/francais/produits/lcpc-produits-viscoanalyse/). For 3D pavement analysis, a semi-analytical multi-layered solution using Fast Fourier Transforms and the linear behaviour of the Huet-Sayegh model for asphalt materials has been written in the free software ViscoRoute. ViscoRoute 2.0 enables users to consider multiple moving loads and elliptical-shaped loads [34] (see http://www.lcpc.fr/francais/produits/lcpc-produits-viscoroute-2-0/).

2.3.2.3 Fatigue Testing: Specimen Geometry and Laboratory Device:

Due to the thickness of each layer, the sawing procedure (NF P 98-250-3:1992) has been adapted to extract the specimen horizontally in each layer. For each slab, 8 specimen are sawn, 4 for each layer. The experimental setup is shown in Fig. 2.24.

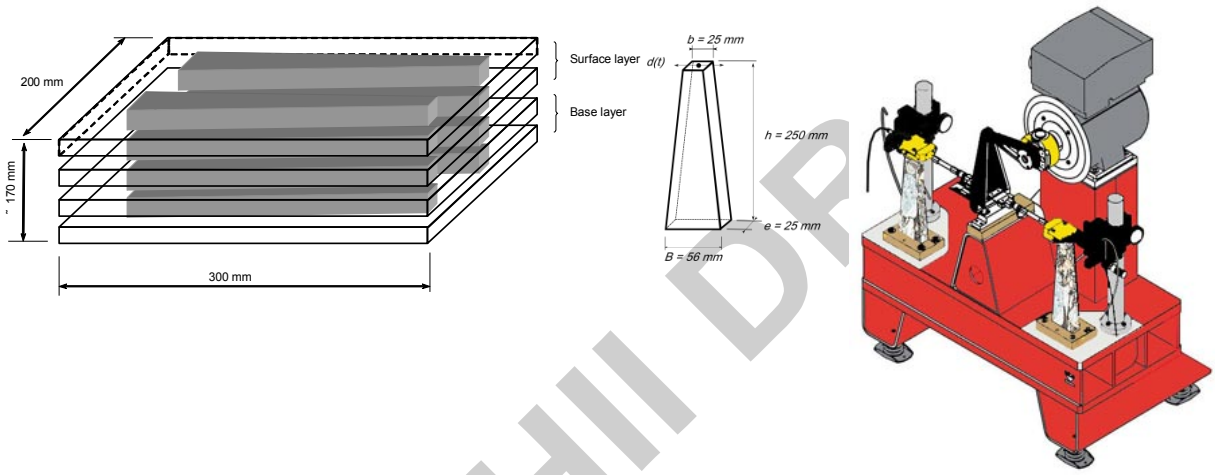

Fig. 2.23 Fatigue bending test on trapezoidal cantilever beam NF EN 12697-24 and M2F laboratory device (http://www.lcpc.fr/english/products/catalogue-of-mlpc-r-equipment/fiche-268/article/m2f-1111)

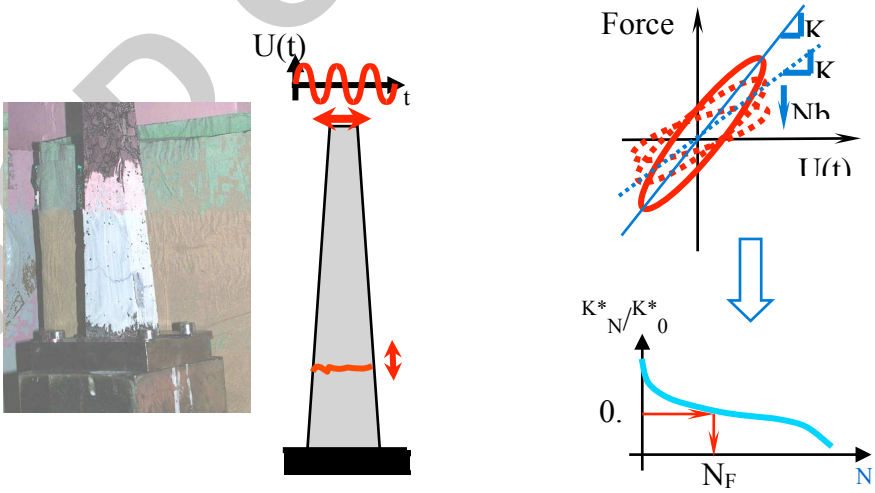

Fig. 2.24 Experimental setup [29]

Brief Test Description

The fatigue resistance of the materials is evaluated in bending mode on trapezoidal cantilever beams according the standard [35] on the M2F device (Fig. 2.23). Results of this test are usually used for pavement thickness designing [30].

The trapezoidal specimen is clamped on its large base and loaded at the top small base. A constant amplitude displacement is applied. Tests are more often performed at 10°C and at a frequency of 25 Hz. A variant of the test consist in applying a sinusoidal force at constant amplitude. A minimum of three loading levels sets need to be done. Each of them corresponds to a different loading level expressed by the maximal strain value in the specimen at the beginning of the test. To access to a mean value for each tests 6 specimen are tested at each loading level. For each test the force (and displacement) at the loaded boundary is measured as a function of the loading cycles.

The classical test analysis is based on a fatigue life criterion (Fig. 2.24). Classically, the specimen is supposed broken (N_f: number of cycles) when its stiffness reaches 50% of its initial value. A Wohler diagram is plotted presenting the fatigue life versus the loading levels (ε_a: maximal strain value around the specimen). Then, a linear regression is made in log-log coordinates leading to the relation between fatigue life and strain (Eq. (2.10).

For the French pavement design method, the strain level leading to specimen failure for one million cycles, ε_6 is used to calculate the admissible strain in each asphalt layers

$$N_f = 10^6 \left(\frac{\varepsilon_a}{\varepsilon_6} \right)^p \tag{2.10}$$

where p is the fatigue line slope in the log-log diagram [30].

To study the effects of the size of the specimen on fatigue process, three size of homothetic specimen can be tested [36]. Then a fatigue damage model [37] can be used to assess intrinsic fatigue cracking parameters.

2.3.2.4 Test results

Fatigue tests were undertaken in controlled strain mode. Testing conditions were as follows: temperature 20°C degrees; frequency 15 and 25 Hz; sinusoidal loading; strain levels between 120 and 190με. [38-39]. For each test stiffness modulus, phase angle and dissipated energy were calculated. The material chosen for the fatigue test is 10 mm Dense Bitumen Macadam (DBM) and 100 Pen Binder.

Fig. 2.25 shows the typical trend of the stiffness modulus. It is calculated considering the recorded stress divided by the applied strain. As it can be possible to see, a three stage evolution process is recorded during a fatigue test. After a rapid reduction of stiffness (phase I), due to the internal heating phenomenon, the stiffness decrease seems more regular (phase II). Fracture occurs in the final stage (phase III) and it is characterised by an acceleration of stiffness drop [40-43]. Fig. 2.26 shows the dissipated energy versus number of cycles.

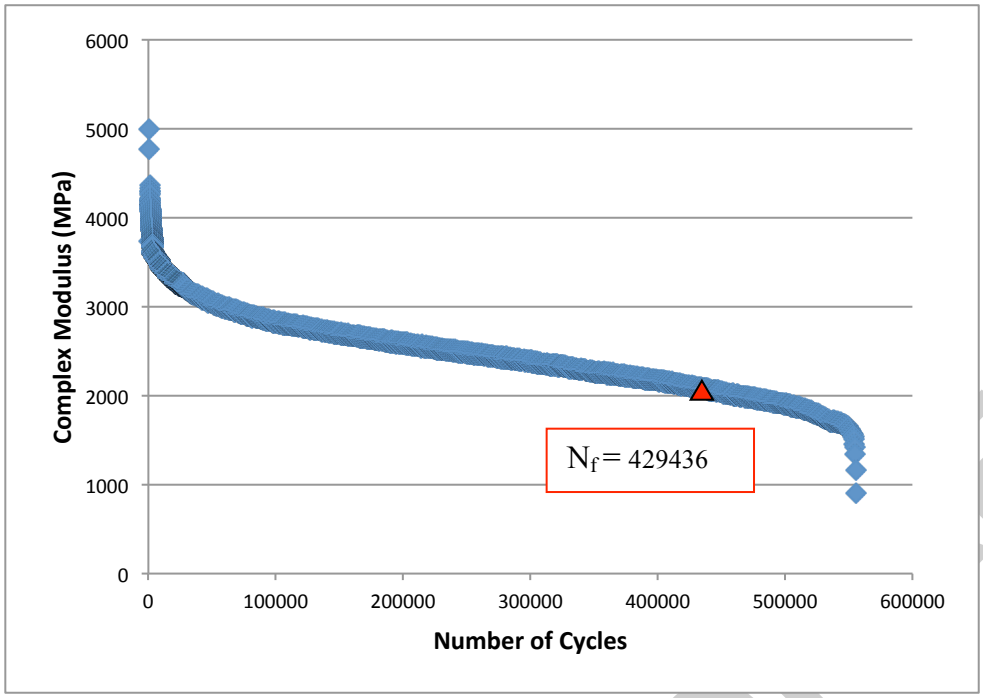

Fig. 2.25 Stiffness evolution during a fatigue test (160με)

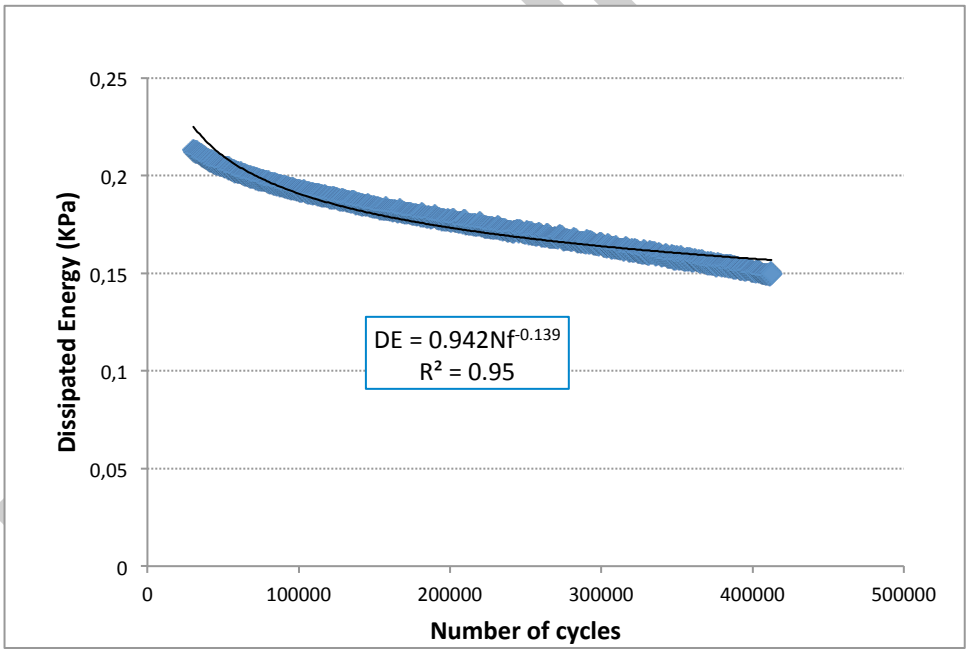

Fig. 2.26 Dissipated energy versus number of cycles during a fatigue test (160με) fitted with power law (Ax^k).

2.3.3 Skrinkage-Bending test from LRPC of Autun

2.3.3.1 Specimen Geometry and Equipement

Among all different lab tests used to get the behaviour of asphalt concrete beam with one or two layer (s) and an initial crack notch, the one coming from the regional laboratory of Autun (France) offers the possibility to simulate in laboratory, with thermal control possibilities crack propagations due to different shrinkage and cyclic bending load conditions. Readers may find more details about this test in Vecoven et al. [44] and Dumas et al. [45] (Fig. 2.27). By mean of a notch, this equipement has been used for testing the crack propagation in an asphalt material coming from the previous Rilem TC-CAP (Fig. 2.27).

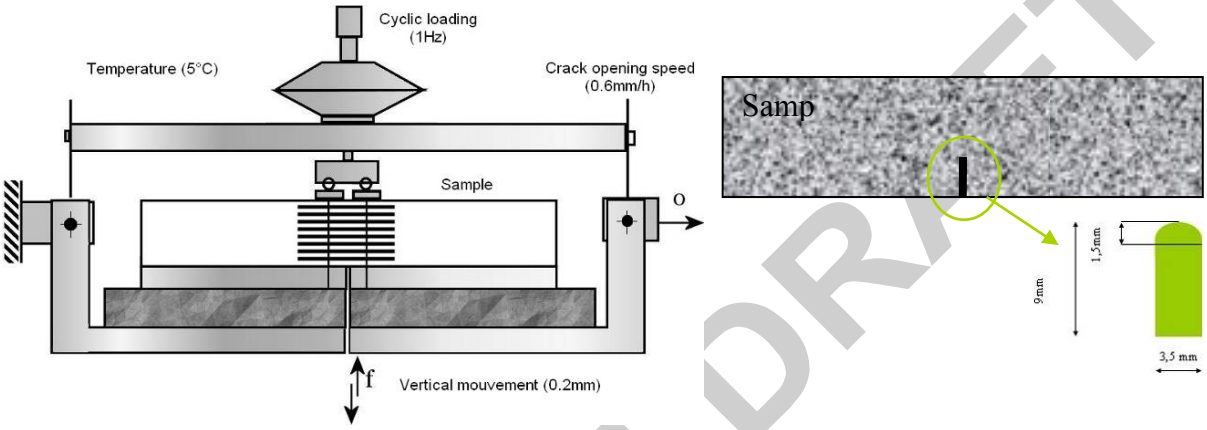

Fig. 2.27 Equipment [44] and the "special mono-layer" specimen geometry tested for the Rilem TC-CAP

2.3.3.2 Brief Test Description

This test simulates at once the pavement thermal contraction and the heavy traffic solicitations at a constant temperature (+5°C) in the following way (Fig. 2.27):

- The thermal shrinkage of precrack semi-rigid pavement is simulated by the opening of the movable plate (average speed 0.6 mm/h)
- The action of a track axle is simulated by a cyclic loading at a frequency of 1 Hz monitored by the deflexion set to 0.2mm."

During the test the measure consists in following the crack (initiation, propagation in the first centimetres and breaking time) by mean of special cracks sensors, strain sensors, force and displacement sensors (Fig. 2.28).

Although the link between these lab experimental results and those obtain with some accelerating pavement testing has to be done with lots of care (Pérez et al., 2007; 2008), this device is still used. It serves in France as a reference to test anti-crack systems for the knowledge of long term behaviour of 40% of French roads made of composite pavement (see SETRA Note N°57 for the typical French procedure used for testing anti-crack systems).

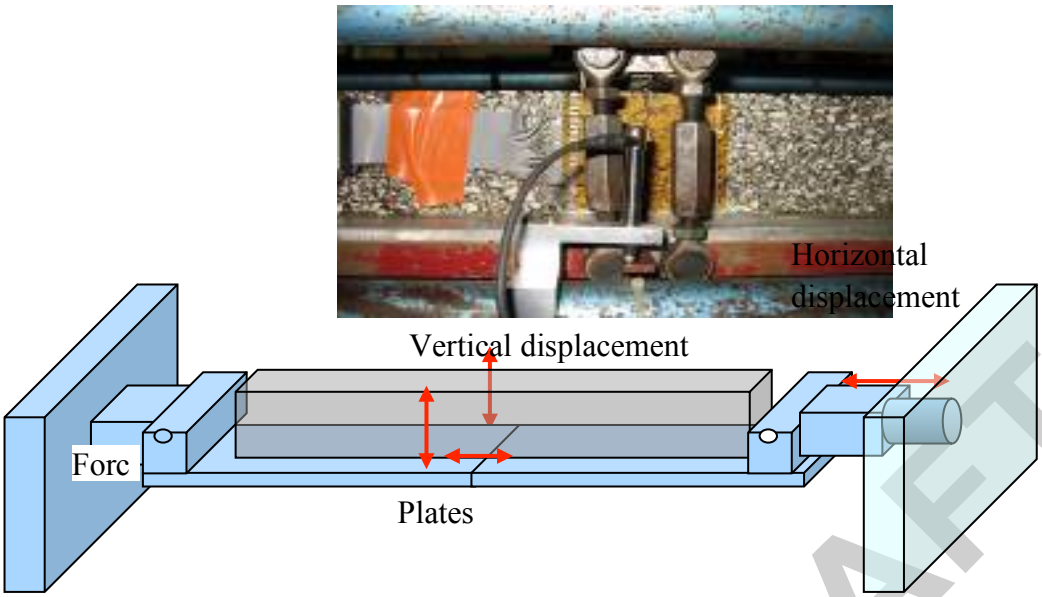

Fig. 2.28 Experimental Setup

2.4 CONSTITUTIVE MODELS FOR CRACK INITIATION AND PROPAGATION

The cracking phenomenon in asphalt concrete is quite complex and requires employment of fundamental fracture mechanics principles that are coupled with time and temperature dependent constitutive models to accurately represent the initiation and propagation of cracks. Due to the level of complexitiy involved with modelling of asphalt concrete as a heterogenous composite it is common for most modelling approaches to homogenize the asphalt mixture as an isotropic viscoeasltic composite. This assumption holds true at lower temperatures, as temperature increases the presence of viscoplasticity becomes more prevelant and should be incorporated in the model formulations.

This section of the chapter is divided into three sub-sections. The first subsection presents an energy based approach to model crack growth initiation in viscelastic materials. The formulation is based on approach proposed by Dubois et al. [46]. This is followed by cohesive zone approach, which is also an energy based formulation for representation of fracture quasi-brittle materials. Finally, a model proposed by University of Florida is presented that separates the elastic strain energy from the total strain energy to characterize fracture process in asphalt mixtures.

2.4.1 Crack Growth Initiation Model for Viscoelastic Materials

2.4.1.1 Model Introduction

For purposes of modeling, the bituminous concrete can be assumed as an isotropic viscoelastic material. It can be hypothesized that the crack growth process is generally concentrated within the bitumen or mastic phase of the bituminous concrete with crack bifurcations driven by the aggregates and their thin film interfaces. The study of the crack initiation and its propagation requires integration of time dependent behaviour associated with an energy based approach near the crack tip, thus making energy release rate concept a feasible approach. The crack growth initiation model described here focuses on a numerical approach that couples an incremental formulation for viscoelastic response and energy release rate evolution versus time allowing the simulation of the crack initiation and its propagation.

The model is implemented in a finite element softwareusing spectrum decomposition scheme for Prony series in the complex domain. This algorithm allows the definition of the strain and stress responses by integrating the Boltzmann's formulation in the time domain. In this context, time frequency transposition is proposed using a spectrum decomposition technique. The fracture analysis for representation of crack initiation and growth in bitumen follows Dubois's approach [46]. In this approach the energy release rate is computed by performing a separation technique providing the exact the viscous dissipation isolation. Based on the non-dependence past integrals, the Gq technique is adapted for creep crack growth [47].

2.4.1.2 Model Formulation

The viscoelastic behaviour is generally written in terms of a Boltzmann's integral which defined the time relationship between the stress tensor $\underline{\underline{\sigma}}(t)$ and the strain tensor $\underline{\underline{\varepsilon}}(t)$. Assuming a linear response, the hereditary behaviour is traduced by the following form:

$$\underline{\underline{\varepsilon}}(t) = \int_0^t \mathbf{J}(t-\tau) \cdot \frac{\partial \underline{\underline{\sigma}}}{\partial \tau} d\tau \tag{2.11}$$

In which $\mathbf{J}$ is the four-order creep tensor. The bitumen can be characterized as an isotropic material. It is generally admitted that the Poisson's coefficient ν can be assumed as a constant property. With this consideration, Eq. (2.11) can be rewritten as follows:

$$\underline{\underline{\varepsilon}}(t) = \mathbf{A} \cdot \int_0^t C(t-\tau) \cdot \frac{\partial \underline{\underline{\sigma}}}{\partial \tau} d\tau \tag{2.12}$$

$C(t)$ designates a compliance function which can be defined as the inverse function of the tangent rigidity modulus noted $E(t)$. $\mathbf{A}$ is a constant tensor composed with the Poisson's ratio. The linear viscoelastic behavior can be expressed with a discrete spectrum representation which allows us the storage overcoming of the complete past history of stresses and strains. This method is based on a time discretization of the compliance function according to the following Prony's series:

$$C(t) = C_o + \sum_{m=1}^{M} C_m \cdot \left[1 - \exp(-t/\tau_m)\right] \tag{2.13}$$

C_o and C_m are positive compliance constants. τ_m are relaxation times. Then, the governing equations can be obtained using the finite difference integration and a step-by-step algorithm. Incremental constitutive equations, using a linear approximation of stresses in each time step $\Delta t_n = t_n - t_{n-1}$, are given by:

$$\underline{\underline{\Delta\varepsilon_n}} = \mathbf{A} \cdot M_n \cdot \underline{\underline{\Delta\sigma_n}} + \underline{\underline{\tilde{\varepsilon}}}(t_{n-1}) \tag{2.14}$$

$\underline{\underline{\Delta\varepsilon_n}}$ and $\underline{\underline{\Delta\sigma_n}}$ are the increments of $\underline{\underline{\varepsilon}}(t)$ and $\underline{\underline{\sigma}}(t)$, respectively, during the time increment Δt_n. $\underline{\underline{\tilde{\varepsilon}}}(t_{n-1})$ is a pseudo-strain tensor at time t_{n-1} illustrating the influence of the past history of stress. M_n designates the viscoelastic compliance function defined, for the specific time step Δt_n, by:

$$M_n = C_o + \sum_{m=1}^{M} C_m \cdot \left[1 - \frac{\tau_m \cdot \left(1 - \exp\left(-\Delta t_n / \tau_m\right)\right)}{\Delta t_n}\right] \tag{2.15}$$

The finite element resolution of the incremental formulation in Eq. (2.14) is performed by employ the Ghazlan's method (C. Chazal, 2001) derived from the virtual displacement principle. According to the nodal displacement vector notation $\{\Delta u\}_n$, the balance equation, in the discredited domain W, can be written as:

$$K_T \cdot \{\Delta u\}_n = \{\Delta F_{ext}\}_n + \{\widetilde{F}\}(t_{n-1}) \tag{2.16}$$

K_T is an equivalent stiffness matrix. $\{\Delta F_{ext}\}_n$ denotes the increment of nodal force vector. $\{\widetilde{F}\}(t_{n-1})$ is the supplementary viscous loading vector representing the complete mechanical history. It overcomes the difficulty to perform, for each time step, the Boltzmann's integral without storage of stress and strain histories. It is given by:

$$\{\widetilde{F}\}(t_{n-1}) = \int_{\Omega} B^T \cdot M_n \cdot \mathbf{A} \cdot \{\widetilde{\varepsilon}\}_{n-1} d\Omega \tag{2.17}$$

Where $\{\widetilde{\varepsilon}\}_{n-1}$ is the strain vector derived from the strain history tensor $\underline{\underline{\widetilde{\varepsilon}}}(t_{n-1})$.

The crack growth process in a viscoelastic media induces different sources of energy dissipation achieved through viscous disipation, the crack surface separation and the kinetic energy caused by the crack tip advance and dynamic effects. According to Dubois's formulations [47], the crack growth initiation can be driven by considering the viscoelastic energy release rate definition calculated by a classical path independent integral. In this context, this work uses the Gθ integral defined, for axisymmetric description, as follow:

$$G\theta = \frac{1}{P} \cdot \int_C \left(-W_\varepsilon \cdot \theta_{k,k} + \sigma_{ij} \cdot u_{i,k} \cdot \theta_{k,j}\right) dC \tag{2.18}$$

C is path surrounding the crack tip. $\vec{\theta}$ is a derivable vector field defined by it boundary conditions on the integration path according to a crack growth in the x direction or the r direction for axisymmetric cases, respectively. P is a geometric parameter allowing to adapt the formalism for axisymmetric configurations (circular crack tip length). For viscoelastic behaviours, Staverman (A. Staverman, 1952) has demonstrated the W_ε form by integrating creep properties. It form is given by:

$$W_\varepsilon = \frac{1}{2} \cdot \int_0^t \int_0^t A_{ijkl} \cdot \left[2 \cdot C(t-\xi) - C(2 \cdot t - \xi - \beta)\right] \cdot \frac{\partial \sigma_{ij}}{\partial \xi} \cdot \frac{\partial \sigma_{kl}}{\partial \beta} d\xi d\beta \tag{2.19}$$

A_{ijkl}, σ_{ij} and σ_{kl} are components of the tensor $\mathbf{A}$ and the stress tensor, respectively, see Eq. (2.12).

2.4.1.3 Example Aplication of the Crack Growth Initiation Model: Numerical Modelling of the Bitumen Fracture

The researchers at IFSTTAR have developed a test in order to evaluate the bitumen contribution in the fracture phenomena in bituminous concrete [48-49]. This test allows to simulate the crack growth process in bitumen around aggregates. The specimen is composed by a thin film fixed between two steel convex protuberances onto which the testing machine

imposes a displacement with different loading rates and temperature (c.f. Fig. 2.29). The specimen geometry allows assuming an axisymmetric approach. The crack initiation is localized in the specimen center. The vertical symmetry enables the assumption of fracture in mode –I with a concentric crack front along the privileged crack line. The discretized geometry through the finite element mesh is also shown in Fig. 2.29. The contact between steel convex protuberances and bitumen is modeled with a line interface on to which a vertical displacement boundary condition is imposed. It can be noted that the film thickness is a parameter called e. The crack propagation line is a symmetric line in which vertical displacements are blocked. The crack tip advance is operated by freeing vertical boundary conditions with respect to the actual crack length [50].

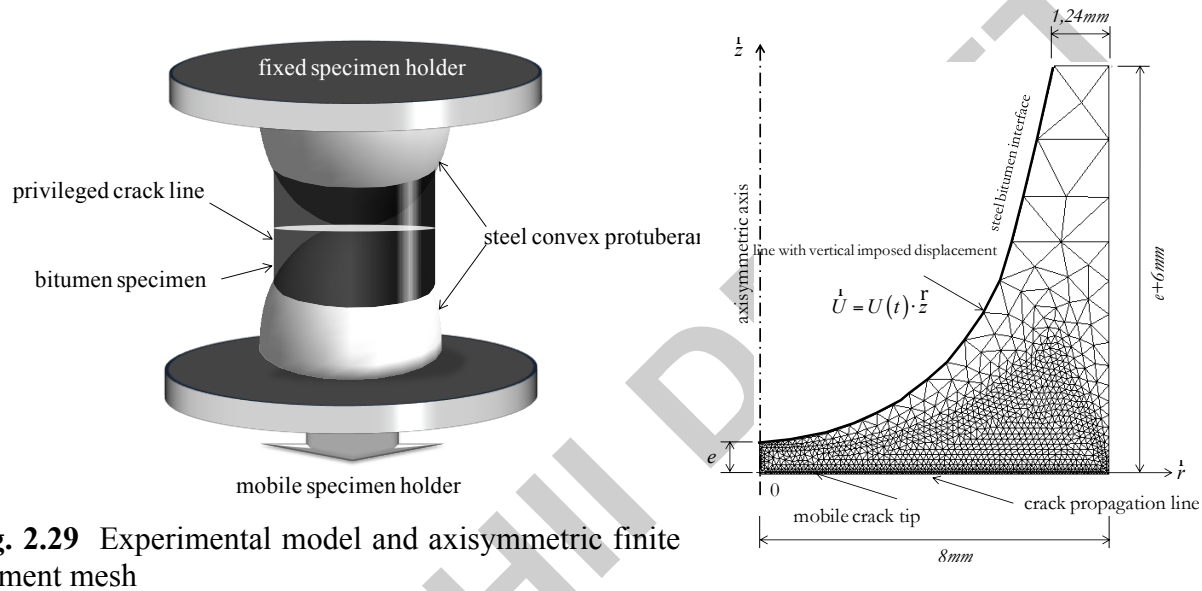

Fig. 2.29 Experimental model and axisymmetric finite element mesh

For the materials used in this example, the viscoelastic properties, in the frequency domain, have been measured on a pure bitumen of PEN50/70 grade by employing a viscoanalyser Metralib at different temperatures. The Prony series parameters for linear viscoelastic characterization are determined at a reference temperature of 0°C. The decomposition of Prony series is based on a discrete spectrum decomposition allowing the limited number of parameters. The compliance components, C_m and relaxation times t_m are given in Table 2.4.

Table 2.4 Prony series parameters at reference temperature, T=0°C

Compliances (Mpa^{-1})		Relaxation times (s)	
C_o	$1,02 \times 10^{-3}$	-	-
C_1	$6,37 \times 10^{-4}$	t_1	$2,39 \times 10^{-3}$
C_2	$6,72 \times 10^{-4}$	t_2	$1,53 \times 10^{-2}$
C_3	$4,16 \times 10^{-3}$	t_3	$2,07 \times 10^{-1}$

The tenacity test results showed the intrinsic separation work rate G_s to be *4J/m²* and the tension toughness f_t of *2MPa* at the reference temperature of *0°C*.

It is necessary to adjust the Poisson's ratio throughout the tensor A (Eq. (2.12)) in order to make adjustments for the assumed initial crack length. In this context, it considers that, for very small crack lengths, the reaction force can be assimilated as a function of Poisson's ratio, n. A first test is analyzed with a film thickness (e) of *320μm*, a displacement speed of *11m/s*. The crack initiation is given for a critical displacement value of *6.7μm* and an equivalent reaction force of *150N*. The correspondence between displacement timeand force leads to resolving the Poisson's ratio value at *0.35*. This first simulation deals with the crack growth initiation by imposing different speeds for displacements. Results are given in terms of displacement-force curves for 11m/s (reference result), 5.5m/s, 2.0m/s and 1.1m/s, see Fig. 2.30(a). These results show that the relaxation effects are evident during the crack growth initiation phase. At high speeds, the crack growth initiation is driven by the elastic response inducing high force value and lower displacements. In the other hand, at low speeds the long term properties with a softening behaviour is apparent through lower induced force levels.

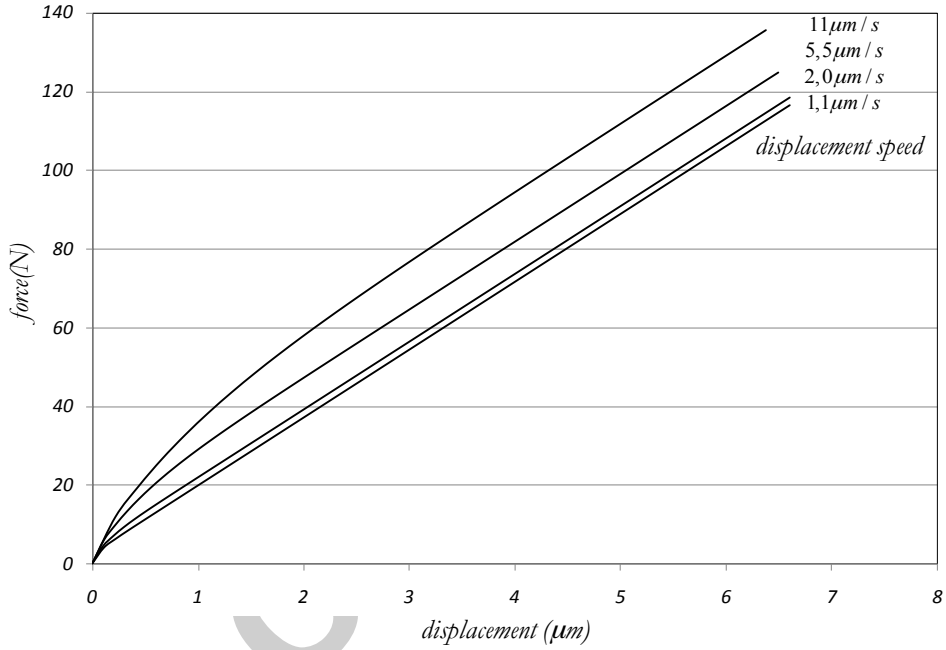

(a)

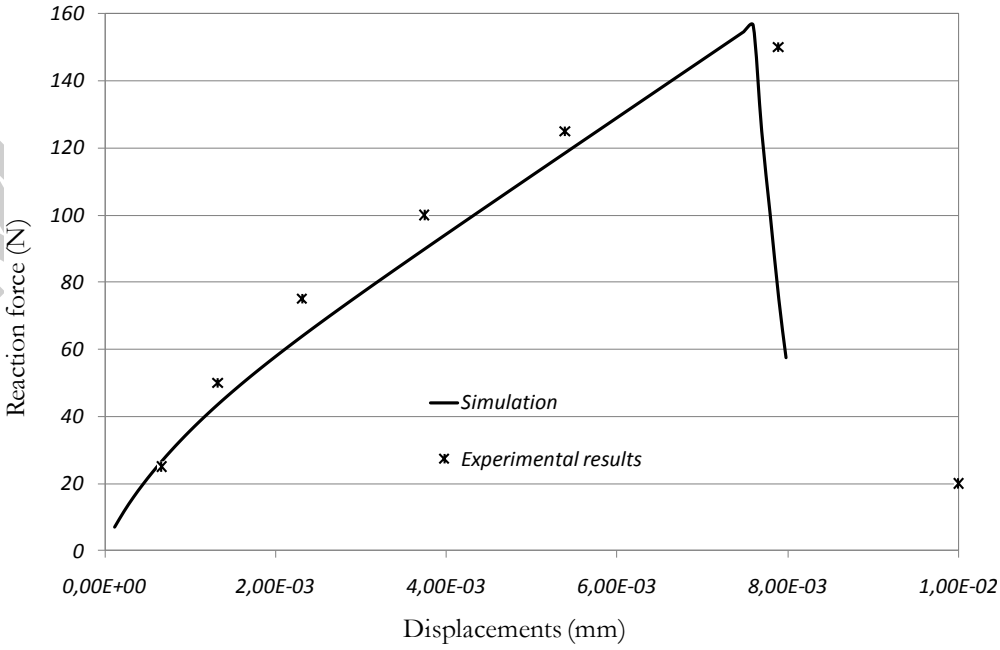

(b)

Fig. 1.30 Force-displacement, **(a)** experimental results; (b) experimental and simulation results

The Fig. 2.30(b) shows comparisons between the experimental and finite element simulation results. A good prediction for the crack growth initiation phase can be observed. The differences can be partly due to difficulties in defining the time discretization of creep function. However, the crack growth instability traduces more differences with experimental results. In fact, the time domain resolution and the crack growth algorithm can trace the progressive crack lip decohesion but does not take into account the damage state around the crack tip characterized by the process zone. The cohesive zone approach discussed next focusses on capturing the damage state within the process zone.

2.4.2 Cohesive Zone Fracture Model

2.4.2.1 Model Introduction

The geometric and non-linear material response in the vicinity of the crack tip and the importance of accurate simulation of crack initiation and propagation make a standard "strength of materials" type analysis insufficient for the realistic simulation of cracking in asphalt concrete. Wagoner et al. [1][5], Li et al. [51] and other researchers involved in fracture testing of asphalt concrete at low and intermediate temperatures have reported the presence of a fracture process zone ahead of an advancing crack tip. The cohesive zone fracture modelling approach allows for better representation of the traction-separation behaviour of quasi-brittle materials by linking intrinsic material properties such as fracture energy and cohesive strength with the length scale associated with the size of the aforementioned fracture process zone (FPZ). For simulation of crack initiation and propagation, a cohesive zone model is recommended for its accuracy in representing the FPZ and efficiency in numerical simulation framework, such as finite element analysis. Several researchers including Song et al. [52] have demonstrated the capabilities of the cohesive zone model (CZM) for accurate simulation of cracking in asphalt concrete materials. The bi-linear CZM described by Song et al. [52] has been applied for simulation of thermal and reflective cracking in asphalt pavements and overlays, for example by Dave et al. [53].

2.4.2.2 Model Formulation

Here a temperature dependent bi-linear CZM is presented. This approach allows the fracture energy of asphalt concretes to be simulated as function of temperature. At present, the tensile strength of the material is modelled to be independent of temperature. This simplification was made on the basis of the laboratory test results, which indicated very limited dependence of strength with temperature within the simulation thermal boundaries, i.e. for temperatures below 10°C. Fig. 2.31 illustrates the temperature dependent bi-linear CZM for an asphalt mixture from in mode-I (pure opening) fracture. The CZM describes the relationship between traction and the displacement jump along the potential crack path. Notice that the intrinsic model form of the present CZM requires use of an initial, linearly elastic response regime with very high stiffness selected based upon the parametric study of Song et al. [52], as described below. The location 'A' in the figure illustrates the peak traction corresponding to the material strength as the threshold for material damage. The displacement at this location can be written as δ_A. The region between points 'A' and 'B' represents the progression of damage in the material and could represent the coalescence of the micro-cracks within the fracture process zone. The region past of location 'B' represents a fully formed

macro-crack, the cohesive displacement at point 'B' is commonly referred as the critical displacement and could be given by δ_B. At any given temperature, the area under the traction-displacement curve represents the fracture energy of the material. For the given example the traction-displacement surface illustrates its evolution with temperature. The traction-displacement relationship for the temperature dependent bi-linear CZM in mode-I could be written as,

(2.20)

Where, σ_c represents the material cohesive strength and T is the temperature. The displacements at any given instance is the element is δ_n and the corresponding traction is t_n. The displacement at peak traction and at the complete separation are δ_A and δ_B respectively. The fracture energy of material, G_f, links the strength, σ_c, with the displacement jump at complete separation, δ_B as,

$$G_f(T) = \frac{1}{2}\sigma_c \delta_B(T) \tag{2.21}$$

The displacement jump at peak traction, δ_A is chosen to minimize undesired or artificial compliance in the cohesive zone interface elements prior to material softening. It is typically recommended for this to be less than or equal to 1% of δ_B. This recommendation is made in order to minimize the artificial compliance induced due to model in the simulation results.

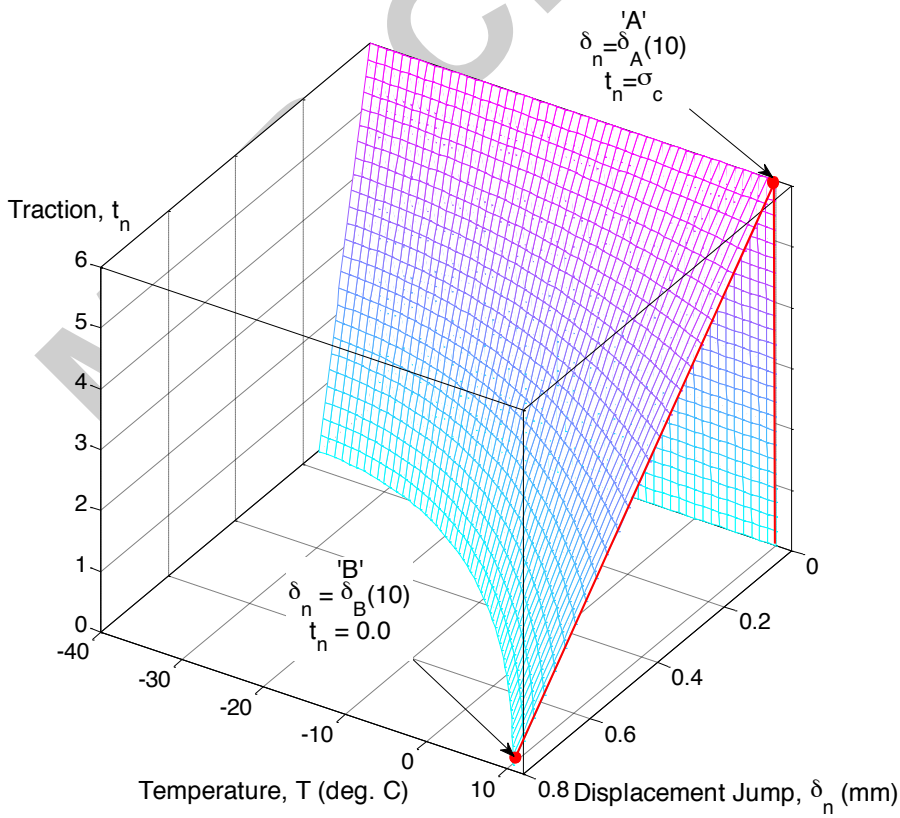

Fig. 2.31 Temperature dependent bi-linear Cohesive Zone Model for MnROAD Section 34 mixture (Cohesive Strength = 5.94 MPa)

2.4.2.3 Model Verification, Calibration and Validation

Verification, calibration, and validation steps provide a realistic evaluation of the accuracy and robustness of a numerical model. As part of the RILEM CAP TG-03 work, the researchers from University of Illinois completed these steps to evaluate the capabilities of cohesive zone models. The verification step in this case employed the double cantilever beam (DCB) geometry due to the presence of a known analytical solution. As shown in Fig. 2.32(a), the numerical results matched well with the closed-form solution. Next, the calibration step included the use of the DC(T) geometry with experimentally evaluated strength and fracture energy parameters embedded in the CZM. The numerical solution in the calibration stage was adjusted by a constant factor of 0.84 to produce a global load-CMOD response similar to the experimental results. In general, calibration factors are employed in considering global fracture energy because CZM models tend to over-predict the fracture resistance of the material at the local level. Finally, validation was completed using the semi-circular bend (SCB) geometry. In this study, the cohesive zone model performed quite well as shown in Fig. 2.32(b). Therefore, the verification, calibration, and validation steps displayed the abilities of the CZM approach in asphalt materials.

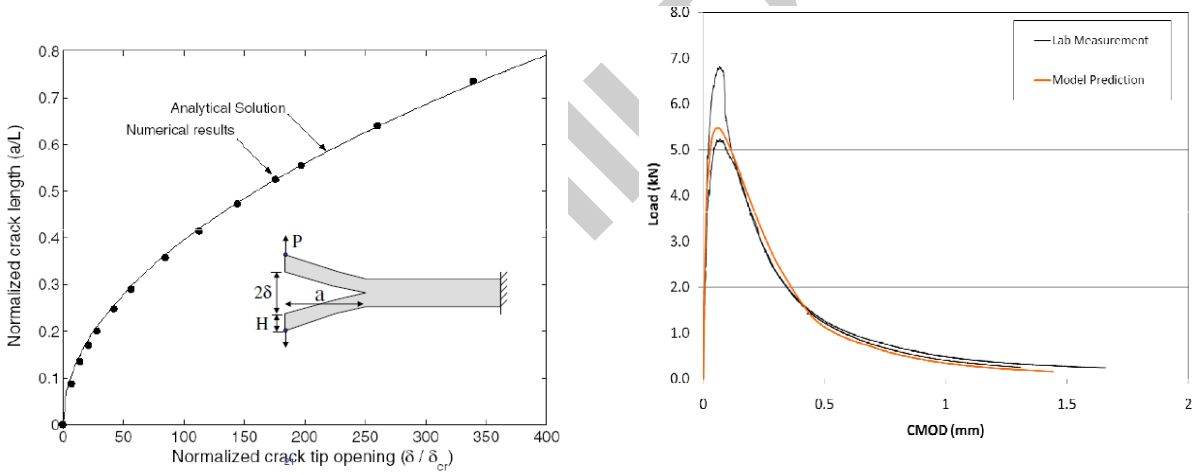

Fig. 2.32 **(a)** Verification using DCB **(b)** Validation using SCB

2.4.3 Hot Mix Asphalt Fracture Mechanics Model

2.4.3.1 Model Introduction

Laboratory and field studies at the University of Florida have led to the development of a viscoelastic fracture mechanics-based cracking model, termed HMA-Fracture mechanics (HMA-FM) model. The model is focused on describing both initiation and propagation of cracks in asphalt mixtures for any combination of loading and temperature conditions. Previous research work has shown that conventional fracture mechanics approach [54-55] may provide a rational way to consider the effects of stress redistribution induced by flaws or micro-cracks in a material. The HMA-FM model assumes that crack growth in asphalt pavements occurs in discontinuous, step-wise manner on basis of the anecdotal evidence from field observations as reported in previous research [56-57] .

Viscoelasticity and continuum damage approach [57-58] analyzes micro-cracking behavior of asphalt mixtures under realistic loading conditions and healing effect. However, continuum

damage mechanics is not applicable after crack initiates (the system is no longer a continuum) and, thus, a continuous crack growth law is assumed for crack propagation in the HMA-FM approach.

The HMA-FM model provides a viscoelastic fracture mechanics-based cracking model able to predict both crack initiation and step-wise propagation, under generalized loading and healing conditions, based on an energy-based threshold concept.

2.4.3.2 Model Formulation

The HMA-FM model utilizes a concept of threshold or limit that is based on the observation that micro-damage in asphalt mixtures (i.e., damage that may potentially lead to crack initiation or crack propagation) appears to be fully healable, whereas macro-damage (i.e., damage associated with crack initiation or propagation) does not appear to be healable [59-62]. This indicates that a damage threshold exists below which damage is fully healable. Once the threshold is exceeded, the developed macro-damage is no longer healable. As with other two approaches discussed easlier in the section, the threshold limit is deifned in terms of energy. The energy threshold defines the development of macro-cracks (macro-damage), at any time during either crack initiation or propagation, at any point in the mixture. If loading and healing conditions are such that the induced energy does not exceed the mixture threshold, then the mixture may never crack, regardless of the number of load repetitions applied.

As discussed by Zhang [59] and Roque et al. [61], fracture (crack initiation or crack propagation) can develop in asphalt mixtures in two distinct ways, defined by two distinct thresholds or failure limits. It has been determined that the dissipated creep strain energy (DCSE) density and the fracture energy (FE) density of asphalt mixtures suitably define the lower and the upper failure limits, respectively.

In the HMA-FM approach the fracture energy density and dissipated creep strain energy density is determined from the stress-strain response of a tensile strength test conducted on asphalt mixture, as shown in Fig. 2.33. The fracture energy density limit (FE_f) is determined as the area under the stress-strain curve, while the dissipated creep strain energy density limit ($DCSE_f$) is the fracture energy minus the elastic energy (EE) at the time of fracture. Resilient modulus (M_R) and tensile strength (S_t) are used to define EE. These two energy failure limits ($DCSE_f$ and FE_f) have been identified as fundamental material properties of asphalt mixtures, independent of mode of loading, rate of loading and specimen geometry [63].

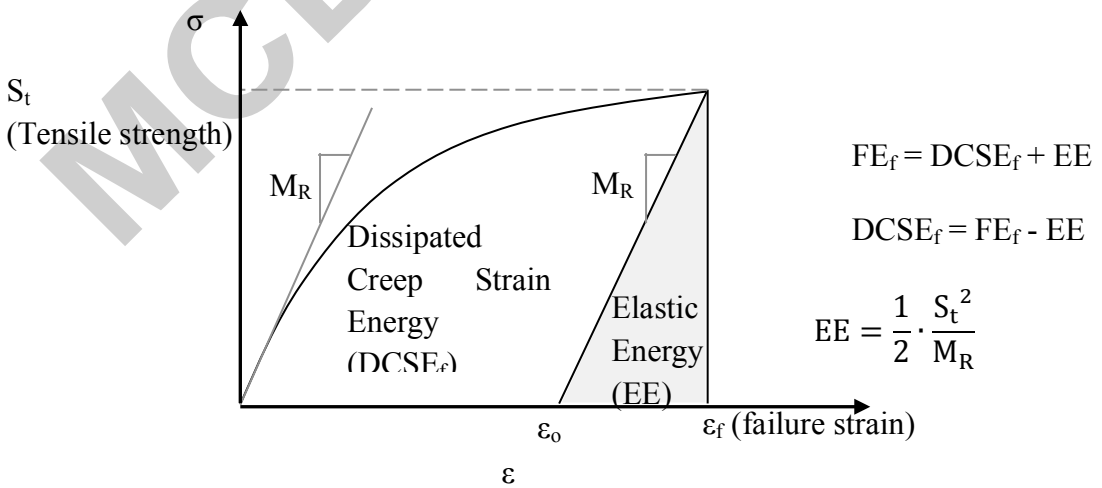

Fig. 2.33 Determination of failure limits: FE and DCSE [59-61]

The lower threshold ($DCSE_f$) is selected as the failure criterion under repeated loading condition (Fig. 2.34(a)). When repeated stresses significantly below the tensile strength occur, cracking will eventually take place if the rate of damage accumulation exceeds the rate of healing during the loading period. In contrast, the upper energy threshold (FE_f) corresponds to the failure criterion under critical loading condition (Fig. 2.34(b)). In this case, fracture would occur if any single load applied during the loading cycle exceeds the threshold required to fracture the mixture.

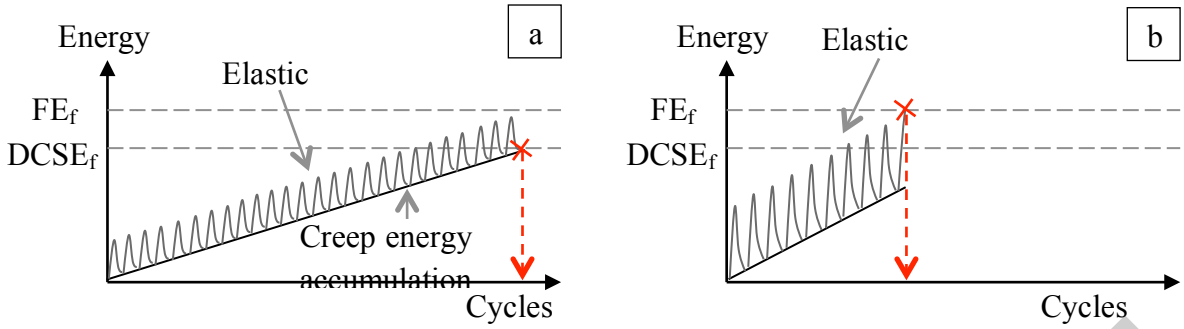

Fig. 2.34 Potential failure conditions under continuous loading. **(a)** Repeated loading. **(b)** Critical load

One unique feature of the HMA-FM model is the consideration of both failure limit and rate of damage to predict fracture. The rate of damage of an asphalt mixture under repeated loading conditions is defined as the dissipated creep strain energy density accumulated per load cycle (DCSE/cycle). Therefore, there is an inherent assumption that damage can be quantified in terms of the viscous response (creep) of the asphalt mixture.
For a haversine load consisting of a 0.1s loading period followed by a 0.9s rest period, DCSE/cycle is defined as the integral of the stress σ(t) multiplied by the creep strain rate $\dot{\varepsilon}_{cr}(t)$:
where σ_{ave} represents the average stress in the zone of interest, and $\dot{\varepsilon}_{cr,max}$ is the maximum creep strain rate.

$$\frac{DCSE}{cycle} = \int_0^{0.1} \sigma(t) \cdot \dot{\varepsilon}_{cr}(t) \cdot dt = \int_0^{0.1} \underbrace{\sigma_{ave} \cdot \sin(10\pi t)}_{\sigma(t)} \cdot \underbrace{\dot{\varepsilon}_{cr,max} \cdot \sin(10\pi t)}_{\dot{\varepsilon}_{cr}(t)} \cdot dt \tag{2.22}$$

The maximum creep strain rate can be estimated from a creep test, based on the relationship between creep strain $\varepsilon_{cr}(t)$ and creep compliance D(t):

$$\varepsilon_{cr}(t) = \sigma_{ave} \cdot D(t) \tag{2.23}$$

One model used for creep compliance representation is power law function:

$$D(t) = D_0 + D_1 \cdot (t_{cr})^m \tag{2.24}$$

where D_0, D_1, and m are fitting parameters, and t_{cr} is the duration of the creep test. Typically, a 1000-second creep test has been considered to be enough to capture the viscous response exclusively for intermediate temperatures associated with fatigue (0-25 ºC). Then, the maximum creep strain rate is determined as:

$$\dot{\varepsilon}_{cr,max} = \sigma_{ave} \cdot \frac{dD(t)}{dt} = \sigma_{ave} \cdot m \cdot D_1 \cdot (t_{cr})^{m-1} \tag{2.25}$$

Substituting Eq. (2.25) into Eq. (2.22), the rate of damage (DCSE/cycle) is obtained:

$$CSE/cycle = \frac{1}{20} \cdot (\sigma_{ave})^2 \cdot m \cdot D_1 \cdot (t_{cr})^{m-1} \tag{2.26}$$

It should be pointed out that healing, which can be described in terms of recovered DCSE per cycle [64], must be determined and used to adjust the rate of damage.

The parameters utilized in this approach can be used not only to predict damage and crack growth in mixtures subjected to generalized loading conditions, but they may also be used in

mixture design and optimization. For example, the fracture tolerance of mixture improves as the $DCSE_f$ limit increases. Similarly, a lower creep rate, which is a function of D_1 and m-value, will result in a lower rate of damage accumulation. However, lower rate of damage does not necessarily assure improved cracking performance, since failure limit and healing rate are also involved in cracking mechanism.

The HMA-FM model assumes a step-wise crack growth law, as shown in Fig. 2.35. When the DCSE accumulated in the zone with the highest average tensile stress equals the $DCSE_f$ limit of the mixture, a crack initiates. Then, crack propagates through the next zone every time that the DCSE accumulated in that zone equals the $DCSE_f$ limit of the mixture. Note that the model keeps track of the DCSE induced in all zones where crack growth may be of interest (at every step).

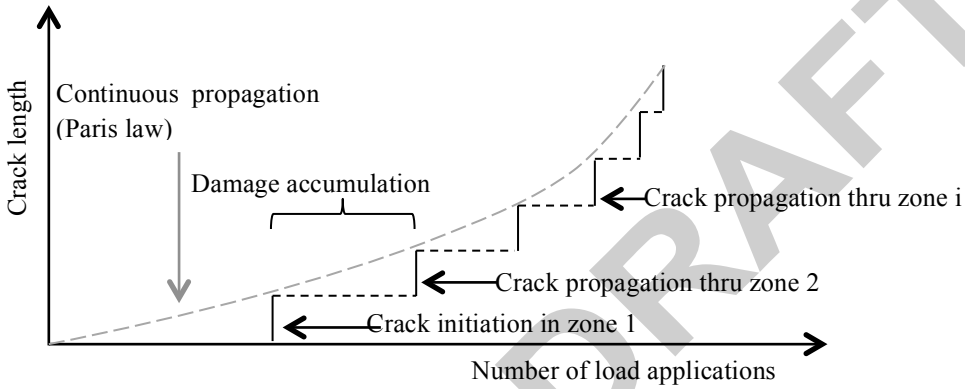

Fig. 2.35 Step-wise crack growth law [59-61]

The basic analysis framework of the model is as follows:

1. Divide potential crack path(s) into zones. Previous analysis showed that zone size had little effect on the predicted rate of crack propagation [65], so zones of fixed size are considered for the analysis. Typically, a zone size of 5 mm is used, which is assumed to capture the effect of stress concentration near the contact points between aggregates.
2. Calculate or estimate the stress distribution and compute the average tensile stress in each zone during condition 1, i.e. $(\sigma_{ave})_{i,1}$, where i represents the zone number.
3. Determine the rate of damage in each zone for condition 1, i.e. $(DCSE/cycle)_{i,1}$ according to Eq. (2.26) for the average tensile stress calculated in step 2, i.e. $(\sigma_{ave})_{i,1}$.
4. Determine the number of cycles for crack initiation in zone 1 ($N_{f,1}$):

$$N_{f,1}(initiation) = \frac{DCSE_f}{(DCSE/cycle)_{1,1}} \tag{2.27}$$

in which $DCSE_f$ is the failure limit of the asphalt mixture, and $(DCSE/cycle)_{1,1}$ is the rate of damage for zone 1 during condition 1.

5. Determine the new stress distribution as a result of crack growth. Once the crack initiates, the stress distribution ahead of the crack tip σ(r) can be estimated as:

$$\sigma(r) = \sigma_{FA}\frac{a+r}{\sqrt{r}\cdot\sqrt{2a+r}} \tag{2.28}$$

where r is the distance measured from the crack tip, a is half the crack length, and σ_{FA} represents the far away stress.

As shown in Fig. 2.36, tensile stresses in the material have an upper limit equal to the tensile strength of the asphalt mixture (S_t) and a lower limit equal to the far way stress (σ_{FA}).

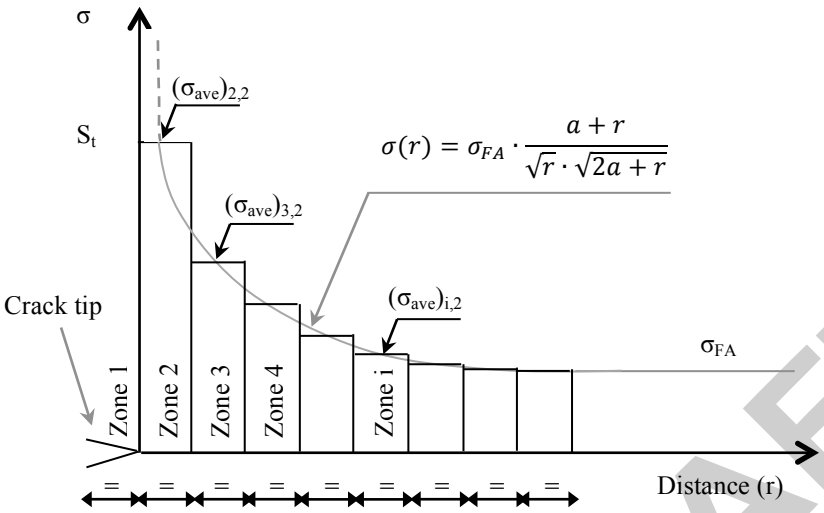

Fig. 2.36 Stress distribution ahead of the crack tip after crack initiation

6. Compute the average tensile stress in each zone during condition 2, i.e. $(\sigma_{ave})_{i,2}$.
7. Calculate the rate of damage in each zone for condition 2, i.e. $(DCSE/cycle)_{i,2}$ according to Eq. (2.26) for $(\sigma_{ave})_{i,2}$ obtained in step 6.
8. Determine the number of cycles for crack propagation through zone 2 ($N_{f,2}$):

$$N_{f,2}(propagation) = \frac{DCSE_f - \overbrace{\left(\frac{DCSE}{cycle}\right)_{2,1} \cdot N_{f,1}}^{Accumulated\ from\ previous\ condition}}{\left(\frac{DCSE}{cycle}\right)_{2,2}} \quad (2.29)$$

where $(DCSE/cycle)_{2,1}$ is the rate of damage for zone 2 during condition 1, $(DCSE/cycle)_{2,2}$ is the rate of damage for zone 2 during condition 2, and $N_{f,1}$ is the number of cycles to fail zone 1.

9. Repeat steps 5 through 8 to determine crack propagation through new zones. Note that the fracture energy density limit (FE_f) also has to be checked for every condition.

It should be pointed out that crack propagation predicted by the model (crack length versus number of load repetitions) agreed closely with crack growth measured in laboratory tests [59-61]. These results support that the HMA-FM model is rational and reliable to predict cracking performance of asphalt mixtures.

2.4.3.3 Use of Model for Evaluation of Cracking Performance

A detailed analysis and evaluation of 22 field test sections throughout the state of Florida resulted in the qualification, calibration and validation of the energy-based criteria for cracking evaluation in asphalt mixtures [66]. The work clearly indicated that there is no single mixture property or characteristic (volumetrics, viscosity of recovered binder, resilient modulus, tensile strength, creep compliance, etc.) that can reliably predict cracking performance of asphalt mixtures. A parameter termed energy ratio (ER), which was derived using the HMA-FM model, was determined to accurately distinguish between pavements that exhibited cracking and those that did not, except for mixtures with excessively low or unusually high dissipated creep strain energy thresholds.

Using data from the field sections and laboratory testing the paramerters such as ER and A can be calibrated to be linked to laboratory measured properties. The energy ratio (ER) is defined as the dissipated creep strain energy density limit ($DCSE_f$) of the mixture divided by the minimum dissipated creep strain energy required can be represented in terms of material properties as:

$$ER = \frac{DCSE_f}{DCSE_{min}} = \frac{DCSE_f}{\frac{m^{2.98} \cdot D_1}{A}} \tag{2.30}$$

where, m and D_1 are the creep compliance power law fitting parameters.

A is a parameter that depends on the tensile stress in the pavement section (σ_t) and the tensile strength of the mixture (S_t):

$$A = \frac{(6.36 - S_t)}{33.44 \cdot {\sigma_t}^{3.1}} + 2.46 \cdot 10^{-8} \tag{2.31}$$

The energy ratio accounts for the effects of pavement structural characteristics (σ_t) and material properties ($DCSE_f$, S_t, m, D_1) on cracking performance: the higher the value of the energy ratio, the better the expected cracking performance of the section. Therefore, ER can be used to integrate asphalt mixture properties in the pavement design process as well as to predict the performance of in-service pavement sections.

2.4.3.4 Summary of Models for Discrete Cracking In Asphalt Mixtures

This section discussed three models that are developed and implemented for modelling of cracks in asphalt mixtures. All three of the the approaches described herein have their advantages and disadvantages in terms of their capabilities and limitations. Each of these models have provided insight into the mechanisms of cracking in pavements. Table 2.5 provides a brief summary of the three approaches in terms of the basis (theory/approach) behind the models, required laboratory tests/material parameters, status of the model in terms of model qualification, verification, calibration and validation, and the status of application of the models to simulate cracking performance of pavements and improve understanding of cracking mechanisms for asphalt and composite pavements. The validation status is divided into two catagories, namely laboratory and field. Laboratory validation refers to use of model to predict a different test using calibration and material parameters from a different test. Field validation refers to comparisons between model predicitons of pavement cracking performance against the actual field cracking performance.

Table 2.5 Summary of Discrete Crack Models for Asphalt Mixtures

Model (Contributor)	Theoritical Basis for Model	Implementation in Pavement Structural Model (framework)	Laboratory Testing Requirements	Model Qualification, Verification, Calibration and Validation Status					Field Performance Prediction Status
				Q	V	C	V (Lab)	V (Field)	

Crack Growth Initiation Method (U. Limoges)	Viscoelasticity, energy release rate concept (Gθ approach)	No	- Viscoelastic characterization - Crack growth test at different temperatures and loading rates	X	X	X	X		Not applied at present but application is planned.
Cohesive Zone Model (U. Illinois)	Quasi-brittle fracture process zone characterization using fracture energy and cohesive strength. Potential based approach.	Yes (finite element analysis)	- Fracture energy testing (Typ.: Disk-shaped compact tension test, ASTM D7313) - Cohesive strength (Typ.: Indirect tensile strength test) - Viscoelastic characterization (Typ.: 1000 second indirect tensile creep test at 3 temperatures)	X	X	X	X	X	Applied for reflective and thermal cracking.
HMA-Fracture Mechanics Model (U. Florida)	LEFM extended to step-wise crack growth model and dissipated creep strain energy conc45ept	Yes (layered elastic analysis / boundary element analysis)	- Resilient modulus (Typ: Indirect tensile resilient modulus @ 10ºC) - Viscoelastic characterization (Typ: 1000 second indirect tensile creep test at @ 10ºC) - Tensile strength (Typ: Indirect tensile strength @ 10ºC) - Healing test (Typ. @ 20ºC)	X	X	X		X	Applied for fatigue (top-down and bottom-up) cracking

2.5 CONSTITUTIVE MODELS FOR CYCLIC DEGRADATION

2.5.1 Dissipated Energy Concept

2.5.1.1 Model Introduction

Asphalt is a viscoelastic material, thus it dissipates energy under mechanical work (loading and relaxation). Usually, in an elastic material the energy is stored in the system when the load is applied, all the energy is recovered when the load is removed; in this case the unloading and the loading curves coincide. Viscoelastic materials are characterised by a hysteresis loop because the unloaded material traces a different path to that when loaded (phase lag is recorded between the applied stress and the measured strain); in this case the energy is dissipated in the form of mechanical work, heat generation, or damage [67-68].

The area of the hysteresis loop represents the dissipated energy in a load cycle and the following equation can be used to calculate its value in a linear viscoelastic material subjected to sinusoidal loading:

$$W_i = \pi\sigma_i\varepsilon_i sin\varphi_i \tag{2.32}$$

Where,

W_i = Dissipated energy in cycle i,
σ_i = stress level in cycle i,
ε_i = strain level in cycle i, and
φ_i = phase angle in cycle i.

During a fatigue test, the stiffness reduces, the fatigue process starts and microcracks are induced in the material; therefore the dissipated energy, W_i, varies per loading cycle and it, usually, increases for controlled stress tests and decreases for controlled strain tests
An example of the evolution of hysteresis loop (dissipated energy) during a fatigue test is shown in Fig. 2.37.

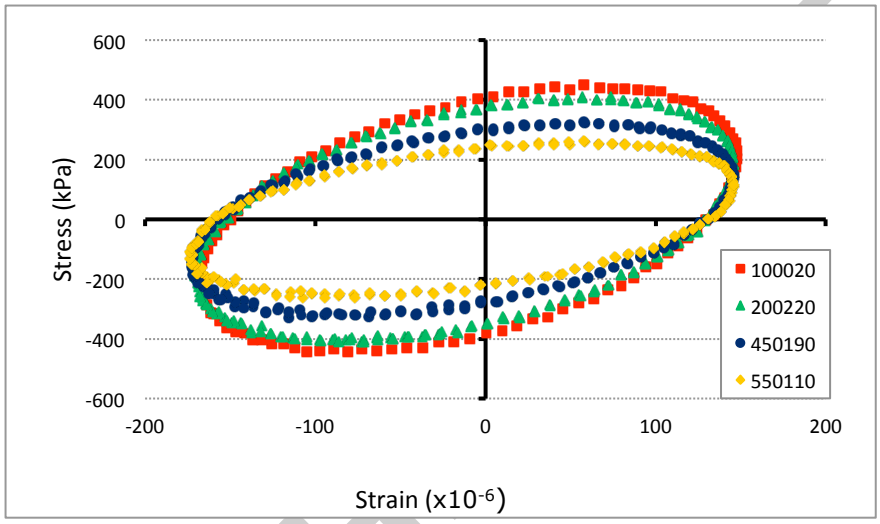

Fig. 2.37 Evolution of hysteresis loop during a fatigue test

2.5.1.2 Model Formulation

According to the classical fatigue analysis, fatigue life is conventionally defined as a number of cycles at which the stiffness modulus has decreased to the half of the initial value (see Fig. 3). The number of cycles to reach 50% of initial stiffness is inidicated by N_f^{50}. However, dissipated energy methods have been considered in order to determine the number of cycles to failure. Thus, a comparison between different fatigue failure criteria, based on dissipated energy concepts, and the conventional analysis is presented here.

The Energy Ratio ($R\varepsilon$) method is considered first. It was introduced by Hopman et al. in 1989 [42]. The Energy ratio is the cycle number where cracks are considerend to initiate ($N_f^{R\varepsilon}$). N_I is defined as the point at which the slope of the energy ratio versus the number of cycles deviates from a straight line. In a controlled strain test, energy ratio is defined as follows:

$$R_\varepsilon = \frac{nW_0}{W_i} = \frac{n(\pi\sigma_0\varepsilon_0 sin\varphi_0)}{\pi\sigma_i\varepsilon_i sin\varphi_i} \tag{2.33}$$

Where W_0 is the energy dissipated in the first cycle, W_i is the energy dissipated at i^{th} cycle. If the stress is replaced by the product of strain and modulus, and considering that the strain level remains constant for a strain controlled test, then the Eq. (2.33) can be simplified and written as follow [67]:

$$R_\varepsilon = \frac{n}{E_i^*} \tag{2.34}$$

Fig. 2.38 shows the energy ratio and complex modulus plotted as function of load cycles for an asphalt mixture. It can be seen that the number of cycles obtained by means of the classical analysis is generally greater than the energy ratio method.

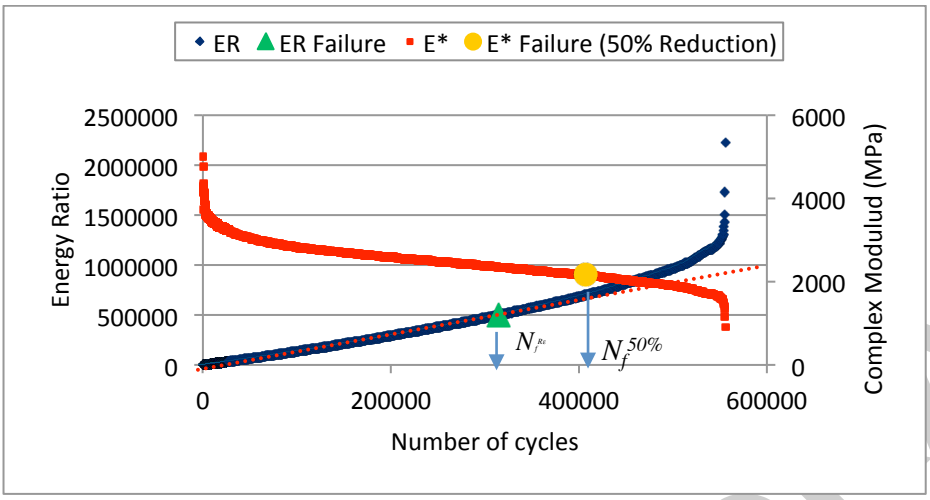

Fig. 2.38 Energy ratio versus number of load cycles at 20 ºC and at 15 Hz loading frequency

Fig. 2.39 shows the classical Whöler curves that represents the life duration versus applied strain amplitude. In the conventional approach, the relationship between applied strain ε_0 and load cycle to failure N_f is often times presented in a power function [21]:

$$N_f = K_1(\varepsilon_0)^{-k_2} \tag{2.35}$$

Where K_1 and K_2 are the intercept and the slope, respectively. These are determined experimentally and they seem to be highly correlated. Researchers [69-71] believe that mode of loading, testing temperature, frequency and asphalt content has a more significant effect on the K_1-K_2 relation than asphalt type, air voids levels and aggregate gradation. Fig. 2.40 shows the cumulative dissipated energy versus load cycle curve.

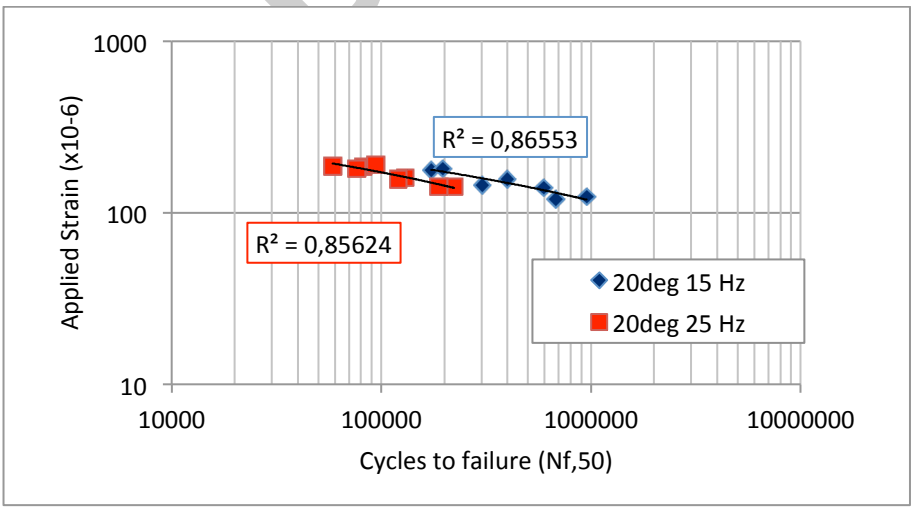

Fig. 2.39 Classical fatigue life curves obtained at 20 ºC at 15 Hz and 25 Hz loading frequencies.

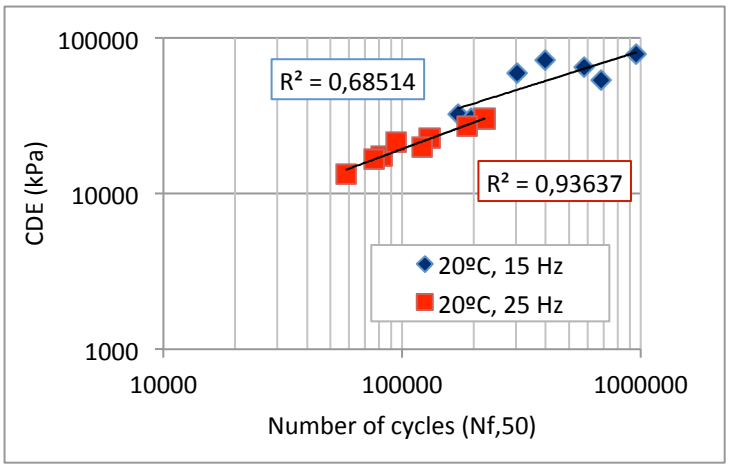

Fig. 2.40 Cumulative dissipated energy versus load cycle curve obtained at 20 ºC at 15 and 25 Hz loading frequencies.

Van Dijk and Visser [72] performed some of the early research to consider dissipated energy as a fatigue parameter. This work determined an equation that relates the cumulative dissipated energy (W_f) to the number of cycles to failure as shown in Eq. (2.36):

$$W_f = A\left(N_f^{W_f}\right)^z \tag{2.36}$$

Where W_f is the cumulative dissipated energy to failure, i.e. the total energy dissipated by the material during the fatigue test (sum of all areas within the stress-strain hysteresis loop for every cycle until failure); $N_f^{W_f}$ is the number of load cycle to failure, and A, z are the mixture dependent parameters that are determined experimentally.

The cumulative dissipated energy has not shown very good promise to be a parameter to describe the fatigue performance in asphalt materials, as it does not distinguish the amount of dissipated energy due to damage as opposed to viscous dissipation. Also, Eq. (2.36) is not unique it was found that it changes depending on the mode of loading, loading frequency and temperature. The same result was found by SHRP study for stress controlled tests [73].

Some researchers [74-75] have suggested the Ratio of Dissipated Energy Change (*RDEC*) as a parameter to describe fatigue in asphalt materials. The same researchers believe that the *RDEC* is a true indicator of damage because it is able to eliminate the other forms of dissipated energy due to mechanical work or heat generation. Therefore, it can be considered a good parameter to describe the fatigue process in asphalt, and is calculated with the following expression:

$$RDEC = \frac{DE_{n+1} - DE_n}{DE_n} \tag{2.37}$$

Where *RDEC* is ratio of the dissipated energy change per load cycle, DE_n is dissipated energy produced in load cycle n, and DE_{n+1} is dissipated energy produced in load cycle $n+1$. Fig. 2.41 shows the variation of the *RDEC* and the complex modulus ratio (E^*/E_0) plotted against the number of load cycles. Complex modulus ratio is ratio of the complex modulus in the current cycle normalized against complex modulus from first load cycle.

In case of asphalt mixtures, three main phases during a fatigue test have been suggested. The *RDEC*, after a rapid decrease (I stage), reaches a plateau stage in which a plateau value (*PV*) can be obtained, corresponding to the *RDEC* value when initial stiffness modulus has been reduced of half. This represents an energy plateau where an almost constant rate of

energy input is being turned into damage. Researchers have validated that the *PV* is uniquely related to fatigue life. After the *RDEC* increases rapidly until true fatigue failure (III stage).

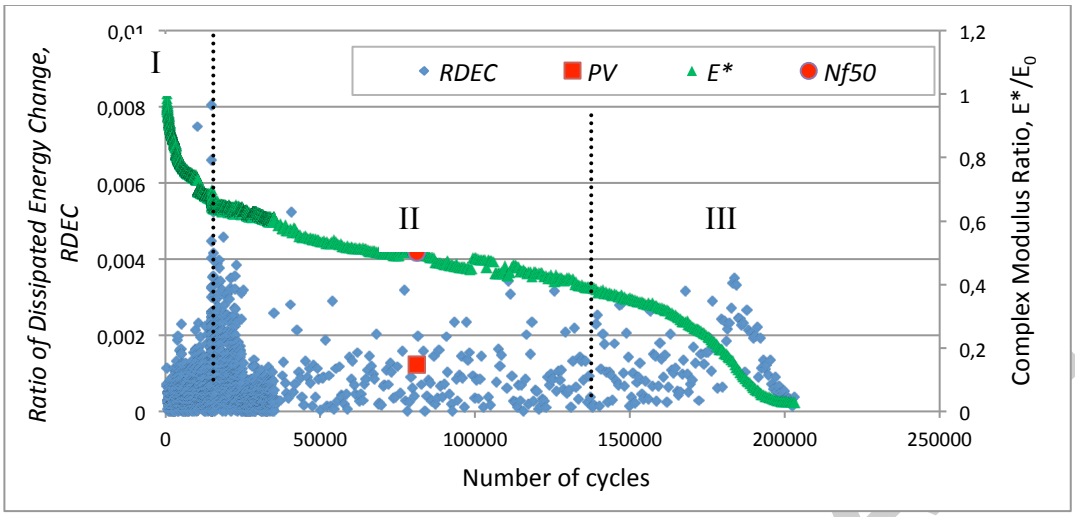

Fig. 2.41 RDEC vs Load cycle curve obtained at 20 degrees at 15 Hz

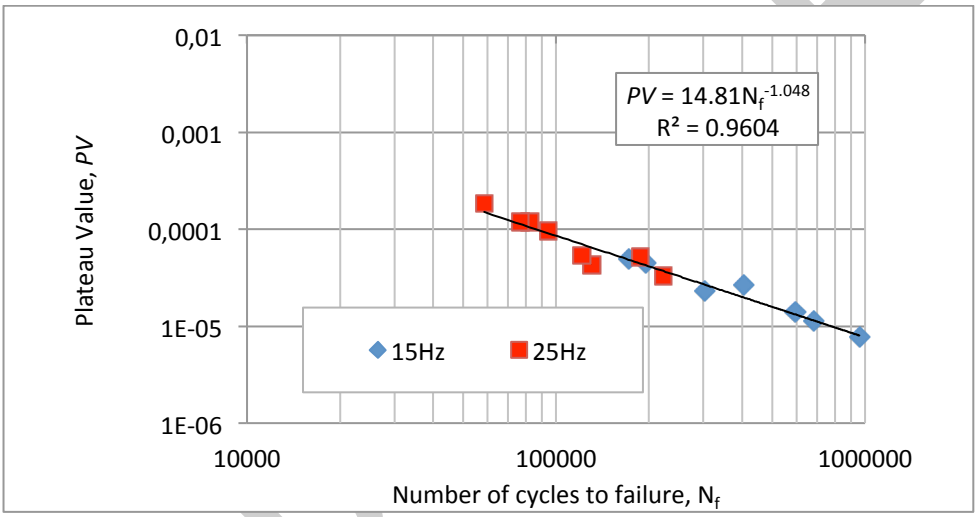

Fig. 2.42 PV vs number of cycles obtained at 20 degrees at 15 Hz and 25Hz

One challenge associated with the use of *RDEC* plateau value based approach is to find the value of *PV*. Often it is not easy to obtain the *PV* from experimental data and also they contain a high amount of dispersion. A hypothesis that has been proposed is that if the dissipated energy curve follows a power law relationship ($DE=AN_f^k$), the *RDEC* can be simplified, considering the exponential slope of the power law *k*, as follows:

$$\mathrm{RDEC} = \frac{1-\left(1+\frac{100}{a}\right)^{k}}{100} \tag{2.38}$$

Also in this case, it is not so easy to determine the PV depending on the evolution of the dissipated energy during the fatigue test. However, the plateau value is correlated with a number of fatigue cycles to failure by means of a statistical approach, using the following equation [74] [76].

$$PV = cN_f{}^{d} \tag{2.39}$$

The value of the constants c and d are determined experimentally. The coefficient d typically varies from -0.80 and -1.60 [76]. It can be seen from the experimental curve the fit the experimental data from both frequencies (15 and 25 Hz) is characterised by a coefficient d equal to -1.048 (see Fig. 2.42).

2.5.2 Non-local Modeling of Fatigue Microcracking with Application to Specimen Size Effects

2.5.2.1 Model Description

For a fatigue test with a sinusoidal loading and an offset equal to zero, the initial complex modulus of an undamaged material at the beginning of the test can be expressed as follows:

$$E_O^*(i\omega) = \frac{\sigma_0 e^{i\omega t}}{\varepsilon_0 e^{(i\omega t-\phi_0)}} = \frac{\sigma_0}{\varepsilon_0} e^{i\phi_0} = |E_O^*| e^{i\phi_0} \tag{2.40}$$

Where, E^* is complex modulus, ω is the frequency, ϕ is phase angle for initial cycle, σ is uniaxial stress and ε is uniaxial strain. The subscript for these variables represents the number of load cycle. After N cycles, the complex modulus is $|E_N^*| e^{i\phi_N}$ and the fatigue damage D induced by the micro cracks development within the material can be interpreted as a function of the ratio of $|E_N^*| e^{i\phi_N}$ to the initial complex modulus:

$$D = 1 - \frac{|E_N^*| e^{i\phi_N}}{|E_O^*| e^{i\phi_0}} \tag{2.41}$$

Assuming the phase angle of the complex viscoelastic modulus of the material is not locally affected by the damage growth, $\phi_N = \phi_0$ and the viscoelastic behaviour of the material can be deduced from an elastic model. The damage is then expressed as a function of the ratio of the corresponding Young's modulus E_O and E_N:

$$D = 1 - \frac{|E_N^*|}{|E_O^*|} \approx 1 - \frac{E_N}{E_O} \tag{2.42}$$

with D growing from 0 for the undamaged material to 1 when the material does not transfer stress anymore.

This damage D is introduced in the constitutive equations as a scalar affecting the material isotropic elastic tensor C_{ijkl}, function of the Young modulus E and the Poisson ratio ν :

$$\sigma_{ij} = (1-D) C_{ijkl} \varepsilon_{kl} \tag{2.43}$$

where σ_{i_j} and ε_{kl} are respectively the elastic stress and strain tensor components.

To be representative of a mode I cracking (opening), only the strains induced by the positive principal stresses (traction) σ_i are assumed to contribute to the cracking damage in the form of a scalar equivalent strain:

$$\tilde{\varepsilon} = \sqrt{\sum_{i=1,\dots,3} \frac{\langle \sigma_i \rangle^2}{E_o(1-D)}} \text{ where } \langle \sigma_i \rangle = \frac{1}{2}\left(|\sigma_i| + \sigma_i\right) \tag{2.44}$$

To avoid localisation problems in the structural computation, a non local integration of the equivalent strain can be applied as a mesh regularization method. This non local integration is realized through a convolution of the strain field with a normalized 3D Gaussian kernel: the local equivalent strain value $\tilde{\varepsilon}$ is replaced by a non-local equivalent strain $\bar{\varepsilon}$ equal to the Gaussian weighted average of $\tilde{\varepsilon}$ taken over a region about the point of interest.

$$\bar{\varepsilon} = \frac{1}{V_r(x)}\int_\Omega \Psi(x-s)\tilde{\varepsilon}(s)ds \text{ where } V_r(x) = \int_\Omega \Psi(x-s)ds \tag{2.45}$$

and $\Psi(x-s) = e^{\frac{-4|x-s|^2}{l_c^2}}$ a Gaussian function

For a sinusoidal loading, if the Miner's rule of linear additive damage is assumed, the Wöhler curves are respected for a damage evolution law of the form [77] :

$$\dot{D} = f(D)\varepsilon^\beta \langle \dot{\varepsilon} \rangle \tag{2.46}$$

The damage growth relationship component $f(D)$ is defined by the following mathematical expression:

$$f(D) = \frac{\alpha 2}{\alpha 1 \alpha 3}\left(\frac{D}{\alpha 2}\right)^{1-\alpha 3} e^{\left(\frac{D}{\alpha 2}\right)^{\alpha 3}} \tag{2.47}$$

The model is implemented in a finite element code with parameters $\beta, \alpha 1, \alpha 2, \alpha 3$ to be material properties.

2.5.2.2 Results of The Model Prediction for Study Of Specimen Size Effects

Numerical simulations were conducted for the three specimen sizes with a set of material parameters $\beta, \alpha 1, \alpha 2, \alpha 3$ evaluated on the bituminous mix used in previous research.
Comparison between the model predictions and the experimental results are presented for the three sizes (Figs. 2.43, 2.44 and 2.45) for the strain level 140x10^{-6}:

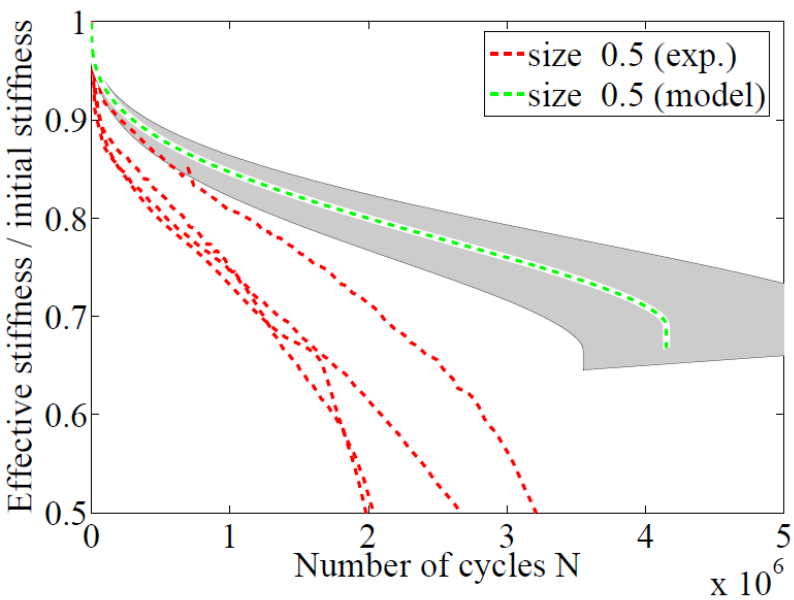

Fig. 2.43 Comparison between model predictions and experimental results (size 0.5)

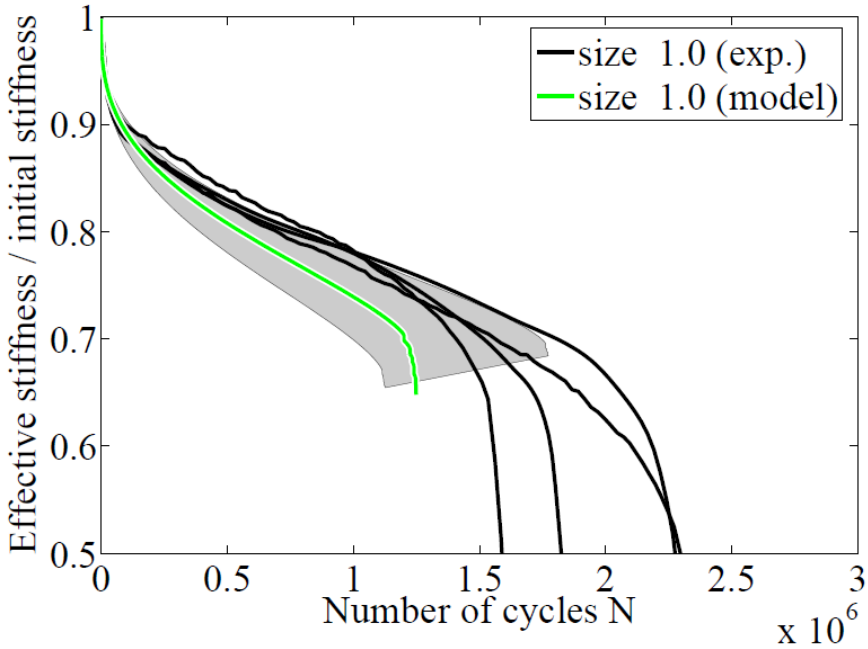

Fig. 2.44 Comparison between model predictions and experimental results (size 1)

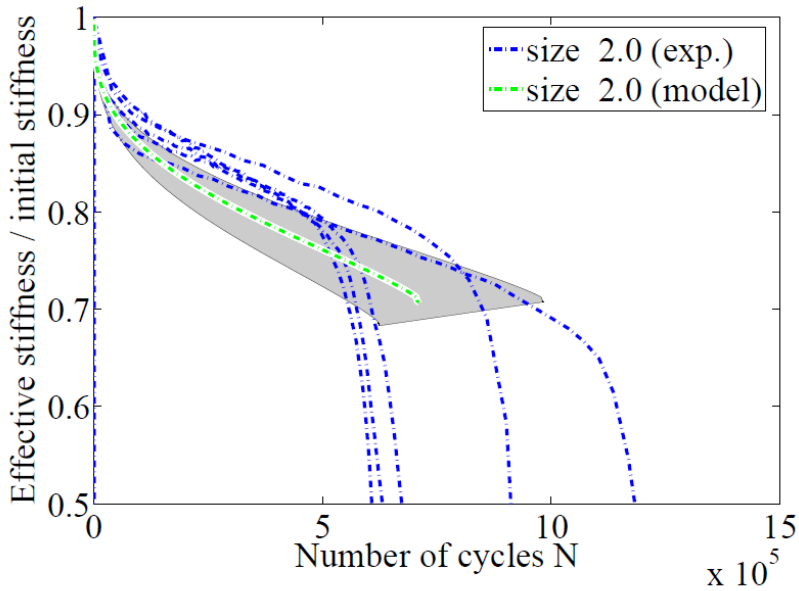

Fig. 2.45 Comparison between model predictions and experimental results (size 2)

The experimental trend for the number of cycle before rupture to increase as the size of the specimen decreases is reproduced by the simulation but this effect is over estimated for the smaller size. Model predicted and experimental Wöhler curves are compared in Fig. 2.46:

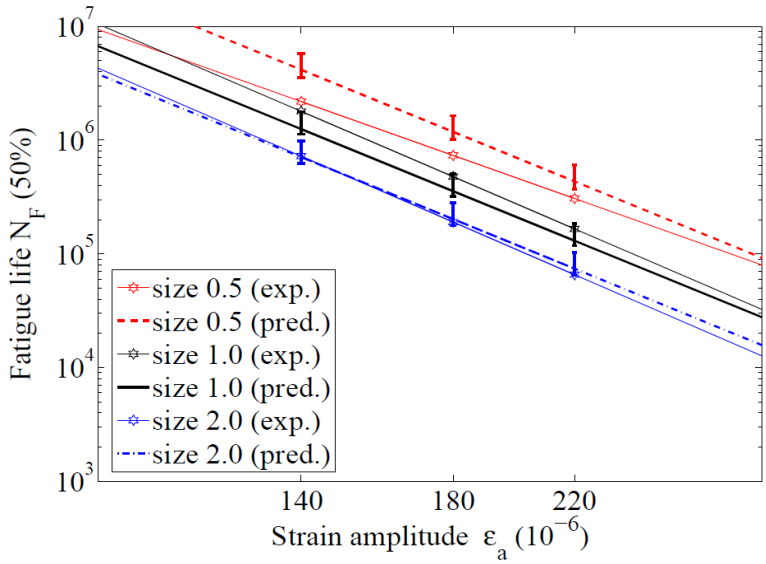

Fig. 2.46 Comparison between model predicted and experimental Wöhler curves

The model chosen implies parallel predicted Wöhler curves with a material dependent log-log slope equal to $-(\beta+1)$. This is not the case for the experimental Whöler curves with a significantly different slope for the experimental curve obtained for the smaller samples (size 0.5).

The model prediction/experimental differences could thus be explained by viscoelastic thermal effects, affecting the β parameter induced by the material self-heating neglected in the modelling.

2.5.3 Viscoelstoplastic Continuum Damage Model

2.5.3.1 Model Introduction

The viscoelastoplastic continuum damage (VEPCD) model in tension is based on (1) the elastic-viscoelastic correspondence principle, (2) continuum damage mechanics to account for the effect of microcracking on the constitutive behavior, (3) a time- and stress-dependent viscoplastic model to account for the plastic and viscoplastic behavior, and (4) the time-temperature superposition (TTS) principle with growing damage to describe the effect of temperature on the constitutive behavior. The resulting models are integrated by the strain decomposition approach to form the VEPCD model. These principles are briefly described below.

2.5.3.2 Time-Temperature Superposition (TTS) with Growing Damage

If the time-temeprature superposition principle can be extended to outside of the linear viscoelastic (LVE) range for asphalt mixtures, its impact is significant in terms of testing requirements and efficiency in modeling.

The TTS with growing damage can be verified using a simple technique where stress and time are determined at a strain level from the constant crosshead rate monotonic tests at different rates and temperatures. The corresponding time is converted to reduced time with the time-temperature shift factors from LVE characterization (e.g., frequency and temperature sweep dynamic modulus tests) and plotted with the respective stress. If the resulting graph, for a wide range of strain levels, appears continuous, then TTS with growing damage is said

to be verified. Details on the theoretical background of this technique can be found in Chehab et al. [78].

Chehab et al. [78] demonstrated that the thermorheologically simple (TRS) behavior extends well beyond the LVE limits to highly damaged levels for asphalt concrete in tension. Underwood et al. [79] proved that TTS with growing damage is valid for various modified asphalt mixtures. Other researchers (Zhao [80]; Gibson et al. [81]; Kim et al. [82]) also found that asphalt concrete in compression is TRS at high strain levels with damage.

The importance of this finding lies in the reduction of testing conditions required for modeling purposes. Once the behavior at a given temperature is known, the behavior at any other temperature can be predicted using the LVE shift factors. In terms of the VEPCD model, this principle is considered by replacing physical times with reduced times, generally calculated from Eq. (2.48), or more specifically by Eq. (2.49) if temperature does not change with time:

$$\xi = \int_0^t \frac{dt}{a_T} \tag{2.48}$$

$$\xi = \frac{t}{a_T} \tag{2.49}$$

For the remainder of the discussion on this model, the formulations are presented using the reduced time (ξ) instead of the physical time (t), based on the TTS principle with growing damage.

2.5.3.3 Viscoelastic Continuum Damage (VECD) Model

The viscoelastic strain in the VEPCD model covers both linear viscoelasticity and the damage due to microcracking. The VECD model forms the basis for the viscoelastic strain. This model is based on two principles: the elastic-viscoelastic correspondence principle based on pseudo strain and the continuum damage mechanics-based work potential theory.

The stress-strain relationships for many viscoelastic materials can be represented by elastic-like equations through the use of so-called *pseudo* variables. This simplifying feature enables a class of extended correspondence principles to be established and applied to linear as well as some nonlinear analyses of viscoelastic deformation and fracture behavior [83]. Using these correspondence principles, one can obtain viscoelastic solutions from their elastic counterparts through a simple conversion procedure. The usual Laplace transform-based correspondence principle is limited to LVE behavior with time-varying boundary conditions, whereas the correspondence principles based on pseudo variables are applicable to both linear and nonlinear behavior of a class of viscoelastic materials with stationary or time-dependent boundary conditions. Also, the latter does not require a transform inversion step to obtain the viscoelastic solutions but rather requires a convolution integral which is much easier to handle than the inversion step.

Consider a stress-strain equation for linear viscoelastic materials,

$$\sigma_{ij} = \int_o^{\xi} E_{ijkl}(\xi - \tau) \frac{\partial \varepsilon_{kl}}{\partial \tau} d\tau \tag{2.50}$$

where σ_{ij}, ε_{kl} = stress and strain tensors;
$E_{ijkl}(t)$ = the relaxation modulus matrix;
$\xi = t/a_T$ = reduced time;
t = physical time;
a_T = the time-temperature shift factor; and

τ = the integration variable.

Eq. (2.50) can be written as

$$\sigma_{ij} = E_R \varepsilon_{kl}^R \quad or \quad \varepsilon_{kl}^R = \frac{\sigma_{ij}}{E_R} \tag{2.51}$$

if we define

$$\varepsilon_{kl}^R = \frac{1}{E_R}\int_o^{\xi} E_{ijkl}(\xi - \tau)\frac{\partial \varepsilon_{kl}}{\partial \tau} d\tau \tag{2.52}$$

where E_R is termed the *reference modulus*, which is a constant and has the same dimension as the relaxation modulus, $E_{ijkl}(t)$. The usefulness of Eq. (2.51) is that a correspondence can be found between Eq. (2.51) and the linear elastic stress-strain relationship. That is, the equations in Eq. (2.51) take the form of *elastic* stress-strain equations even though they are actually *viscoelastic* stress-strain equations. The ε_{kl}^R is called the *pseudo strain*. The pseudo strain accounts for all the hereditary effects of the material through the convolution integral. The reference modulus, E_R, is introduced here because it is a useful parameter in discussing special material behaviors and introducing dimensionless variables. For example, if we take $E_{ijkl}(t) = E_R$ in Eq. (2.52), we obtain $\varepsilon_{kl}^R = \varepsilon_{kl}$, and Eq. (2.51) reduces to the linear elastic equation $\sigma_{ij} = E_{ijkl}\varepsilon_{kl}$ or $\varepsilon_{kl} = \sigma_{ij}/E_{ijkl}$. If we take $E_R = 1$ in Eq. (2.52), pseudo strains are simply the linear viscoelastic stress response to a particular strain input. For the remainder of this chapter, E_R is set to one. The results from experimental verification of the correspondence principle have been documented by Kim and Little [84], Kim et al. [85], and Lee and Kim [86] using uniaxial monotonic and cyclic data of asphaltic materials under a wide range of test conditions.

The material property needed to calculate the pseudo strain in Eq. (2.52) is the relaxation modulus. Typically, the relaxation modulus test is not easy to perform due to the large amount of stress that develops at the beginning of the test from the step input of displacement. Therefore, the relaxation modulus is determined from the complex modulus using the theoretical inversion process. Alternatively, the relaxation modulus can also be determined from creep compliance mastercurve through inversion process.

Because the complex modulus tests are performed on a separate set of representative specimens for the mixture in question, the relaxation modulus determined from the complex modulus tests may not be the same as the one for specimens used in damage testing due to sample-to-sample variability. In order to minimize the effect of the sample-to-sample variability, the dynamic modulus ratio, *DMR*, is introduced. The *DMR* is the ratio between the dynamic modulus of a test specimen determined from a fingerprint dynamic modulus test performed at 10 Hz right before the fatigue test and the dynamic modulus determined at the fingerprint test temperature and 10 Hz from the mastercurve generated from separate specimens using the time-temperature superposition.

Thus, the governing constitutive equation in uniaxial mode becomes

$$\sigma = DMR\ \varepsilon^R \tag{2.53}$$

where

$$\varepsilon^R = \frac{1}{E_R}\int_o^{\xi} E(\xi - \tau)\frac{\partial \varepsilon}{\partial \tau} d\tau \tag{2.54}$$

In most cases, the *DMR* value remains between 0.9 and 1.1. When the *DMR* value is significantly out of this range, a re-examination of the data (both the relaxation modulus and test results) is necessary.

A state variable based appraich is recommended for pseudo-strain calcualaiton due to its efficiency over piece-wise linear approximation which is fundamentally sound but computationally inefficient.

2.5.3.4 Work Potential Theory

Fig. 2.47(a) shows typical stress versus pseudo strain hysteresis loops for an asphalt muixture at different numbers of cycles in the controlled-stress cyclic test. Relatively high stress amplitude is used to induce significant damage in the specimen. Unlike the negligible damage case, change in the slope of each $\sigma - \varepsilon^R$ cycle (i.e., reduction in the pseudo stiffness of the material) can be observed from this figure due to the damage incurred in the specimens.

The effect of damage on pseudo stiffness can also be seen in the monotonic data shown in Fig. 2.47(b). In this figure, the stress-pseudo strain curves deviate from the line of equality as damage grows. Also, the onset of this deviation occurs at different times as the rate of loading changes, indicating the presence of the rate-dependent damage mechanism. On basis of these observations, the following uniaxial versions of constitutive equations are presented for linear elastic and linear viscoelastic bodies with and without damage. They also show how models of different complexity may evolve from simpler ones.

Elastic Body without Damage: $\sigma = E\varepsilon$ (2.55)

Elastic Body with Damage: $\sigma = C(S_m)E\varepsilon$ (2.56)

Viscoelastic Body without Damage: $\sigma = E_R\varepsilon^R$ (2.57)

Viscoelastic Body with Damage: $\sigma = C(S_m)E_R\varepsilon^R$ (2.58)

where $C(S_m)$ indicates that C is a function of damage parameters, S_m. The function, $C(S_m)$, represents the changing *stiffness* of the material due to growing damage. Eq. (2.58) results from Eqs. (2.55), (2.56), and (2.57). The form of Eq. (2.58) is also supported by the observations made in Fig. 2.47; i.e., the pseudo stiffness changes as the damage grows. To determine an analytical representation of the damage function, C, the work potential theory, the continuum damage mechanics principle developed by Schapery [87], is adopted.

In continuum damage mechanics, the damaged body can be viewed as a homogeneous continuum on a macroscopic scale, and the influence of damage is typically reflected in terms of reduction in stiffness or strength of the material. The state of damage can be quantified by a set of parameters often referred to as *internal state variables* or *damage parameters* in the context of thermodynamics of irreversible processes. The growth of damage is governed by an appropriate damage (or internal state) evolution law. The *stiffness* of the material, which varies with the extent of damage, is determined as a function of the internal state variables by fitting the theoretical model to available experimental data.

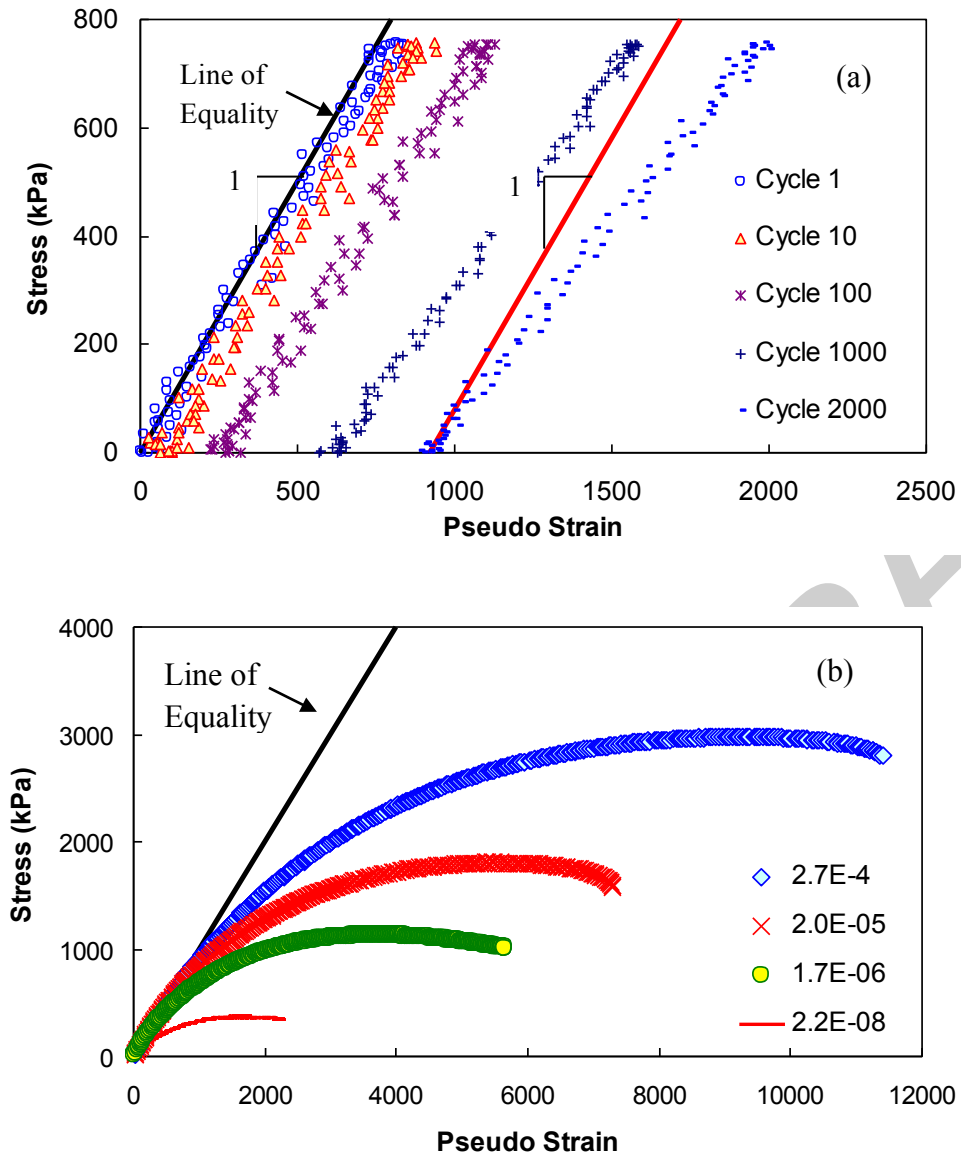

Fig. 2.47 Stress-Pseudo Strain Behavior of Asphalt Concrete in: **(a)** Controlled-Stress Cyclic Test; **(b)** Constant-Strain-Rate Monotonic Test (different symbols represent different strain rates)

When damage occurs due to external loading, the work done on the body is not entirely stored as strain energy; part of it is consumed in causing damage to the body. The amount of energy required to produce a given extent of damage is expressed as a function of *internal state variables*. The total work input to the body during the processes in which damage occurs depends, in general, on the path of loading. However, it has been observed that, for certain processes in which damage occurs, the work input is independent of the path of loading [88-89].

Schapery [87] applied the method of thermodynamics of irreversible processes and the observed phenomenon of path independence of work in damage-inducing processes to develop the work potential theory so that it may be applicable to describing the mechanical behavior of elastic media with growing damage and other structural changes. The theory is general enough to allow for strong nonlinearities and coupling between the internal state variables and to describe a variety of mechanisms including micro- and macrocrack growth in

monolithic and composite materials. Sicking [90] applied the theory to model the damage-related material nonlinearity in graphite-epoxy laminates, and Lamborn and Schapery [91] showed the existence of a work potential for suitably limited deformation paths using experimental data from axial and torsional deformation tests on angle-ply fiber-reinforced plastic laminates. The elements of work potential theory in terms of a strain energy formulation may be represented as follows:

Strain Energy Density Function: $W = W(\varepsilon_{ij}, S_m)$ (2.59)

Stress-Strain Relationships: $\sigma_{ij} = \dfrac{\partial W}{\partial \varepsilon_{ij}}$ (2.60)

Damage Evolution Laws: $-\dfrac{\partial W}{\partial S_m} = \dfrac{\partial W_S}{\partial S_m}$ (2.61)

where σ_{ij} are stresses, ε_{ij} are strains, S_m are internal state variables (or damage parameters), and $W_S = W_S(S_m)$ is the dissipated energy due to damage growth. The internal state variables, S_m (m=1,2,..., M), account for the effects of damage, and the number of internal state variables (i.e., M) is typically determined by the number of different mechanisms governing the damage growth. Eq. (2.61) is similar to a crack growth equation (e.g., $\boldsymbol{G} = \boldsymbol{G}_c$, where $\boldsymbol{G}$ is the energy release rate and $\boldsymbol{G}_c$ is the fracture toughness) and, in fact, Eq. (2.61) is used to find S_m as functions of ε_{ij}. The left-hand side of Eq. (2.61) is the *available* thermodynamic force, while the right-hand side is the *required* force for damage growth.

Based on the elastic-viscoelastic correspondence principle, the strains, ε_{ij}, that appear in the elastic damage model, Eqs. (2.59)-(2.61), are replaced with corresponding pseudo strains, ε_{ij}^R, defined by Eq. (2.52). Then, according to the correspondence principle, the set of equations written in terms of pseudo strains now governs the corresponding viscoelastic damage problem. It was found from experimental studies (e.g., [92]), however, that the damage evolution laws for elastic materials cannot be translated directly into evolution laws for viscoelastic materials through the correspondence principle. Not only is the available force for growth in S_m rate-dependent, but the resistance against the growth of S_m is rate-dependent for most viscoelastic materials. The following evolution laws, which are similar in form to the well-known power-law crack growth laws for viscoelastic materials [93], are adopted in this study as they can reasonably represent the actual damage evolution processes in many viscoelastic materials:

$$\dot{S}_m = \left(-\frac{\partial W^R}{\partial S_m} \right)^{\alpha_m} \tag{2.62}$$

where $W^R = W^R(\varepsilon_{ij}^R, S_m)$ is the pseudo strain energy density function, $\dot{S}_m$ is the damage evolution rate, and α_m are material-dependent constants related to the viscoelasticity of the material. Eq. (2.62) is similar to the crack propagation rate equation. The same form of evolution laws has been used successfully in describing the behavior of a filled elastomer with growing damage [92] [94] also adopted the work potential theory in modeling the rate-dependent behavior of asphalt-aggregate mixtures under constant strain rate monotonic loading.

Finally, the work potential theory applied to viscoelastic media with the rate type damage evolution law is represented by the following three components for the uniaxial loading condition:

Pseudo Strain Energy Density Function: $W^R = W^R(\varepsilon^R, S_m)$ (2.63)

Stress-Strain Relationship: $\sigma = \dfrac{\partial W^R}{\partial \varepsilon^R}$ (2.64)

Damage Evolution Law: $\dot{S}_m = \left(-\dfrac{\partial W^R}{\partial S_m} \right)^{\alpha_m}$ (2.65)

2.5.3.5 Determination of Material Parameters

The work potential theory specifies an internal state variable, S_m, to quantify damage, which is defined as any microstructural changes that result in an observed stiffness reduction. The method used to solve the damage evolution law in Eq. (2.65) is a matter of preference. Lee and Kim [86] proposed a solution that utilizes the chain rule and makes no assumption regarding α. The solution of these researchers is presented in Eq. (2.66) It is noted that both methods have been successfully applied in asphalt concrete research [94-96].

$$S_{i+1} = S_i + \left[-\frac{1}{2}\left(C_i - C_{i-1}\right)\left(\varepsilon_i^R\right)^2 \right]^{\frac{\alpha}{1+\alpha}} \Delta t^{\frac{1}{1+\alpha}} \tag{2.66}$$

This method assumes that the rate of change in damage is constant over some discrete time step. This rate of change is determined at a point near the current value of damage ($S_i+\delta S$) where the extrapolation error is minimized. The method begins with an initial calculation of S by either of the approximate methods, both of which require results from constant crosshead rate tests for the stress-pseudo strain relationship. The initial S values are plotted with the pseudo stiffness values, C, calculated from the following relationship, which is obtained from Eq. (2.58):

$$C = \frac{\sigma}{I \times \varepsilon^R} \tag{2.67}$$

The C and initial S values are then fit to some mathematical form, such as the one presented in Eq. (2.68), where a and b are fitting parameters:

$$C = e^{aS^b} \tag{2.68}$$

Returning to the damage evolution law, and noting that the increments of time are generally small, one can write the rate of change in damage as

$$\frac{dS}{dt} = \frac{\Delta S}{\Delta t} \tag{2.69}$$

Substituting this expression into Eq. (2.65), and rearranging and writing in the discrete form, one finds the following equation:

$$S_{i+1} = S_i + \Delta t \left(-\frac{\left(\delta W_d^R\right)_i}{\delta S} \right)^{\alpha} \tag{2.70}$$

It must be observed that for the uniaxial case, the work function (W^R) is given by

$$W^R = \frac{1}{2} C\left(S\right) \varepsilon^R \tag{2.71}$$

Substituting Eq. (2.71) into (2.70) and simplifying, one arrives at

$$S_{i+1} = S_i + \Delta t\left(-\frac{1}{2}\left(\varepsilon^R\right)^2 \frac{\left(\delta C\right)_i}{\delta S}\right)^{\alpha} \tag{2.72}$$

In Eq. (2.72), it is assumed that before loading occurs, S and C are zero and one, respectively. Further, δS must be specified and should be significantly less than the change in damage over a time step (typically, 0.1 is used). After calculating the value of damage (S_i) and the incremental damage ($S_i+\delta S$) at a given time step, the corresponding values of C are found by Eq. (2.68). The difference between these values (δC) is then used to calculate damage at the next time step. The process is repeated until all data points are processed.

After completing this first iteration, the new values of S are plotted against the original pseudo stiffness values, and a new analytical relationship is found. The entire process is repeated until the change in successive iterations is small. In this research, eight such iterations were performed, but it was noted that very little improvement was made after the third or fourth iteration.

Daniel and Kim [95] studied the relationship between damage parameter (S) and the normalized pseudo secant modulus (C) under varying loading conditions. The most significant finding from their study is that a unique damage characteristic relationship exists between C and S, regardless of loading type (monotonic versus cyclic), loading rate, and stress/strain amplitude. In addition, the application of the TTS principle with growing damage to the C versus S relationships at varying temperatures yields the same damage characteristic curve in the reduced time scale. The only condition that must be met in order to produce the damage characteristic relationship is that the test temperature and loading rate combination must be such that only the elastic and viscoelastic behaviors prevail with negligible, if any, viscoplasticity. When the test temperature is too high or the loading rate is too slow, it was found that the C versus S curve deviates from the characteristic curve.

To ensure that the test temperature is low enough and the loading rate is fast enough not to induce any significant viscoplastic strains, the tests are performed at a low temperature (typically 5°C) with varying loading rates. If the C versus S curves at different rates overlap to form a unique relationship, the combinations of the temperature and loading rate are sufficiently satisfactory to develop the damage characteristic relationship.

Finally, the VECD model is

$$\sigma = C(S)\varepsilon^R \tag{2.73}$$

or

$$\varepsilon_{ve} = E_R \int_0^{\xi} D\left(\xi - \tau\right) \frac{d\left(\dfrac{\sigma}{C(S)}\right)}{d\tau} d\tau \tag{2.74}$$

by converting Eq. (2.73) to predict the viscoelastic strain. Note that E_R in Eq. (2.74) is set to one and that the *DMR* is not used in Eq. (2.73). *DMR* is only necessary in calibrating the model using the experimental data from several replicate specimens.

The major advantage of the damage characteristic relationship is that it allows a reduction in testing requirements. Since the same relationship exists in monotonic and cyclic tests, the material behavior under cyclic loading can be predicted from the damage characteristic curve characterized from the much simpler monotonic tests. Daniel and Kim [95] have verified that this approach can predict the fatigue life of asphalt concrete within the sample-to-sample variation.

2.5.3.6 Determination of VECD Model Parameters with Example from RILEM TC-CAP Material

The modeling techniques presented in the previous sections are applied to the asphalt concrete specimens fabricated by the research team at the University of Illinois at Urbana-Champaign. Two types of tests are required for the full VEPCD characterization: (1) temperature and frequency sweep dynamic modulus tests and (2) constant crosshead rate tests until failure. These tests were performed in direct tension using a MTS closed-loop servo-hydraulic loading frame. Table 1.6 summarizes the values of the VEPCD coefficients determined from the testing of the UIUC mixture. Figs. 2.48 and 2.49 show backcalculated viscoplastic strains.

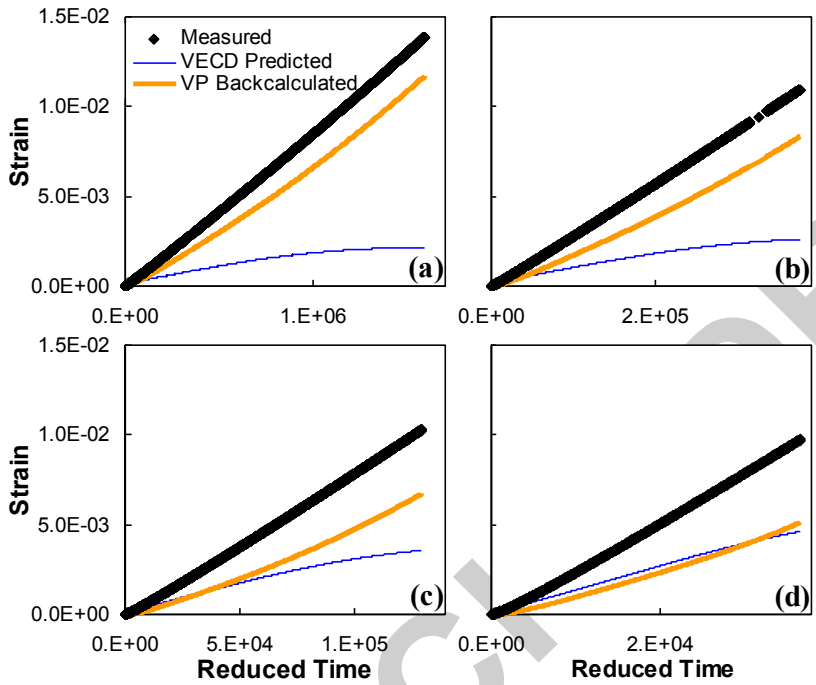

Fig. 2.48 Backcalculated viscoplastic strains from 40°C constant crosshead rate tests at: **(a)** 0.0003 ε/s, **(b)** 0.001 ε/s, (c) 0.003 ε/s and (d) 0.01 ε/s

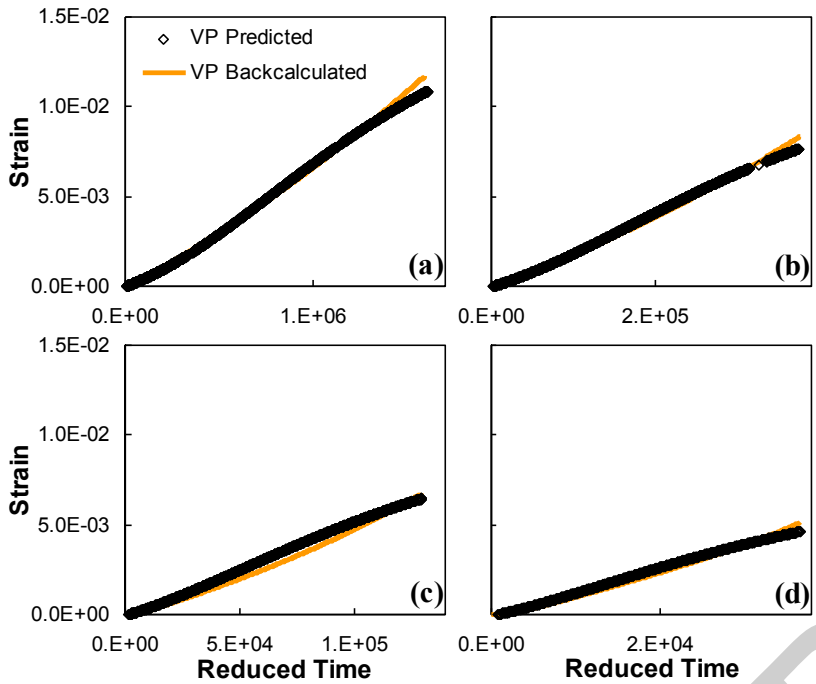

Fig. 2.49 Characterization of viscoplastic models from backcalculated viscoplastic strains from 40°C constant crosshead rate tests at: **(a)** 0.0003 ε/s, **(b)** 0.001 ε/s, **(c)** 0.003 ε/s and **(d)** 0.01 ε/s

It is noted that the VEPCD modeling techniques currently investigated by the NCSU research team are slightly different from the methodologies presented in this document. The basic principles of the VECD model are the same; however, the most recent form of the VECD model (so-called simplified VECD model) uses the data from a constant crosshead amplitude cyclic test instead of the monotonic test. More details on the simplified VECD model and its application can be found in Underwood et al. [97] and Hou et al. [98]. Also the current form of the viscoplastic model is a new type of rate model for explaining the behavior of asphalt concrete in compression using repeated creep and recovery tests. This model places an emphasis on capturing load history effects directly using viscoelastic-like convolution integrals. This approach leads naturally to a back stress concept that can be used to explain the effect of rest periods on the permanent deformation evolution.

Table 1.6 VEPCD coefficients for the UIUC mixture

Model			Coefficients
LVE	Shift Factor Function	a1	0.000223
		a2	-0.13514
		a3	0.670097
	Sigmoidal Function	a	1.999011
		b	2.40541
		d	1.646788
		g	0.729349
	Alpha		3.44
VECD	a		-0.00051
	b		0.589123

2.5.3.7 Summary of Models for Cyclic Degradation

The discussion of the models for characterization of asphalt mixturtes in terms of cyclic degradations or fatigue damage was presented in three sections. First section presented several different approaches that are used to represent asphalt mixture's cyclic degradation characteristics. These are typically used for purposes of comparing various mixturtes and have been used in an empirical manner to predict field performances. The other two approaches present formulations that are implemeneted within structural models (suc as, finite element analysis) and have been applied to better understand the cracking mechanisms in pavements. A summary of the approaches presented herein on the topic of cyclic degration models is described in Table 2.7. Similar to the table presented previously for comparisons of discrete crakcing models the the basis (theory/approach) behind the models, required laboratory tests/material parameters, status of the model in terms of model qualification, verification, calibration and validation, and the status of application of the models to simulate cracking performance of pavements are also presented.

Table 2.7 Summary of Discrete Crack Models for Asphalt Mixtures

Model (Contributor)	Basis for Model	Implementation in Pavement Structural Model (framework)	Laboratory Testing Requirements	Model Qualification, Verification, Calibration and Validation Status					Field Performance Prediction Status
				Q	V	C	V (Lab)	V (Field)	
Dissipated Energy Concepts for Fatigue Characterization (Different approaches: Enery ratio, DCSE, RDEC, PV) (U. Nottingham & IFSTTAR)	Empirical, energy dissipation rate, viscoelasticity	No	- Cyclic (fatigue) tests (uniaxial and flexural)	X		X	X		Applied for mixture design and preliminary pavement life predictions.
Non-local Model of Fatigue Microcracking (IFSTTAR)	Viscoelasticity, non-local damage distribution	Yes (Finite element analysis)	- Viscoelastic characterization (Typ.: Unixial complex modulus test) - Cyclic (fatigue) tests	X	X		X		Not applied at present but application is planned.
Continuum Damage Approach (North Carolina State U.)	Continuum damage, work potential theory, viscoelasticity	Yes (Layered viscoelastic analysis)	- Viscoelastic characterization (Typ.: Uniaxial complex modulus test) - Cyclic tests (Typ.: Constant cross-head pull-pull tensile tests)	X	X	X		X	Applied for fatigue (traffic and thermal effects) cracking

2.6 SUMMARY

2.6.1 Summary and Observations on The State of the Art for Laboratory Tests and Constitutive Models for Characterization of Fracture in Bulk Asphalt Material

This chapter provided a state of the art review of laboratory characterization and modelling tools that are currently available for understanding the fracture mechanisms of asphalt mixtures. This review demonstrated that significant progress has been made on this topic over past decade. The following table provides a summary of the laboratory tests presented in this review in terms of temperature conditions, loading rates and specimen requirements.

Below are some observations and remarks on the basis of the review presented herein:

- The use of fracture energy based testing procedures through use of notched specimens has shown great potential and such methods are becoming routine testing practice. The fracture energy has shown better correlation to extent of field cracking as opposed to strength based measures.
- The laboratory methods for evaluation of cyclic response of asphalt mixtures has progressed significantly as well. Major progress has been made on the use of advanced constitutive models to analyse the test results, such as, incorporation of material's viscoelastic response as well as use of dissipated energy concepts. Furthermore, the cyclic tests have become more robust through use of multi-axial strain measurements.
- The constitutive models for fracture in asphalt mixtures have become exceedingly robust and more representative of the physical processes associated with material's failure. The energy dissipation based approaches have been adopted for modelling of discrete cracks in the asphalt material, these approaches have shown promising results at capturing the critical cracking events for pavement thermal and reflective cracks. The use of Paris law based linear-elastic fracture mechanics models have been superceded by the energy based models.
- The constitutive models capable of capturing cracking in asphalt pavements under cyclic loading conditions have progressed in the phenomenological direction and have moved away from older empirical approaches that were based on data-fitted regression equations. Through use of thermo-viscoelastic modelling framework the recent modleing approaches are able to capture the effects of loading rate and temperature leading to higher prediction reliability.

2.6.2 Scientific Lack & Future Research Suggested

A unified laboratory test and model that can characterize and capture response of asphalt mixtures under all the modes that affect its properties (temperatres, loading rates, aging effect etc.) is desired. The present report demonstrates that the current state of the art in characterization and modelling of asphalt bulk fracture is capable of capturing material response under wide-range of conditions, however the the present approaches are still incapable of capturing all possible range of variables that affect fracture behaviour of asphalt mixtures.

The major scientific areas that is lacking in the field of fracture in bulk asphalt materials identified through this review include:

- Limited ability of models to capture both static and cyclic crack growths in an interchangable manner
- Models and tests are lacking fundamental understanding of healing processes

- Most laboratory tests and analysis procedures focus on use of global specimen reponses; more research is needed on incorporation of local material response from laboratory tests (see Chapter 4)
- Development of universal criteria from model qualification, verification and validation is needed

REFERENCES

1. Wagoner, M. P., W. G. Buttlar, Paulino, G.H. Disk-Shaped Compact Tension Test for Asphalt Concrete Fracture. Experimental Mechanics 45: 270-277 (2005)
2. Ahmed, S., Dave, E.V., Buttlar, W.G., Exline, M.K. Fracture Properties of Gap and Dense Graded Thin Bonded Overlays. Journal of the Association of Asphalt Paving Technologists 79: 443-446 (2010)
3. Ahmed, S., Dave, E., Behnia, B., Buttlar, W.G., Exline, M.K. Fracture Characterization of Gap-Graded Asphalt Mixtures and Thin Bonded Wearing Courses. International Journal of Pavement Research and Technology (3): 128-134 (2010)
4. Behnia, B., Dave, E.V., Ahmed, S., Buttlar, W.G., Reis, H. Investigation of Effects of the Recycled Asphalt Pavement (RAP) Amounts on Low Temperature Cracking Performance of Asphalt Mixtures using Acoustic Emissions (AE). Journal of the Transportation Research Board 2208: 64-71 (2011)
5. Wagoner, M.P., Buttlar, W.G. Influence of Specimen Size on Fracture Energy of Asphalt Concrete. Journal of Association of Asphalt Paving Technologists 76: 391-426 (2007)
6. Braham, A.F., Buttlar, M.P., Clyne, T.R., Marasteanu, M.O., Turos, M.I. The Effect of Long-Term Laboratory Aging on Asphalt Concrete Fracture Energy. Journal of the Association of Asphalt Paving Technologists 78: 417-454 (2009)
7. Hill, B.C., Behnia, B., Hakimzadeh, S., Buttlar, W.G., Reis, H. Evaluation of the Low Temperature Cracking Performance of WMA Mixtures. Journal of the Transportation Research Board (2012)
8. Buttlar, W.G., Ahmed, S., Dave, E.V. Braham, A.F. Comprehensive Database of Asphalt Concrete Fracture Energy and Links to Field Performance. Paper presented at the 89th Annual Meeting of the Transportation Research Board. Washington, D.C. (2010)
9. Ahmed, S. Fracture Characterization of Thin Bonded Asphalt Concrete Overlay Systems. Urbana-Champaign: University of Illinois. (2010)
10. Nguyen M.L., Di Benedetto H., Sauzéat C., Wendling L. Investigation of cracking in bituminous mixtures with a four point bending test. 6th RILEM International Conference on Cracking in Pavements. Chicago, Illinois. 16-18 (2008)
11. Lemaistre, H. Etude des propriétés thermomécaniques de divers réfractaires. Lyon: INSA (1998)
12. Jiang, F., Rohatgi, A., Vecchio, K.S., Adharapurapu, R.R. Crack length calculation for bend spe-cimens under static and dynamic loading. Engineering Fracture Mechanics 71: 1971-1985 (2004)
13. Wendling, L., Xoline, E., Gimenez, D., Reynaud, P., De La Roche, C., Chevalier, J., Fantozzi, G. Characterisation of crack propagation in butuminous mixtures. Fifth International RILEM Conference on Cracking in Pavements. Limoges, France. 639-646 (2004)
14. Mandel, J. Sur les corps visco-élastiques à comportment linéaire. Comptes rendus del l'Académie des Sciences 241: 1910-1912 (1955)
15. Nguyen, M.L. Etude de la propagation de fissure dans les enrobés bitumineux. Master of Civil Engineering, University of Lyon/ENTPE, Lyon [in French] (2005)
16. Tapsoba, N. Fissuration des enrobés bitumineux. Lyon: University of Lyon/ENTPE (2008)

17. Di Benedetto, H., Corté, J.F. Matériaux routiers Tome 2, Vol. 2, Hermes [in French] (2005)
18. Birgisson, B., Montepara, A., Romeo, E., Roncella, R., Tebaldi, G., Roque, R. The use of digital image correlation for accurate determination of fracture energy density in Hot Mix Asphalt (HMA). 6th RILEM International Conference on Cracking in Pavements. Chicago Illinois, 2008: 811-820 (2008)
19. Simonin, F. Comportement thermomécanique de béton réfractaires alumineux contenant du spinelle de magnésium. PhD Thesis, INSA Lyon [in French] (2000)
20. Nguyen, M.L. Etude de la fissuration et de la fatigue des enrobés bitumineux. PhD Thesis, University of Lyon/ENTPE, Lyon [in French] (2009)
21. Di Benedetto, H., De La Roche, C., Baaj, H., Pronk, A., Lundstrom, R. Fatigue of bituminous mixtures. Materials and Structures 37 (267): 202-216 (2004)
22. Di Benedetto, H., Delaporte, B., Sauzéat, C. Three-dimensional linear behavior of bituminous materials: Experiments and modeling. International Journal of Geomechanics 7 (2): 149-157 (2007)
23. Delaporte, B., Di Benedetto, H., Chaverot, P., Gauthier, G. Linear viscoelastic properties of bituminous materials: From binders to mastics. Proceeding AAPT. San Antonio, TX. 455-494 (2007)
24. Delaporte, B., Di Benedetto, H., Chaverot, P., Gauthier, G. Linear Viscoelastic Properties of Bituminous Materials Including New Products Made with Ultrafine Particles. Road Materials and Pavement Design 10 (1): 7-38 (2009)
25. Pouget, S., Sauzeat, C., Di Benedetto, H., Olard, F. From the Behavior of Constituent Materials to the Calculation and Design of Orthotropic Bridge Structures. Road Materials and Pavement Design 11 (SI EATA): 111-144 (2010)
26. Di Benedetto, H., Nguyen, H.M., Pouget, S., Sauzéat, C. Time-Temperature superposition principle for bituminous mixtures: Three dimensional approach and extenstion in the non-linear domain. First International Conference on Transport Infrastructure. Beijing (2008)
27. Nguyen, H.M., Pouget, S., Di Benedetto, H., Sauzeat, C. Generalization of the Time-Temperature Superposition Principle for bituminous mixtures: experimentation and modeling. Paris: Orgagec (2008)
28. Williams, M.L., Landel, R.F., Ferry, J.D. The temperature dependence of relaxation mechanisms in amorphous polymers and other glass-forming liquids (1955)
29. Bodin, D. Modèle d'endommagement par fatigue: Application aux enrobés bitumineux. Nantes: École Centrale de Nantes (2002)
30. Corte, J.F., Goux, M.T. Design of pavement structures: the French technical guide. Transport Research Report 1539: 116-124 (1996)
31. Chailleux, E., Ramond, G., Such, C., de la Roche, C. A mathematical-based master-curve construction method applied to complex modulus of bituminous materials. Roads Materials and Pavement Design 7 (SI EATA): 75-92 (2006)
32. Huet, C. Coupled size and boundary-condition effects in viscoelastic heterogeneous and composite bodies. Mechanics and Materials 31: 787-829 (1999)
33. Sayegh, G. Viscoelastic properties of bituminous mixes. In proceedings of the 2nd International Conference on the Structural design of Asphalt Pavements Proceedings:. University of Michigan, Ann Arbor, Michigan, USA. 743-755 (1967)
34. Chabot, A., Chupin, O., Deloffre, L., Duhamel, D. Viscoroute 2.0: a tool for the simulation of moving load effects on asphalt pavement. RMPD Special Issue on Recent Advances in Numerical Simulation of Pavements 11 (2): 227-250 (2010)
35. EN 12697-7:2002 Bituminous mixtures. Test methods for hot mix asphalt. Determination of the bulk density of bituminous specimens by gamma rays

36. Bodin, D., de la Roche C., Pijaundier-Cabot, G. Size Effect regarding Fatigue Evaluation of Asphlat Mixtures. Roads Materials and Pavement Design 7 (SI EATA): 181-200 (2006)
37. Bodin, D., Pijaundier-Cabot, G., De La Roche, C., Piau, J.M. Chabot, A. Continuum Damage Approach to Asphalt Concrete Fatigue Modelling. ASCE Journal of Engineering Mechanics 130 (6): 700-708 (2004)
38. EN-12697-24-2007. Bituminous mixtures - Test methods for hot mix asphalt - Part 24: Resistance to fatigue.
39. EN-12697-26-2004. Bituminous mixtures - Test methods for hot mix asphalt - Part 26: Stiffness.
40. Baburamani, P. Asphalt fatigue life prediction models: a literature review. ARRB Transport Research (1999)
41. Bankowski, W., Sybilski, D. Energetic method as an alterative for conventional method in fatigue life analysis of bituminous mixtures. 4th International SIIV Congress. Palermo, Italy. 12-14 (2007)
42. Hopman, Kunst, and Pronk. A renewed interpretation method for fatigue measurement verification of Miners rule. 4th Eurobitume Symposium. Madrid. 557-561 (1989)
43. Pell, P.S. Fatigue of Asphalt Pavement Mixes. Proceedings of the Second International Conference on the Structural Design of Asphalt Pavements. Ann Arbor, Michigan (1967)
44. Vecoven, J.H. Méthode détude de systèmes limitant la remontée de fissures dans les chausses. In Proceedings of the 2th International RILEM Conference on Reflective Cracking in Pavements – Assessment and Control, March 8 to 10, Liège. Edited by Rigo J.M., Degeimbre R., 57-62 (1989)
45. Dumas, P., Vecoven J. Processes reducing reflective cracking ; synthesis of laboratory tests. In Proceedings of the 2th International RILEM Conference on Reflective Cracking in Pavements - State of the Art and Design Recommendations. March 10 to 12, Liège. Edited by Rigo J.M., Degeimbre R. et Francken L., 246–253 (1993)
46. Dubois, F., Petit, C. Modelling of the crack growth initiation in viscoelastic media by the Gq-integral. Engineering Fracture Mechanics 72: 2821-2836 (2005)
47. Dubois, F., Chazal, C., Petit, C. A finite element analysis of creep-crack growth in viscoelastic media. Mechanics of Time-Dependent Materials 2: 269-286 (1999)
48. Nguyen, H.N. Etude numérique de la fissuration dun milieu viscoélastique : Analyse de l'essai de rupture sur bitume, PhD thesis, LCPC (2008)
49. Maillard, S., de La Roche, C., Hammoum, R., Gaillet, L., Such, C. Experimental investigation of fracture and healing of bitumen at pseudo-contact of two aggregates. Eurobitume 1291-1304 (2004)
50. Dubois, F., Moutou Pitti, R., Picoux, B., Petit, C. Finite element model for crack growth process in concrete bituminous. Advances in Engineering Software 44: 35-43 (2012)
51. Li, X., Braham, A., Williams, A., Marasteanu, M., Buttlar, W. Effect of Factors Affecting Fracture Energy of Asphalt Concrete at Low Temperature. Road Materials and Pavement Design 9 (SI): 397-416 (2008)
52. Song, S. H., Paulino, G.H., Buttlar, W.G. A Bilinear Cohesive Zone Model Tailored for Fracture of Asphalt Concrete considering Rate Effects in Bulk Materials. Engineering Fracture Mechanics 73 (18): 2829-2348 (2006)
53. Dave, E., Buttlar, W. Low Temperature Cracking Prediction with Consideration of Temperature Dependent Bulk and Fracture Properties. Road Materials and Pavement Design 11 (SI): 33-59 (2010)
54. Majidzadeh, K., Kaufmann, E.M. and Ramsamooj, D.V. Application of Fracture Mechanics in the Analysis of Pavement Fatigue, Journal of the Association of Asphalt Paving Technologists 40, 227-246 (1971)

55. Ramsamooj, D.V. Prediction of Fatigue Life of Asphalt Concrete Beams from Fracture Test, Journal of Testing and Evaluation. 19 (3), 231-239 (1991)
56. Jacobs, M.J., Hopman, P.C., Molenaar, A.A. Application of Fracture Mechanics Principles to Analyze Cracking in Asphalt Concrete, Journal of the Association of Asphalt Paving Technologists 65, 1-39 (1996)
57. Kim, Y.R., Lee, H.J., Little, D.N. Fatigue Characterization of Asphalt Concrete Using Viscoelasticity and Continuum Damage Theory, Journal of the Association of Asphalt Paving Technologists 66, 520-569 (1997)
58. Kim, Y.R., Little, D.L. Benson, F. Chemical and Mechanical Evaluation on Healing Mechanism of Asphalt Concrete, Journal of the Association of Asphalt Paving Technologists 59, 240-276 (1990)
59. Zhang, Z. Identification of Suitable Crack Growth Law for Asphalt Mixtures Using the Superpave Indirect Tensile Test (IDT), Ph.D. Dissertation (University of Florida, Gainesville) (2000)
60. Zhang, Z., Roque, R., Birgisson, B. Sangpetngam, B. Identification and Verification of a Suitable Crack Growth Law, Journal of the Association of Asphalt Paving Technologists 70, 206-241 (2001)
61. Roque, R., Birgisson, B., Sangpetngam, B., Zhang, Z., Hot Mix Asphalt Fracture Mechanics: A Fundamental Crack Growth Law for Asphalt Mixtures, Journal of the Association of Asphalt Paving Technologists 71, 816-827 (2002)
62. Zhang, Z., Roque, R. Birgisson, B. Evaluation of Laboratory Measured Crack Growth Rate for Asphalt Mixtures, Transportation Research Record: Journal of the Transportation Research Board 1767, 67-75 (2001)
63. Birgisson, B., Montepara, A., Romeo, E., Roque, R., Roncella, R., Tebaldi, G. Determination of Fundamental Tensile Failure Limits of Mixtures, Journal of the Association of Asphalt Paving Technologists 76, 303-344 (2007)
64. Kim, B. Roque, R. Evaluation of Healing Property of Asphalt Mixture, Transportation Research Record: Journal of the Transportation Research Board 1970, 84-91 (2006)
65. Sangpetngam, B. Development and Evaluation of a Viscoelastic Boundary Element Method to Predict Asphalt Pavement Cracking, Ph.D. Dissertation (University of Florida, Gainesville) 2003.
66. Roque, R., Birgisson, B., Drakos, C., Dietrich, B. Development and Field Evaluation of Energy-Based Criteria for Top-down Cracking Performance of Hot Mix Asphalt, Journal of the Association of Asphalt Paving Technologists 73, 229-260 (2004)
67. Rowe, G. M. Performance of Asphalt Mixtures in the Trapezoidal Fatigue Test. Proceedings of the Association of Asphalt Paving Technologists, vol. 62 (1993)
68. Rowe, G. M. Application of the dissipated energy concepts to fatigue cracking in asphalt pavements. PhD thesis at University of Nottingham, UK (1996)
69. Ghuzlan, K. A. Carpenter, S. H. Traditional Fatigue Analysis of Asphalt Concrete Mixtures. TRB, Transportation Reasearch Board (2003)
70. Monismith, C. L., Deacon, J.A. Fatigue of Asphalt Paving Mixtures. Journal of Transportation Engineering ASCE, vol. 95 (1969)
71. Pell, P. S., Cooper, K. E. The Fatigue of Testing and Mix Variable on the Fatigue Performance of Bituminous Materials. Association of Asphalt Paving Technologist 44 proc., Phoenix, AZ (1975)
72. Van Dijk, W., Visser, W. The Energy Approach to Fatigue for Pavement Design. Proceedings of the Association of Asphalt Paving Technologists (AAPT), vol. 46 (1977)
73. SHRP-A-404. Fatigue Response of Asphalt-Aggregate Mixes. Washington, DC: Report for the Asphalt Research Program Institute of Transportation Studies University of

California, Berkeley. Strategic Highway Research Program National Research Council (1994)
74. Ghuzlan, K. Carpenter S. Energy-Derived, damage-based failure criterion for fatigue testing. Transportation Research Record - TRR, 1723 (2000)
75. Shen, S. Dissipated Energy Concepts for HMA Performance: Fatigue and Healing, PhD thesis, Departement of Civil and Environmental Engineering. University of Illinois at UrbanaChampaign: Urbana, Illinois (2007)
76. Ghuzlan, K. Carpenter S. Fatigue damage analysis in asphalt concrete mixtures using the dissipated energy approach. Canadian Journal of Civil Engineering (2001)
77. Stéfani C., Unicité des états spaciaux dendommagement. Internal note LCPC (1990)
78. Chehab, G. R., Kim, Y.R., Schapery, R.A., Witczak, M.W., and Bonaquist, R. Time-Temperature Superposition Principle for Asphalt Concrete Mixtures with Growing Damage in Tension State. Journal of Association of Asphalt Paving Technologists, Vol. 71, pp. 559–593 (2002)
79. Underwood, B. S., Kim, Y.R., Chehab, G.R. A Viscoelastoplastic Continuum Damage Model of Asphalt Concrete in Tension, Proceedings of the 10th International Conference of Asphalt Pavements (2006)
80. Zhao, Y. Permanent Deformation Characterization of Asphalt Concrete Using a Viscoelastoplastic Model. North Carolina State University (2002)
81. Gibson, N.H., Schwartz, C.W., Schapery, R.A., Witczak, M.W. Viscoelastic, Viscoplastic, and Damage Modeling of Asphalt Concrete in Unconfined Compression. Transportation Research Record 1860: 3-15 (2003)
82. Kim, Y.R., Guddati, B.S., Underwood, T.Y., Yun, Subramanian, V., Heidari, A.H. Characterization of ALF Mixtures Using the Viscoelastoplastic Continuum Damage Model. Final report to the Federal Highway Administration (2005)
83. Schapery, R.A. Correspondence Principles and a Generalized J-integral for Large Deformation and Fracture Analysis of Viscoelastic Media. International Journal of Fracture 25: 195-223 (1984)
84. Kim, Y.R., Little, D.N. One-Dimensional Constitutive Modeling of Asphalt Concrete. ASCE Journal of Engineering Mechanics 116 (4): 751-772 (1990)
85. Kim, Y.R., Lee, Y.C., Lee, H.J. Coorespondence Principle for Characterization of Asphalt Concrete. Journal of Materials in Civil Engineering, ASCE 7 (1): 59-68 (1995)
86. Lee, H.J., Kim, Y.R. A Uniaxial Viscoelastic Constitutive Model for Asphalt Concrete under Cyclic Loading. ASCE Journal of Engineering Mechanics 124 (1): 32-40 (1998)
87. Schapery, R.A. A Theory of Mechanical Behavior of Elastic Media with Growing Damage and Other Changes in Structure. J. Mech. Phys. Solids 38: 215-253 (1990)
88. Schapery, R.A. Deformation and Fracture Characterization of Inelastic Composite Materials Using Potentials. Polymer Engineering 27: 63-76 (1987)
89. Lamborn, M. J., Schapery, R.A. An Investigation of Deformation Path-Independence of Mechanical Work in Fiber-Reinforced Plastics, Sicking; Washington, D.C.; USA; pp. 991–1000 (1989)
90. Sicking, D.L. Mechanical Characterization of Nonlinear Laminated Composites with Tranverse Crack Growth. College Station: Texas A&M University (1992)
91. Lamborn, M.J. Schapery, R.A. An Investigation of the Existence of a Work Potential for Fiber Reinforced Plastic. Journal of Composite Materials 27 (4): 352-382 (1993)
92. Park, S.W. Development of a Nonlinear Thermo-Viscoelastic Constitutive Equation for Particulate Composites with Growing Damage. Texas A&M University (1994)
93. Schapery, R.A. A Theory of Crack Initiation and Growth in Viscoelastic Media, Part I: Theoretical Development, Part II: Approximate Methods of Analysis, Part III: Analysis

of Continuous Growth. International Journal of Fracture 11: 141-159, 369-388, 549-562 (1975)

94. Park, S.W., Kim, Y.R., Schapery, R.A. A Viscoelastic Continuum Damage Model and Its Application to Uniaxial Behavior of Asphalt Concrete. Mechanic and Materials 24 (4): 241-255 (1996)
95. Daniel, J. S., Kim, Y.R. Development of a Simplified Fatigue Test and Analysis Procedure Using a Viscoelastic Continuum Damage Model, Journal of the Association of Asphalt Paving Technologists, Vol. 71, pp. 619–650 (2002)
96. Chehab, G. R., Kim, Y.R., Schapery, R. A., Witczak, M.W., Bonaquist, R. Characterization of Asphalt Concrete in Uniaxial Tension Using a Viscoelastoplastic Model, Journal of the Association of Asphalt Paving Technologists, pp. 315-355 (2003)
97. Underwood, B.S., Kim, Y.R., Guddati, M.N. Improved Calculation Method of Damage Parameter in Viscoelastic Continuum Damage Model, International Journal of Pavement Engineering, Volume 11, Issue 6, pp. 459-476 (2010)
98. Hou, T., Underwood, B.S., Kim, Y.R. Fatigue Performance Prediction of North Carolina Mixtures Using the Simplified Viscoelastic Continuum Damage Model, Journal of the Association of Asphalt Paving Technologists, Vol. 79, pp. 35-80 (2010)